UNIVERSITY OF CALIFORNIA SAN DIEGO

Visualizing circadian cell biology in cyanobacteria

A dissertation submitted in partial satisfaction of the
requirements for the degree Doctor of Philosophy

in

Biology with a Specialization in Quantitative Biology

by

Vinson Curtis Lam

Committee in charge:

Professor Susan Golden, Chair
Professor Elizabeth Villa, Co-Chair
Professor Terence Hwa
Professor Susan Taylor
Professor James Wilhelm

2022

The Dissertation of Vinson Curtis Lam is approved, and it is acceptable in quality and form for publication on microfilm and electronically.

University of California San Diego

2022

DEDICATION

I dedicate this dissertation to my parents, Mai and Van Lam, and to my brother, Sherman. Although they have not read it (yet), they are surely among the authors. Who I am and what I have accomplished, have been with their unwavering support. Their time, their energy, their *food*, and—most importantly—their love have given me the strength, fortitude, and clarity of thought in my pursuit knowledge.

EPIGRAPH

I close my eyes and see a flock of birds. The vision lasts a second, or perhaps less; I am not sure how many birds I saw. Was the number of birds definite or indefinite? The problem involves the existence of God. If God exists, the number is definite, because God knows how many birds I saw. If God does not exist, the number is indefinite, because no one can have counted. In this case I saw fewer than ten birds (let us say) and more than one, but did not see nine, eight, seven, six, five, four, three, or two birds. I saw a number between ten and one, which was not nine, eight, seven, six, five, etc. That integer—not-nine, not-eight, not-seven, not-six, not-five, etc.—is inconceivable. *Ergo,* God exists.

Argumentum Ornithologicum, *Jorge Luis Borges*

TABLE OF CONTENTS

LIST OF FIGURES

LIST OF TABLES

LIST OF ABBREVIATIONS

CCM Carbon (CO_2) Concentrating Mechanism

CET Cryo-electron Tomography

CLEM Correlated Light and Electron Microscopy

CT Circadian Time

FIB Focused Ion Beam

IBC Iterative Binary Classification

PC Pro-carboxysome

S7002 *Synechococcus elongatus* PCC 7002

S7942 *Synechococcus elongatus* PCC 7942

SEM Scanning Electron Microscopy

SPA Single Particle Analysis

STA Sub-Tomogram Averaging

TEM Transmission Electron Microscopy

ZT Zeitgeber Time

μE μEinsteins, equivalent to μmoles of photons $m^{-2}s^{-1}$

ACKNOWLEDGEMENTS

I would like to acknowledge Professor Susan Golden and Professor Elizabeth Villa for their scientific support, advice, and mentorship over the past several years. Having a student with fingers in too many pies can be challenging for everyone involved. But I am grateful for their forbearance and for letting me have a chance to experience all they have to offer.

Chapter 1, in full, is currently being prepared for submission for publication as Vinson Lam and Susan Golden. "Circadian rhythms in *Synechococcus elongatus* PCC 7942 are independent of *smc*-mediated chromosome compaction". The dissertation author was the primary investigator and author of this paper.

Chapter 3, in part, is published as Benjamin R. Gilbert, Zane R. Thornburg, Vinson Lam, Fatema-Zahra M. Rashid, John I. Glass, Elizabeth Villa, Remus T. Dame, and Zaida Luthey-Schulten. "Generating Chromosome Geometries in a Minimal Cell From Cryo-Electron Tomograms and Chromosome Conformation Capture Maps", Frontiers in Molecular Biosciences, vol.8, 2021. The dissertation author was a secondary investigator and author of this paper.

Chapter 4 is a reprint of material published as Vinson Lam and Elizabeth Villa "Practical Approaches for Cryo-FIB Milling and Applications for Cellular Cryo-Electron Tomography", Methods in Molecular Biology, vol.2215, 2021. The dissertation author was the primary investigator and author of this paper.

VITA

2015	Bachelor of Sciences in Biochemistry with a Specialization in Computing University of California, Los Angeles
2017–2019	Instructional Assistant Assistant, Department of Biological Sciences University of California San Diego
2017–2022	Graduate Student Researcher University of California San Diego
2022	Doctor of Philosophy in Biology with a Specialization in Quantitative Biology University of California San Diego

FIELDS OF STUDY

Major Field: Biological Sciences (Microbiology and Quantitative Biology)

Studies in Microbiology and Circadian Biology
Professor Susan Golden

Studies in Cryo-Electron Tomography
Professor Elizabeth Villa

Studies in Quantitative Biology
Professors Susan Golden, Elizabeth Villa, and Terence Hwa

ABSTRACT OF THE DISSERTATION

Visualizing circadian cell biology in cyanobacteria

by

Vinson Curtis Lam

Doctor of Philosophy in Biology with a Specialization in Quantitative Biology

University of California San Diego, 2022

Professor Susan Golden, Chair
Professor Elizabeth Villa, Co-Chair

Circadian clocks are nearly ubiquitous throughout life, appearing in eukaryotes and prokaryotes alike. They are an adaptation that evolved to modify metabolism and behavior in anticipation of the daily fluctuation in light and other environmental conditions. One of the simplest organisms to posses a circadian clock is the photoautotrophic cyanobacterium *Synechococcus elongatus* PCC 7942. As an organism wholly dependent on the sun's energy, its biology is structured around the day-night cycle. Its metabolism, gene expression, and cellular organization are regulated in a circadian manner. Here, I investigate the potential role of circadian chromosome compaction in imparting rhythmicity to downstream gene expression.

I used fluorescence microscopy to visualize chromosome compaction status and correlate it to rhythmic gene expression. I also investigated circadian changes in cellular organization using high-resolution cryo-electron tomography (CET) to visualize cells in a near-native state. I report interesting subcellular structures and features that have not been observed previously. In support of CET as a maturing tool for cell biology, I present data and considerations for sample preparation and downstream data analysis.

Introduction

Life on earth has evolved around daily fluctuations in light, temperature, and humidity because of Earth's rotation. Consequently, many organisms have developed circadian rhythms, driven by a circadian clock, to modulate their metabolism and behavior in anticipation of regular, predictable environmental changes. Circadian clocks are nearly ubiquitous throughout life, appearing in eukaryotes and prokaryotes alike.

One of the simplest organisms to posses a *bona fide* circadian clock is the photoautotrophic cyanobacterium *Synechococcus elongatus* PCC 7942. Its clock is driven by a protein-based oscillator that signals time by the phosphorylation state of the central clock protein KaiC over a 24-hour period. The circadian clock includes a rhythmically phosphorylated transcription factor, RpaA, that directs expression of dawn and dusk genes at the appropriate time. However, a larger portion of circadian genes are not directly regulated by RpaA. One hypothesis in the field is that regulation of chromosome compaction in a manner similar to hetero- and euchromatin in eukaryotes may be used to drive circadian rhythms. In Chapter 1, we present research investigating the role of chromosome compaction mediated by the condensin Smc in imparting rhythmic gene expression. We find that circadian rhythmicity is independent of the chromosome status.

In addition to investigating the role of *smc* in imparting circadian rhythmicity, we wanted to investigate rhythmic changes in cyanbacterial ultrastructure. Because the metabolism and biology of cyanobacteria are structured around daily fluctuations in light level, we reasoned that such large swings in energy availability would be reflected in the cellular biology of the organism.

In order to study the complex cellular environment of a cyanobacterium, we can use

cryo-electron tomography (CET) to reconstruct the 3D architecture of cellular structures as they exist *in situ*. By flash-freezing whole cells to prevent ice crystallization, we can take a snapshot of what the cell looks like at any point in time. However, CET is limited by sample thickness to less than 500 nm, which renders the method inaccessible even to most bacteria. With focused ion beam (FIB) milling, we can open windows to study the interior of a bacterium by creating $\sim$180 nm thick sections that are accessible to CET. With correlative light and electron microscopy (CLEM), we can compare the fluorescent signals of protein localization to the high-resolution structures observed through electron microscopy for the same sample. In Chapter 1.5 we present observations of cyanobacterial ultrastructure including unknown membrane anchored macromolecules, carboxysome biogenesis, and thylakoid membrane biogenesis.

The past decade has seen technological leaps that enable faster acquisition of higher quality cryoEM data and downstream analysis. The field has developed to a point where structural determination using single particle cryoEM is a routine technique accessible to labs as a commercial service. CET has likewise reaped the benefits from these advances. However due to large variations in sample preparation techniques, CET is still limited to those labs with sufficient expertise and appropriate equipment. Additionally, CET is used to investigate complex cellular environments in diverse organisms. Depending on the specific question of interest, analysis techniques may be vastly different and require custom programming. In Chapter 3, we present developments and considerations for identification of macromolecules in tomograms. In Chapter 4, we present detailed instructions and considerations on using cryo-FIB milling to prepare cellular samples for CET.

Chapter 1

Circadian rhythms in *Synechococcus elongatus* PCC 7942 are independent of *smc*-mediated chromosome compaction

1.1 Introduction

Circadian regulation of biological processes enables an organism to modify their behavior and metabolism in anticipation of regular daily fluctuations in environmental conditions, including light and temperature. Circadian clocks are bio-molecular timekeepers that indicate the subjective time of an organism and direct changes to prepare for the upcoming day or night. In the obligate photoautotrophic bacterium *Synechococcus elongatus* PCC 7942 (hereafter S7942), cell growth and metabolism are intimately tied to the day-night cycle [1, 2]. Among other processes, cells accumulate glycogen during the daytime phase and metabolize it during the nighttime phase [2]. Other behaviors are also tied to the circadian cycle: natural transformability peaks with the onset of dusk [3] and cell division is restricted during the early nighttime window [4, 5]. Such large-scale organization requires circadian coordination of gene expression and in S7942 the genome is globally regulated in a circadian manner [6, 7]. The core KaiABC oscillator indicates subjective time of day through the phosphorylation state of KaiC and regulates gene expression by directing the rhythmic phosphorylation of transcription factor RpaA [8]. However, there exist many genes that are not direct targets of RpaA yet are expressed in a circadian manner

[9]. Additionally, non-native promoters, such as a consensus *E. coli* promoter, are also expressed in a circadian manner [10].

In S7942 a screen for circadian gene expression through a randomly integrated promoter-less reporter [7] showed that in nearly all cases where the reporter could be detected, the signal exhibited rhythmic expression. This unexpectedly broad result suggested that some level of circadian gene expression may be regulated in a sequence-independent manner. One potential regulation pathway is through changes in chromosome topology [11]. Changing chromosome topology is a marker of genetic regulation seen throughout all domains of life. In eukaryotes euchromatin and heterochromatin indicate regions of actively expressed and repressed genes, respectively. In bacteria the reduction of cellular activity during stationary phase is accompanied by chromosome condensation and rearrangement. It is possible that rearrangement of chromosomal packaging is involved in the regulation of circadian gene expression.

Previous work has shown that DAPI-stained chromosomes exhibit compaction cycles that persist in constant light conditions [12]. Additionally, rhythmic DNA supercoiling of the endogenous plasmid in S7942 is regulated in a circadian manner and is abolished by deletion of the KaiABC oscillator [13]. Cyanobacterial promoters relocated onto the plasmid or elsewhere in the genome maintain rhythmic gene expression, suggesting that rhythmicity is not dependent on the original chromosome context [13, 14]. Moreover, a topology sensitive *E. coli* promoter, P_{fis}, was shown to express rhythmically when introduced into cyanobacteria [15]. Perturbing cellular supercoiling with transient antibiotic dosage was also shown to induce changes in gene expression comparable to changes seen during a day-night cycle [6]. In this work, we examine the potential role of the condensin *smc* in regulating circadian chromosome compaction. Condensins are nucleoid-associated proteins that isolate DNA loops and supercoils [16]. Work on chromosome organization in diverse bacterial species has demonstrated that deletion of *smc* leads to decondensed nucleoids and chromosome partitioning defects [17]. By creating a genetic system with chromosome packaging constitutively altered through loss of *smc*, we can investigate how chromosome compaction and DNA topology affects circadian rhythmicity and

other hallmarks of cyanobacterial circadian physiology.

1.2 Results and Data

The *smc* gene in *Synechococcus elongatus* PCC 7942 was putatively identified in the UniProt database (UniProt Q31LJ4) as gene locus Synpcc7942_2045. The gene was inferred to be *smc* based on amino acid homology with known sequences of *E. coli* and *B. subtilis* Smc using BLASTP. In order to investigate the potential role of chromosome compaction in circadian rhythmicity of gene expression, we created an *smc* deletion strain (abbreviated as Δ*smc*) that has an antibiotic cassette replacing the open reading frame of the gene. We also constructed an *smc* complementation allele under the control of an IPTG-inducible promoter (abbreviated as +*smc*), inserted at a neutral site in the chromosome.

1.2.1 Chromosomes in cyanobacteria undergo rhythmic compaction

To determine whether we could visualize the circadian compaction of S7942 chromosomes that has been previously reported [12] we calculated a chromosome compaction index (CI) for individual cells at each circadian hour based on DAPI staining [12]. The compaction index ranges from 0 (least compact) to 1 (most compact) and is a measure of normalized pixel intensity disparity within the boundaries of a single cell (Figure 1.1B,C).

In entrained WT cells DAPI-stained chromosomes exhibited rhythmic chromosome compaction over the course of the circadian day (Figure 1.1A). Compaction was generally higher during the daytime window (ZT 00 to ZT 11) and generally lower during the nighttime window (ZT 12 to ZT 23), with a sharp peak at ZT 16. In comparison, Δ*smc* cells exhibited a lower overall CI throughout the circadian day. Additionally, in Δ*smc* the difference in CI between daytime and nighttime was reduced. As predicted, the levels of chromosome compaction were appreciably different in the two strains, with a 24-hour overall average CI of 0.21 for WT and 0.16 for Δ*smc*. When considering only the daytime phase rom ZT 00 to ZT 11, the average CI changes to 0.24 for WT and 0.16 for Δ*smc*.

However, Δ*smc* cells still appeared to exhibit rhythms in chromosome compaction with the same phase as WT and with decreased amplitude. In particular, Δ*smc* cells also had peak compaction times similar to WT cells at ZT 08 and ZT 16, although the CI is lower in Δ*smc* compared to WT at both times . Under identical conditions, +*smc*-complemented cells have recovered compaction levels to be comparable to WT levels and the chromosome compaction rhythm matches that of the WT strain.

Because Δ*smc* cells still exhibited a reduction in circadian chromosome compaction, we wanted to investigate the chromosome compaction status in the absence of a circadian oscillator. In Δ*kaiC* cells, which lack the foundational protein of the circadian oscillator, we found that rhythmic chromosome compaction no longer occurs (Figure 1.2A). The chromosome compaction index stayed consistent over the course of a circadian day both under entrained and free-running conditions. The average CI in Δ*kaiC* cells appeared to be near the minimum CI in WT cells from ZT 12 to ZT 14. The mean CI in WT cells during early dusk is 0.16 compared to the overall mean CI in Δ*kaiC* of 0.19, indicating that the chromosome is constitutively in a more decompacted state. Additionally, we found that the average CI in Δ*kaiC*Δ*smc* cells is identical to the CI of Δ*kaiC* cells alone (Figure 1.1B).

In the following experiments, we used the Δ*smc* and +*smc* complementation constructs to investigate the role of chromosome compaction in regulation of circadian gene expression by. Although rhythms of chromosome compaction persisted in both *smc* mutants, there is a clear difference in the overall level of compaction. Deletion of *smc* leads to a more diffuse chromosomal appearance and would be expected to lead to a more open and accessible chromosome. Conversely, *smc* overexpression would lead to a more inaccessible chromosome. Both of these scenarios would likely change the ability for transcription machinery to initiate gene expression. Therefore we wanted to investigate whether strains with altered chromosome compaction status from genetic manipulation of *smc* would have perturbed rhythmic gene expression.

1.2.2 Chromosome compaction status does not affect circadian rhythmicity

If chromosome compaction were responsible for the circadian expression of genes, we would expect that deletion or overexpression of *smc* would lead to measurable perturbations in gene expression, and that indirectly regulated circadian genes would be more affected than directly RpaA regulated genes. In addition, because chromosome compaction status corresponds to a unique point in circadian time, we would expect that perturbing chromosome compaction with *smc* mutants would change the ability for cells to shift their circadian phase in response to a resetting light pulse.

To test this hypothesis we constructed Δ*smc* and P_{trc}::*smc* strains carrying four different reporter genes, two directly and two indirectly regulated by RpaA. P_{kaiBC}::*luc* and P_{PurF}::*luxAB* are bound by RpaA, and P_{PsbA1}::*luxAB* and P_{conII}::*luxAB* are not direct targets. P_{kaiBC}, P_{PsbA1}, and P_{conII} are Class 1 promoters, with peak expression at subjective dusk. P_{PurF} is a Class 2 gene with peak expression at subjective dawn. P_{conII} is of particular interest because it is the consensus sequence from *E. coli* and is not native to S7942 [10]. Nonetheless, P_{conII} drives circadian expression of luciferase reporter genes. Therefore, we would expect this reporter to be more sensitive to changes in circadian rhythmicity arising from non-genetically encoded factors.

The circadian bioluminescence traces from of all WT reporters resembled previously reported data. For all reporter strains, comparing the bioluminescence readout of the WT strain to the Δ*smc* strain showed no appreciable difference in rhythmicity. Here, we show representative bioluminescence traces from the P_{conII}::*luxAB* reporter (Figure 1.3A). Additionally, there was no change in rhythmicity for the *smc* overexpression strains.

A standard protocol for resetting the phase of circadian rhythms in S7942 is to apply a 5-hour dark pulse at ZT 08, which causes a phase advance (Figure 1.3B). In this assay the WT reporter strains advanced their circadian phase by approximately 4 to 5 hours, which agrees with previous findings [18]. The same dark pulse applied to Δ*smc* overexpression strains elicited

phase-resetting responses that were identical to those of the WT reporter strains (Figure 1.3B), revealing no effect of *smc* on circadian phasing or phase-resetting.

Because we did not observe any changes to circadian rhythmicity in any of the *smc* mutants, we wanted to determine whether chemically perturbing DNA topolgy would change rhythmic gene expression. Previous work investigating plasmid supercoiling showed that addition of sublethal amounts of the gyrase inhibitor novobiocin (0.1 μg/mL) caused rapid relaxation of the endogenous plasmid in S7942 [6]. Additionally, Δ*smc* mutations in other bacteria have been shown to be hypersensitive to gyrase inhibitors [17]. At 8 hours after releasing into constant light and (to a separate sample) at 16 hours after releasing into constant light, we added 0.1 μg/mL novobiocin or BG-11 medium only to each well (Figure 1.4). These circadian times were chosen because these correspond to the times of highest chromosome compaction index (Figure 1.1A). In both WT and Δ*smc* strains, we find no difference in rhythmicity over the course of five days from the addition of novobiocin. Additionally, the bioluminescence traces for WT and Δ*smc* were identical.

1.2.3 Chromosome compaction does not alter circadian regulated natural transformation

Natural transformation in S7942 involves the uptake and homologous recombination of exogenous DNA into the host chromosome. Additionally, recent research has shown that this natural transformation is regulated by the circadian clock, with peak transformation efficiency occurring near subjective dusk, which coincides with an inflection point in the chromosome compaction status [3]. There is evidence in both eukaryotes and prokaryotes that Smc-mediated chromosomal organization into topologically linked domains facilitates homologous recombination by holding DNA strands in close proximity [19, 20]. We wondered whether the absence of *smc* would affect the natural competence of S7942. Two alternative scenarios present themselves. First, chromosome compaction may bring homologous DNA regions closer together, thereby increasing the likelihood of recombination. Second, chromosome compaction may exclude

recombination machinery and impede the incorporation of exogenous DNA.

To test the effect of *smc* on natural transformation we set up a time course to evaluate transformation efficiency over one circadian day, based on previously established assays (Figure 1.5A). When compared to WT S7942 natural transformation, we found no effect of the loss of *smc* on the rhythmicity of transformation efficiency (Figure 1.5B); WT transformation agreed with previous results, but with a lower overall efficiency [3]. Transformation of both WT and Δ*smc* peaked with similar efficiencies at CT12. However, Δ*smc* showed a larger window of competence compared to WT. At CT08 and CT10 WT S7942 had minimal transformation efficiency (less than 1×10^{-4}) whereas Δ*smc* was three to four times more efficient (around 3×10^{-4}). Additionally, the window of competence appeared to be shifted forward in the mutant: at CT14, the transformation efficiency of WT cells was around 2.5×10^{-4}, but Δ*smc* transformation was close to zero.

1.3 Discussion

Chromosome packing and organization are key components of genetic regulation in all branches of life. Previous work on plasmid supercoiling and chromosome compaction in cyanobacteria has suggested that chromosome organization would be involved in circadian gene regulation in S7942. In the ”oscilloid” model, the rhythmic phosphorylation of KaiC leads to rhythms in chromosome topology, which in turn regulates gene expression through facilitating transcription initiation [13]. While we now know that the circadian transcription factor RpaA regulates several circadian promoters including P_{kaiBC}, it is unclear how indirect promoters such as P_{conII} are able to express in a rhythmic fashion.

In this work, we confirm that in *S. elongatus* PCC 7942 exhibits circadian chromosome compaction when visualized using fluorescent DNA-binding dyes, but has no effect on standard measures of circadian gene expression. The lack of any significant circadian defects in both Δ*smc* and smc overexpression strains suggest that chromosome compaction mediated by *smc* is

not involved in imparting circadian rhythmicity.

Curiously, both the Δ*smc* and Δ*kaiC* strains have a low average CI similar to the CI of the WT strain at the onset of dusk at ZT 12. Gene expression from bioluminescence reporters in a Δ*kaiC* strain is locked in a "dusk-like" state which leads to high constitutive expression from dusk promoters such as P_{kaiBC} [21]. However, we find that even though the chromosome compaction status of the Δ*smc* stain appears "dusk-like", there is no effect on rhythmic gene expression. In other clock deficient strains such as Δ*kaiA*, the cellular program is locked in a "dawn-like" state [21]. In such strains, the chromosome may have a constitutively high CI.

Because genetic perturbation of chromosome status did not change circadian rhythmicity, we sought to chemically alter chromosome status with a gyrase inhibitor. However, novobiocin treatment in our hands did not lead to changes in the circadian rhythmicity over a multi-day time course, in contrast to prior work demonstrating that addition of novobiocin relaxes plasmid supercoiling within five minutes and leads to measurable differences in plasmid supercoiling and gene transcription [6]. However, plasmid supercoiling quickly returns to baseline levels within two hours after initial treatment. Our circadian bioluminescence assay is sampled only at two-hour intervals due to mechanical limitations. Although we took care to measure bioluminescence within a few minutes of adding novobiocin, we were unable to capture such transient perturbations in either WT or Δ*smc* strains. The lack of any permanent effect from chemical perturbation suggests that chromosome topology does not play a role in imparting circadian rhythmicity to gene expression.

Unlike many other bacteria, deletion of *smc* does not appear detrimental to cell growth in S7942. However, the ectopic expression of the gene in the complementation +*smc* strain proved to be toxic over time. Initial transformants grew comparably to WT on both solid and in liquid media. However, once reaching stationary phase in liquid, +*smc* could not resume growth after passaging to fresh media. This may be due to leaky (uninduced) expression of *smc* leading to excessive chromosome packaging. A potential mechanism that may explain the growth-phase sensitivity is that during log-phase growth, chromosome occupancy by RNA polymerase is high

and inhibits SMC binding. When cells enter stationary phase, loss of transcriptional demand may allow SMC binding and subsequent blockage of transcription initiation when cells are returned to log-phase growth conditions.

Although changes in chromosome status did not appear to alter circadian gene expression, deletion of *smc* led to an expanded window of natural competence. This result may suggest increased chromosomal accessibility for DNA integration. However, we did not observe increased competence at all circadian timepoints. This result is expected, because natural transformation is a multi-step process that requires special circadian-regulated competence pili to import DNA. These pili are only expressed towards the end of the daytime period, so competence is lower by default at other times [3].

Why do chromosomes in S7942 appear to compact rhythmically? Rather than serving a regulatory function, compaction may be a response to the transcriptional demands of the cell based on energy availability. Active transcription alters the chromosome ultrastructure by making the gene locus more accessible [22]. As an obligate photoautotroph, S7942 has both abundant energy during the day and a strong transcription/translation demand to synthesize photosynthetic proteins, DNA replication, and new ribosome synthesis. In contrast, the nighttime transcriptional program is reduced compared to the daytime program. These daily rhythms in energy usage may drive chromosome status, suggesting that the observed rhythms in chromosome compaction are a downstream effect.

Taken together, our results suggest that rhythmic chromosome compaction does not impart circadian rhythmicity to gene expression. The question remains of what factors determine the rhythmicity and phasing of expression of a given gene. Promoter sequence and length have some effect in determining phase of gene expression, but phasing also depends on the context of the gene [15]. Single-nucleotide substitutions in the promoter spacer region that slightly modify the GC-content also affect the phasing of a circadian gene [23]. Given the lack of definite elements that confer circadian rhythmicity, it is likely that a combination of energy availability, metabolic factors, and subtle differences among promoter sequences contribute to differences in

circadian phasing.

1.4 Acknowledgements

Chapter 1, in full, is currently being prepared for submission for publication as Vinson Lam and Susan Golden. “Circadian rhythms in *Synechococcus elongatus* PCC 7942 are independent of *smc*-mediated chromosome compaction”. The dissertation author was the primary investigator and author of this paper.

1.5 Methods

Strain construction and culture conditions

Knockout and expression plasmids were made using the Cyano-Vector assembly portal [24]. Knockouts vectors consisted of an antibiotic-resistance cassettes flanked by regions of homology to the chromosome to replace the entire open reading frame of *smc* sequence through homologous recombination (denoted as Δ*smc*). Inducible expression vectors consisted of the native *smc* gene sequence, controlled by the IPTG-inducible P_{trc} promoter (denoted as +*smc*) and flanked by homologous regions to insert into neutral sites in the cyanobacterial chromosome [25]. Plasmids were verified by commercial Sanger sequencing. Complete segregation of the introduced alleles was verified by PCR amplification.

Cultures of *Synechococcus elongatus* PCC 7942 were grown in standard BG-11(N+) liquid medium, on shaking incubators set at 125 RPM, under 125-150 μmole photons $m^{-2}s^{-1}$ (μE) light fluence rate, at 30 °C.

For circadian experiments, a single log-phase culture was diluted to OD_{750} 0.05 to 0.1 with fresh medium and split into 5-mL aliquots in 18-mm glass tubes. Additionally, 1 ml of the same cells were spread on BG-11 agar media in a 35-mm dish and allowed to dry. One tube or one plate was prepared for each desired sampling timepoint. Both liquid and solid cultures were placed in controllable LD incubators and entrained to 12 h light:12 h dark (LD 12:12) at a constant 30 °C for at least 3 full dark cycles. Zeitgeber Time (ZT) indicates the phase of the

light cycle used to entrain the cells. ZT 00 corresponds to the onset of the light phase and ZT 12 corresponds to the onset of the dark phase.

At each timepoint, only one tube or plate was removed from the incubator to minimize environmental disturbances. Experiments using +*smc* were performed without the addition of IPTG unless explicitly noted and relied on the leaky expression from the P_{trc} promoter in cyanobacteria [26].

Chromosome compaction fluorescence microscopy

Cells were grown on BG-11 agar plates and entrained as described above. At each time point a plate was removed from the incubator and cells were scraped from the surface using a pipet tip. Cells were resuspended in 500 μL of 2.5% Glutaraldehyde in PBS pH 7.4 as a fixative buffer. Fixative was prepared fresh for each experiment using new 25% glutaraldehyde from glass ampoules (EMS). Cells in fixative were incubated in the dark for 30 minutes on a rotisserie shaker at room temperature. After initial fixation, cells were centrifuged at 4500×g for 5 minutes, and the supernatant decanted. Pellets were resuspended in 250 μL of fresh fixative, then stored in the dark at 4 °C overnight until subsequent staining. Samples were stained and visualized within 1 week of the initial fixation.

For staining, 250 μL of each sample was transferred to a 96-well v-bottom plate. All subsequent washes and buffer exchanges were done by centrifuging the plate at 2000×g and aspirating the supernatant. Incubation steps were done on a gyrotary shaker in the dark at room temperature. Cells were washed twice in 250 μL of PBS pH 7.4 + 20 mM glycine for 30 minutes each. Cells were resuspended in 150 μL of 1 μg/mL Hoechst 33342 in PBS pH 7.4 (without glycine), for 30 minutes. After staining, two additional washes of PBS (without glycine) for 10 minutes to remove unbound DNA dye. Cells were then resuspended in PBS to desired concentration.

Each sample was prepared for fluorescence microscopy by spotting 1 μL onto a pad made with 1.5% agarose in BG-11 medium. Cells were imaged on a Delta Vision system with

an Olympus IX71 inverted microscope equipped with a Weather Station temperature-controlled environmental box. Images were recorded using a 100x/1.40NA objective (Olympus UPlanSApo) in three channels: brightfield, TRITC (555EX/617em), and DAPI (360ex/457em). The TRITC channel was used to visualize the autofluorescence of the cyanbacterial thylakoid membranes and the DAPI channel was used to visualize Hoechst 33342-labeled DNA. Care was taken to ensure that the sensor did not saturate by adjusting exposure time for each channel, and the same settings were used for all subsequent imaging.

Quantification of compaction index

For the TRITC and DAPI channels of each image stack, the plane of best focus was determined manually and extracted into separate files using Fiji [27]. Cells were segmented using Matlab R2020a based on the cell autofluorescence in the TRITC channel. A compaction index for each cell was calculated using the DAPI channel delineated by the TRITC channel. DAPI pixels were ordered by intensity and used to calculate the Gini coefficient of each cell [12]. The Gini coefficient is a measure of income disparity widely used in macroeconomics that is also applicable to analysis of other statistical distributions [28]. By treating the per-pixel intensity in the DAPI channel as income, we derived a measure of pixel intensity disparity that indicates the level of chromosome compaction.

Circadian bioluminescence

Liquid cultures of WT and mutant reporter strains were grown as indicated above. Cultures were diluted to OD_{750} 0.2 and six technical replicates of 20 μL of each strain were distributed onto the surface of BG-11 agar in 96-well plates [29]. Plates were entrained to LD 12:12 for three full cycles as described above. Plates were transferred to continuous light (LL) conditions at 30 °C and biolumiscence emissions were read on a TECAN Infinite 200 Pro OR a TECAN Spark, both equipped with a microplate stacker system, at 2 hour intervals for approximately 1 week. For dark-induced phase-resetting experiments, plates were removed at the target time and loosely wrapped in aluminum foil. Wrapped plates were placed inside a light-

tight box for five hours. For novobiocin treatment, 10 μL of 3 μg/mL novobiocin sodium salt in BG-11 was added to each well, for a final concentration of about 0.1 μg/mL. Bioluminescent time course data were visualized using MATLAB and Biodare2 (biodare2.ed.ac.uk) [30]. Period and phase analysis were done using FFT-NLLS algorithm in Biodare2.

Natural transformation assay

Liquid cultures were grown as described above, then diluted to OD_{750} 0.1 for circadian entrainment. Diluted culture samples (30 mL) were placed into 250 mL Erlenmeyer flasks to ensure adequate aeration and light penetration.

The following transformation assay is adapted from previous work on circadian natural transformation [3]. At the beginning of the third full dark phase, cells were concentrated to OD_{750} 1.0 by centrifugation, split into 300 μL aliquots in 13-mm glass tubes, then returned to the incubator for the remainder of the dark phase. At the beginning of the next light phase, cells were released into constant light for the remainder of the experiment and retrieved as needed for each timepoint. DNA (150 ng) was added to 100 μL of cell suspension and incubated for 1 hour in the dark. At the end of the dark incubation, the cell suspension was diluted 1:5 with fresh BG-11 over 8 serial dilutions. Samples of each dilution (5 μL) were spotted onto two BG-11 plates, with and without antibiotic selection, and allowed to grow in LL until colonies appeared. Colonies were counted by hand. Transformation efficiency is reported as ratio of CFU/mL with selection to CFU/mL without selection.

Table 1.1. List of strains used in this study.

Strain Number	Genotype	Description	Selection	Reference
AM 5257	NS2::Km^R	Control plasmid for comparison with strains transformed with pAM5897.	Km	
AM 5328	NS3::Gm^R	Plasmid used for natural transformation assay.	Gm	
AM 5329	NS1::SpSm^R	Control plasmid for comparison with strains transformed with pAM5898	SpSm	
AM 5897	Δ*smc*::Km^R	*smc* deletion at native site and replace with antibiotic resistance cassette.	Km	This work
AM 5898	NS1::P$_{trc}$:*smc*	Ectopic expression of *smc* under control of an IPTG-inducible promoter to complement Δ*smc*. Used for fluorescence microscopy of chromosome compaction.	SpSm	This work
AM 5899	NS3::P$_{trc}$:*smc*	Ectopic expression of *smc* under control of an IPTG-inducible promoter to complement Δ*smc*. Used for bioluminescence assays.	Gm	This work
AMC 06	WT	*S. elongatus* PCC 7942	none	
AMC 539	P$_{conII}$::*luxAB*	Class 1 reporter	CmSpSm	
AMC 541	P$_{kaiBC}$::*luc*	Class 1 reporter	Cm	
AMC 669	P$_{psbA1}$::*luxAB*	Class 1 reporter	Cm	
AMC 693	P$_{purF}$::*luxAB*	Class 2 reporter	CmSpSm	
AMC 704	Δ*kaiC* P$_{kaiBC}$::*luc*	Arrhythmic Class 1 reporter	Cm	
AMC 2753	Δ*smc*	Used for fluorescence microscopy of chromosome compaction and natural transformation assay.	Km	
AMC 2754	Δ*smc* P$_{conII}$::*luxAB*	Δ*smc* in AMC 539. For bioluminescence assays.	CmSpSmKm	This work
AMC 2755	Δ*smc* P$_{kaiBC}$::*luc*	Δ*smc* in AMC 541. For bioluminescence assays.	CmKm	This work
AMC 2756	Δ*smc* P$_{psbA1}$::*luxAB*	Δ*smc* in AMC 669. For bioluminescence assays.	CmKm	This work
AMC 2757	Δ*smc* P$_{purF}$::*luxAB*	Δ*smc* in AMC 693. For bioluminescence assays.	CmSpSmKm	This work
AMC 2758	Δ*kaiC*Δ*smc* P$_{kaiBC}$::*luc*	Δ*smc* in AMC 704. For fluorescence microscopy of chromosome compaction	CmKm	This work
AMC 2759	NS1::+*smc*	*smc* complementation in WT background.	KmSpSm	This work
AMC 2760	NS3::+*smc*	*smc* complementation in AMC 539	CmSpSmKmGm	This work
AMC 2761	NS3::+*smc*	*smc* complementation in AMC 541	CmKmGm	This work
AMC 2762	NS3::+*smc*	*smc* complementation in AMC 669	CmKmGm	This work
AMC 2763	NS3::+*smc*	*smc* complementation in AMC 693	CmSpSmKmGm	This work

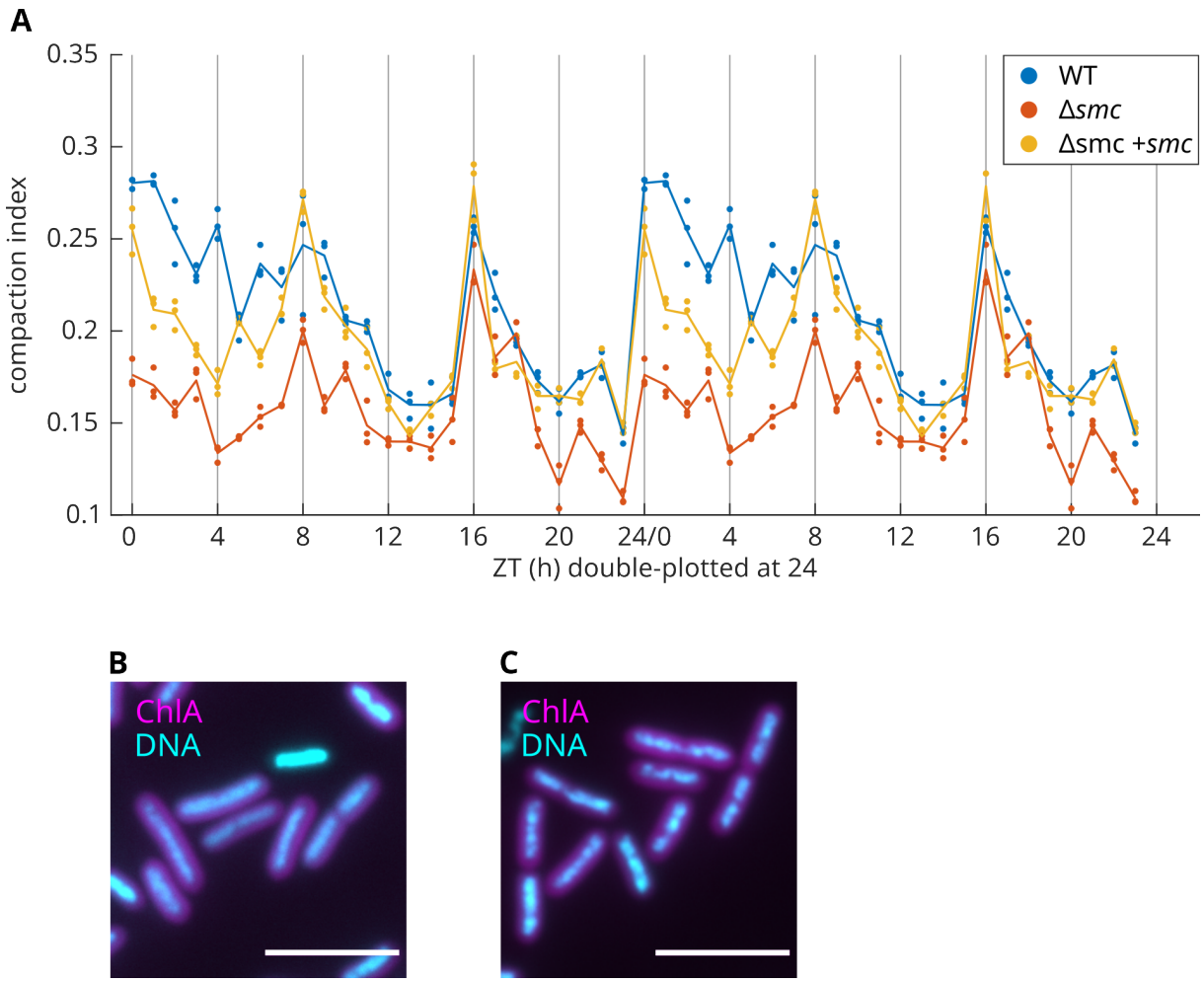

Figure 1.1. Circadian chromosome compaction in *Synechococcus elongatus* PCC 7942. (A) Double-plotted compaction indices (CI) of WT, Δ*smc*, and Δ*smc* +*smc* cells sampled over 24 hours from ZT 00 to ZT 23. CI was calculated from the pixel intensity disparity, ranging from 0 (least compact) to 1 (most compact), for each cell in a given micrograph. Each point represents the average CI of all cells in one micrograph. The line represents that average CI of all cells at a given time. For each time point, at least 3 micrographs were acquired, and at least 100 cells were analyzed. (B,C) Representative images of stained chromosomes in a decompacted (B) and compacted (C) state. Chlorophyll autofluorescence is shown in magenta. DNA stained with Hoechst-33342 dye is shown in cyan. CI was calculated only for cells with autofluorescence. *Scale bars 5 μm*

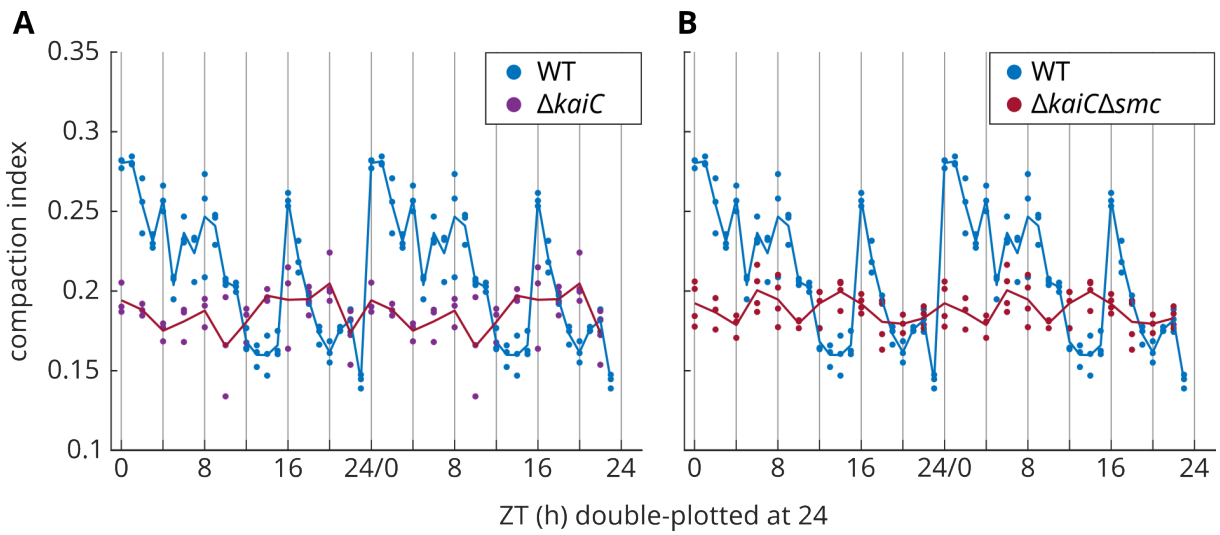

Figure 1.2. Chromosome compaction in arrythmic *Synechococcus elongatus* PCC 7942. (A,B) Double-plotted compaction indices (CI) of WT, Δ*kaiC*, and Δ*kaiC*Δ*smc* cells sampled over 24 hours from ZT 00 to ZT 23. CI was calculated as described in Figure 1.1. The line represents that average CI of all cells at a given time. For each time point, at least 3 micrographs were acquired, and at least 100 cells were analyzed. The data for WT are duplicated from Figure 1.1A for comparison purposes.

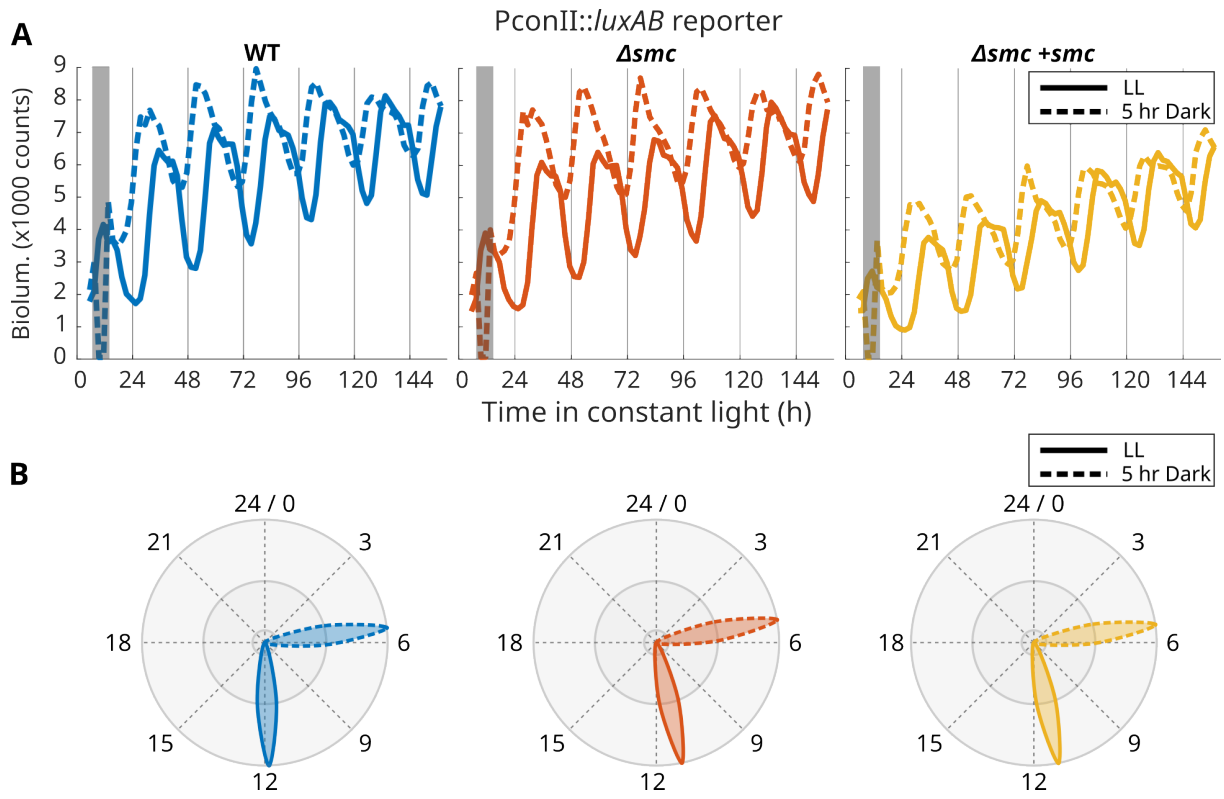

Figure 1.3. Circadian rhythmicity and resetting in *smc* mutants.
(A) Bioluminescence time course from the transcriptional reporter P_{conII}::*luxAB*, tracking activity of a non-native Class 1 promoter that has peak expression at dusk (ZT 12), in WT, Δ*smc*, and Δ*smc* +*smc* backgrounds. Free-running control rhythms are represented by solid lines. A 5-hour dark incubation starting at 8 hours after releasing into constant light was applied to a duplicate set of samples to induce a phase advance. The dark pulse application is marked by the gray bars. Free-running rhythms after application of the dark pulse are represented by dashed lines. Each trace represents the arithmetic mean of n=6. (B) Representation of phases for samples with and without 5-hour dark pulse. Solid and dashed lines as above. Phases were calculated using the mean bioluminescence trace.

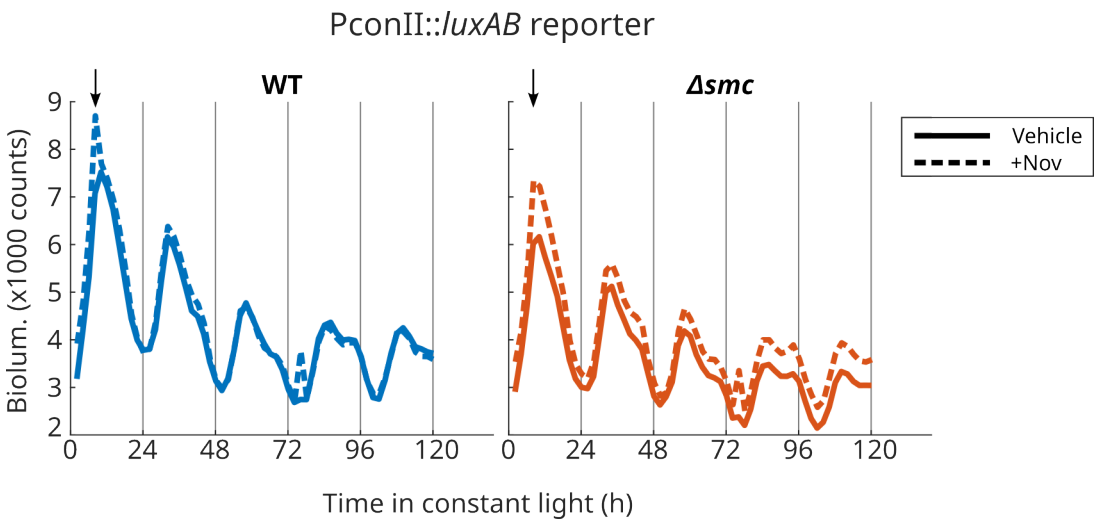

Figure 1.4. Circadian bioluminescence with novobiocin treatment.
Bioluminescence time course from the transcriptional reporter P_{conII}::*luxAB*, in WT and Δ*smc* cells, with and without the addition of the gyrase inhibitor novobiocin. Novobiocin sodium salt (0.1 μg/mL final conc.) was added at ZT 08, indicated by the arrow, corresponding to a time of increased chromosome compaction. Solid lines represent the bioluminescence trace of control cells treated with vehicle only. Dashed lines represent traces of cells treated with novobiocin. Each trace represents the arithmetic mean of n=6.

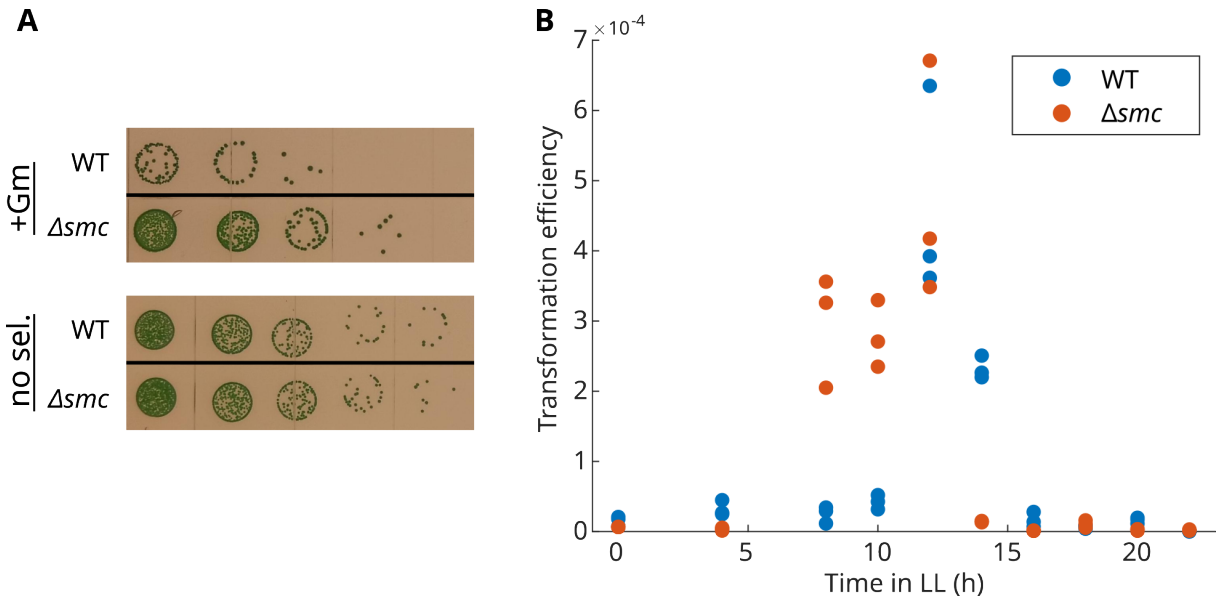

Figure 1.5. Natural transformation in WT and Δ*smc* mutants.
(A) Example of a single timepoint (ZT 10) assessing natural transformation efficiency and comparison between WT and Δ*smc* cells. DNA-incubated cultures were serially diluted and spotted onto plates with (+Gm) and without (no sel.) antibiotic selection corresponding to the marker on the transformed plasmid. (B) Calculated transformation efficiency for WT and Δ*smc* over a 24-hour circadian window. Each point represents one biological replicate (i.e. independent transformation reaction). Three biological replicates were assessed at each timepoint.

Chapter 2

Visualizing Cyanobacteria in High-Resolution

2.1 Introduction

Cyanobacteria form an ancient phylum of organisms that have been on earth for around 3 billion years. As a model prokaryotic system, cyanobacteria offer many unusual features not found in other bacteria. They possess extensive compartmentalization and intracellular organization, a *bona fide* circadian clock, and an evolutionary link to chloroplasts, among others. Cyanobacteria may be best known as model organisms to study photosynthesis, but have also been used to study circadian rhythms, prokaryotic motility, cellular differentiation, natural product synthesis, and as a platform for biosynthetic engineering.

In *Synechococcus elongatus* PCC 7942 (hereafter S7942), an organism in which a great deal is understood about photosynthesis, genetics, physiology, and the circadian clock, much less is known about the cell biology of the organism and how it might change over a circadian cycle. With the goal of creating a circadian cell atlas, I have developed methods for revealing the internal structures of S7942 cells using cryo-focused-ion-beam (FIB) milling and cryo-electron tomography (together denoted CET). The internal organization of a single cyanobacterium (S7942 in this case) is beautiful to behold (Figure 2.1). The thylakoid membranes are neatly arranged with regular periodic spacing just inside of the plasma membrane. In some species, the light-harvesting phycobilisomes on the thylakoids form well-ordered linear arrays. The

icosahedral carboxysomes are positioned along the mid-cell, alternating with polyphosphate bodies. The carbon-fixing RuBisCO molecules within the carboxysomes are packed in a repeating paracrystalline array [31]. As part of my thesis research, I have collected high-resolution tomograms of S7942 grown under diverse environmental conditions. These include cells cultured under high and low light, with circadian light entrainment, and with high CO_2 atmosphere. These images provide new insights into the cellular organization of cyanobacteria. In this chapter, I summarize some findings of interest arising from this dataset.

2.2 Approach to data collection

Culture conditions

All cultures of *Synechococcus elongatus* PCC 7942 (hereafter S7942) were grown using BG-11 medium and standard techniques [25] under moderate intensity light at 150 μmole photons $m^{-2}s^{-1}$ μE light fluence rate at 37 °C. Fresh log-phase cultures of S7942 were diluted to OD_{750} 0.1 and dispensed into 5 mL aliquots in 18 mm glass culture tubes. Cultures were allowed to acclimate for 24 hours then transferred to 12 hours light:12 hours dark (LD 12:12) to entrain for at least 3 full dark cycles.

Cultures of *Synechococcus elongatus* PCC 7002 (hereafter S7002) were grown using A+ medium and standard techniques under moderate intensity light at 150 μE light fluence rate at 37 °C. High-CO_2-requiring (HCR) strains were grown in an enriched 5% CO_2 atmosphere at 100 μE light fluence rate. For induction of carboxysome biosynthesis, cultures were transferred to ambient air, IPTG was added to a final concentration of 1 mM, and allowed to induce for 5 hours before harvesting.

For strains expressing YFP-KaiC under control of an inducible promoter, liquid cultures were grown and entrained as above. At the beginning of the final light phase, IPTG was added to each tube to a final concentration of 1 mM. Cultures were allowed to grow for an additional 18 to 20 hours in LD prior to plunge-freezing.

For the circadian atlas, we aimed to sample cultures grown under LD 12:12 at 3 hour

intervals, from ZT 00 to ZT 21. Approximately 5 minutes before each time point, we removed a single tube from the incubator and concentrated the cells by centrifuging at 4500×g and resuspended to a concentration of OD_{750} 2.8

Plunge-freezing

Cells were centrifuged at 4500×g and resuspended to a concentration of OD_{750} 2.8 for plunge-freezing. Immediately prior to plunge-freezing, 9 μL of cell suspension were mixed with 1 μL of 50% w/v D-(+)-trehalose dihydrate (Chem-Impex) in water to act as a cryoprotectant. Samples were plunge-frozen on a manual plunging device (Max Planck Institute) in the following manner: 4 μL of prepared cell suspension were applied to a Quantifoil Cu 200 mesh R2/1 grid (EMS) mounted in the device, blotted until dry (approximately 4 seconds) using Whatman #1 paper, then plunge-frozen into a 50/50 w/w mixture of ethane-propane (Airgas).

Cryo-Fluorescence Microscopy

Cryo-Fluorescence Microscocopy was used only for YFP-KaiC cells. Frozen grids of cells expressing YFP-KaiC were visualized using a CorrSight inverted microscope (Thermo Fisher Scientific) using EC Plan-Neofluar 5x/0.16NA and EC Plan-Neofluar 40x/0.9NA air objectives (Carl Zeiss Microscopy), a 1344×1024 px ORCA-Flash 4.0 camera (Hamamatsu), and an Oligochrome light-source, with excitation in four different channels (405/488/561/640 nm); red (thylakoid autofluorescence) and green (YFP-KaiC) were used. Data acquisition and processing was performed using MAPS 2.1 and MAPS 3.6 respectively (Thermo Fisher Scientific). After acquiring a grid map at 5X magnification, regions of interest were imaged at 40x magnification, to identify single grid squares containing a monolayer of bacteria.

Cryo-Focused Ion Beam (FIB) Milling.

Grids with cyanobacteria were prepared using cryo-FIB milling as described in Chapter 4 using an Aquilos (Thermo Fisher Scientific) dual-beam instrument [32, 33]. Briefly, areas covered with a monolayer of cells were targeted first for coarse milling with an ion beam current of 0.10-0.50 nA, followed by fine milling using 10-50 pA. Lamella width was typically 10-12

um. Five to eight lamellae were prepared on each grid in one session, with a target thickness of 130 nm. See Chapter 4 for additional details.

Cryo-Electron Tomography

Lamellae were visualized on a Titan Krios (Thermo Fisher Scientific) operating at 300 kV accelerating voltage with a Gatan K2 Summit camera equipped with a Quantum energy filter. Regions of interest were determined based on a low mag overview, and correlation with cryo-fluorescence microscopy for samples expresing YFP-KaiC. Tilt series of cyanobacteria were obtained using SerialEM [34, 35] using both bi-directional and dose-symmetric [36] tilt schemes over a tilt range of +/- 60°, in increments of 2° or 3°, at a pixel size of 0.4265 nm or 0.2687 nm. Each tilt image was collected using electron counting mode and with dose-fractionation. For some tomograms (primarily those collected before 2020) exposure times for each tilt were adjusted to keep an approximately constant number of counts on the sensor. Tomograms collected after 2020 were acquired using a constant exposure time. The exposure scheme was changed to accommodate a new data processing pipeline in the Villa Lab using Warp [37]. Cumulative dose for each tilt series was usually between 120 to 180 e/A2.

Tomogram Reconstruction

The movies corresponding to each tilt were motion-corrected using MotionCor2 software [38]. Tilt series alignment and reconstruction was done using IMOD [39, 40, 41]. Tilt series were aligned using the patch-tracking modality, and reconstructed using weighted back-projection. If needed, individual tilts with excessive motion, poor contrast, or camera errors were excluded from the final reconstruction. Non-linear anisotropic diffusion (NAD) filtering was applied to tomograms in IMOD.

Ribosomal and RuBisCO Template Matching

To determine the location of ribosomes within the tomogram, we used template matching, 3D alignment, and classification. Tilt series were preprocessed using Warp v1.0.9 [37] for

sub-frame motion correction and 3D-CTF estimation. Tilt-series were then aligned using IMOD as above and imported into Warp for final reconstruction.

Template matching of ribosomes within tomograms was performed in Warp. First, manually picked particles were aligned and averaged, and this structure was subsequently used as an initial template. All extracellular particles were initially discarded based on cell boundaries defined in Dynamo [42] . Obvious false positives (e.g., membrane segments) were manually excluded. The remaining particles were used for 3D alignment and classification in Relion v3.1 [43]. Particles were subject to successive rounds of binary classification with a large (500 Å) mask, the smaller class which contained particles that did not appear as ribosomes were removed from subsequent rounds. This was done until the two classes reached about equal population, both clearly representing ribosomes. Coordinates and orientations of the remaining particles were imported into Amira (Thermo Fisher Scientific) for visualization.

Ribosome positions and orientations were refined in M [44] and the resulting alignments were used to refine tilt-series alignment for KaiC template matching and averaging. KaiC template matching and initial averaging were done as described above.

Membrane Segmentation

Membranes were detected using TomoSegMemTV [45]. Tomogram segmentations, membrane annotations, and ribosome annotations were prepared with Amira (Thermo Fisher Scientific).

2.3 Novel Features of Cyanobacterial Ultrastructure

In tomograms of S7942 we repeatedly found structures and features of interest that have been only sparsely described in previous microscopic studies. Due to the structural preservation and native contrast afforded by CET, recent studies have identified features in cyanobacteria such as bacterial gap junctions that provide a channel for intercellular communication in *Anabaena sp.* PCC 7120 [46] and potential thylakoid biogenic centers in *Synechocystis sp.* PCC 6803 [47].

Here, we describe two plasma-membrane associated structures found in S7942, along with other ultrastructural features.

2.3.1 Unidentified plasma-membrane associated structures

The simpler of the membrane-associated structures we tentatively call "tables" (Figure 2.2 A,B), named for their appearance on the cytoplasmic face of the plasma membrane. These structures are about 30 nm across at the membrane attachment point and about 25 nm in height measured from the membrane. We find two or three of these structures per tomogram, where they are visible due to the membrane standing perpendicular to the optical axis. They are likely present in other tomograms, but are not easily visible due to an oblique projection. In some instances, we find a filament passing through the table crossing the periplasmic space, and exiting the cell. Because of this feature, it is possible that the "tables" represent a secretory complex. S7942 is known to possess a type II secretion/type IV pilus system that is involved in secretion of a biofilm supressor [48], natural transformation, [3] and phototaxis [49]. Additionally, recent CET in diverse Gram-negative and Gram-positive heterotrophs have identified a plasma-membrane associated *flagellar Type III* (fT3SS) secretion system that bears a striking similarity to the structures we observe in S7942 [50]. Their function is unknown, but speculated to be involved in flagellar assembly. However, these Type III secretion systems are found attached to the *periplasmic* face of the plasma membrane, rather than the *cytoplasmic* face as is the case in S7942. Moreover, cyanobacteria are not known to possess flagella [51] so it is unclear what role these "table" structures have in S7942.

We also observe "syringe"-like structures attached to the cytoplasmic face of the plasma membrane (Figure 2.2 C,D) that are reminiscent of the barrel and plunger assembly of a medical syringe. These structures measure about 40 nm across at the membrane attachment point and 40 nm in height measured from the membrane. Moving outward from the membrane, the syringes comprise five layers stacked parallel to the membrane that form the "barrel" of the syringe, then a stalk capped by a shorter layer parallel to the lower layers forming the "plunger" of the syringe.

The syringe structures are present in many tomograms, some containing as many as five. They are found at the poles and along the axis of the cell, often in close association with each other, forming clusters of two or three. As is the case with the "tables", the syringes are likely present in more cells, but may not be easily visible due to an oblique projection. We also find filaments passing from the syringes, crossing the periplasmic space, and exiting the cell. These may also be related to the cyanobacterial secretion system. However, the syringes do not resemble the known structures of the Type IVa pilus machinery [52]. It is presently unclear what role these "syringes" have in S7942, and whether they are related to the table structures.

2.3.2 Fine features of thylakoid ultrastructure

Cyanobacterial thylakoids are dynamic structures that adapt to ambient light conditions [53]. They form a network of double-membraned lamellar compartments that are covered in phycobilisomes and contain the photosystems and associated components that convert light energy to chemical energy in the form of ATP and NADPH. The abundance of thylakoids and photosynthesis proteins inside the cell is regulated in response to ambient light conditions [54, 55]. When light levels are high there are fewer thylakoid membranes; conversely, more thylakoid membranes are synthesized during lower-light conditions to efficiently capture scarce light energy [56].

One of the most striking features in our cyanobacterial tomograms are the thylakoid membranes and how they split, merge, and cross over each other within the 3D volume of a tomogram. We have captured many instances of thylakoid membranes in unexpected configurations. In dividing cells we find thylakoid membrane fission events, including strands of membrane that bridge both daughter cells (Figure 2.2 E).

In cyanobacteria transferred from moderate light (150 μE) to very low light (5 μE) for 3 days prior to plunge-freezing, we find an increase in the average number of thylakoid membranes compared to cells grown only at moderate light levels. In several cases, we also find large ordered stacks of what appear to be phycobilisome peripheral rods (Figure 2.2 F) extending from the

innermost thylakoid layer into the cytoplasm by about 400 nanometers. Smaller extensions of these rods are also visible *in between* thylakoid membranes. These extended arrays have not been previously reported and may be part of a transitory state as cells become adapted to low light conditions. Perhaps the phycobilisome rods are held "in reserve" and are distributed as more thylakoid membranes are synthesized.

2.3.3 Challenges in identifying and averaging KaiC from nighttime localized foci

One of my thesis aims was to visualize the KaiC, core protein of the cyanobacterial circadian oscillator. The core circadian oscillator in cyanobacteria comprises three proteins—KaiA, KaiB, and KaiC. Together, these three proteins signal time by the phosphorylation state of KaiC over a 24-hour period [1]. During subjective day, KaiA promotes auto-phosphorylation of KaiC and during subjective night KaiB antagonizes KaiA, thereby promoting auto-phosphatase activity of KaiC [1]. Furthermore, the KaiABC-based clock is part of an integrated circadian network that regulates transcriptional activators and repressors that ultimately change gene expression based on time signals from the oscillator and the environment.

Based on previous research with fluorescently labeled circadian clock proteins, we know that KaiA, KaiB, and KaiC localize to the cell poles during subjective night to form a discrete focus [57]. CikA, another key protein in the cyanobacterial circadian network, also co-localizes with the KaiC focus. This same study also determined that the mechanism of localization is conserved through to *E. coli* because heterologously expressed KaiC is able to form distinct foci separate from inclusion bodies. The formation of these foci may be critical for circadian rhythmicity, as strains defective in foci formation also exhibit irregular circadian phenotypes. However, the effectors responsible for bringing or keeping KaiC near the cell poles are not well understood, nor are their biological functions outside the context of clock-protein localization. Additionally, the organization and overall structure of these foci is unclear.

The aim of using CET to visualize KaiC foci was twofold. Firstly, to determine the

organization of clock components within the foci and to map intermolecular contacts that would not necessarily be captured in single-particle structural studies [58, 59] . Secondly, to identify cellular features such as thylakoid perforations or biogenic sites that promote KaiC localization. To address both of these aims, we used cryo-fluorescent microscopy to find YFP-KaiC foci in cells and CET to target the same cells for high-resolution electron microscopy (Figure 2.3).

We plunge-froze cells with induced YFP-KaiC expression at ZT 18 and ZT 20, the time of maximal focus abundance [57]. In initial tomograms of cells with induced YFP-KaiC expression, we identified filamentous bundles that we believed to be YFP-KaiC based on correlation with fluorescent microscopy data. However, we could not reproduce these filaments under identical growth conditions. In subsequent tomograms of cells with YFP-KaiC overexpression, we reliably and repeatedly observed amorphous YFP-KaiC foci (Figure 2.4 A). The KaiC regions varied in size from around 200 nm to 400 nm in diameter depending on the plane of the cell captured during the FIB-milling process. The region is recognizable in TEM by the lack of ribosomes and overall internal disorder. At higher magnifications, potential KaiC hexamers can be observed. In order to identify KaiC particle positions and orientations, we applied 3-D template matching and subtomogram averaging techniques as described in Chapter 3 using a downsampled map of PDB:2GBL [60]. However, we were unable to recover unbiased averages using alignment with and without a reference, nor with different mask sizes. The results of Figure 2.4 B are typical of averages of random noise. This outcome suggests that the starting particle pool still contains excessive false negatives. Tomograms of amorphous aggregates are difficult to parse due to close packing of neighboring particles. An alternative future route to identify KaiC *in situ* is to use 2-D template matching, a recently developed technique that is able to eliminate more false-positives than the 3-D template matching used here [61, 62]. This approach will require new data to be collected similar to single-particle cryoEM, including acquiring 2-D images only rather tilt series, and at higher magnifications.

2.4 A Circadian Atlas

Because cyanobacteria have large-scale physiological and metabolic changes in response to daily fluctuations in light levels [2], we reasoned that there would be correspondingly large changes in cellular organization. In particular, we wanted to observe potential changes in ribosome distribution over the course of a circadian day as a measure of chromosome compaction as cytological support of the work in Chapter 1. Ribosome placement determined using CET previously has been used as a method to infer chromosome geometry [63, 64]. At the same time, we hoped to capture "day-and-night" differences between daytime and nighttime cells.

In the course of ribosome template matching and averaging for the cyanobacterial atlas (Figure 2.5 A), we found that about 25 to 40% of ribosomes within an individual cell could be found in a dimerized state (100S particles). In diverse bacterial species dimerization is a method to down-regulate ribosome activity when when adapting to low-nutrient environments. In the photoautotrophic cyanobacterium S7942, transcription and translation levels are reduced with the onset of darkness because of the loss their primary energy source. Previous work has demonstrated that under dark conditions, a rise in the alarmone ppGpp increases expression of the ribosomal hibernation promoting factor gene (*hpf*) which in turn leads to a shift in the pool of active ribosomes [65]. In other bacteria, HPF promotes ribosome dimerization during nutrient stress [66]. In *E. coli* proteomics, Rmf and RaiA have also been shown to be involved in ribosome hibernation during nutrient limitation [67]. Given these lines of evidence, cyanobacteria may use HPF-mediated ribosome dimerization as a mode of regulation during the dark phase of the circadian cycle. Because ribosome biogenesis is energetically costly [68], such post-translational regulation allows cells to rapidly respond to a decrease in light availability during the dark phase while preserving total biosynthetic capacity for later activation when the light phase inevitably returns.

Here, we found ribosome dimers within cyanobacteria that are joined at the 30S subunit (Figure 2.5 B,C). This configuration is markedly different from that of 100S particles reported in

E. coli [69] and in *B. subtilis* [70]. In all three cases, the dimer interface is located on the 30S subunit. However, in S7942, the two 50S subunits are rotated by about 90° relative to each other whereas the 50S subunits in *E. coli* and *B. subtilis* are rotated by nearly 180° so that they point away from each other. Our current approach is to identify ribosomes and 100S particles within cells frozen at different circadian times, and to determine how the spatial and class distributions change over a 24 hour interval. Towards this goal, we have plunge-frozen WT S7942 samples at three-hour intervals over the course of a circadian day, prepared them using FIB milling (see Chapter 4), and collected over 100 tomograms spanning the circadian day for an ongoing study. Additionally, we have developed a ribosome distribution analysis pipeline (Chapter 3) to promote creation of a cyanobacterial circadian atlas.

2.5 Carboxysome Biogenesis

Carboxysomes are bacterial microcompartments that contain the enzyme Ribulose Bisphosphate Carboxylase/Oxygenase (RuBisCO), which is responsible for fixing carbon dioxide to Ribulose Bisphophate (RuBP) in the first step of the Calvin cycle to eventually form biomass[71, 72]. However, RuBisCO can also accept oxygen as a substrate, which leads to the energetically wasteful photorespiration cycle that releases CO_2. Early in cyanobacterial evolutionary history, this was not an issue because of the low oxygen and high CO_2 atmosphere in the Precambrian Era [73]. Our modern atmosphere is high in oxygen and low in CO_2, which makes the carbon-fixing activity of RuBisCO very inefficient. One adaptation to a high O_2 in photosythetic organisms is a *CO_2 concentrating mechanism* (CCM) that improves the catalytic function of RuBisCO.

The cyanobacterial CCM includes bacterial microcompartments called carboxysomes that physically sequester RuBisCO and create an environment rich in CO_2 around it. The full biological literature on the carboxysome is too extensive to summarize here, so I will mention a few salient points. The *ccm* operon contains genes encoding carboxysome shell proteins

and scaffolding proteins that arrange RuBisCO within the carboxysome [72]. The shell of the carboxysome is essential for cellular viability at ambient conditions, and deletion of any of shell proteins found in the *ccm* operon leads to *high CO_2 requiring* (HCR) phenotype [74]. On a cellular level, deletion of the *ccm* operon leads to loss of carboxysomes and RuBisCO becomes distributed uniformly within the cytoplasm. Additionally, when only *ccmK*—the gene encoding the major shell protein—is deleted, RuBisCO becomes localized at the cell pole, trapped as a *procarboxysome* (PC) [71]. These procarboxysome-only cells also have an HCR phenotype.

For this collaborative project with the J. Cameron lab, University of Colorado, we set out to visualize *de novo* carboxysome biogenesis within the native cellular context using high-resolution CET. Traditional resin-embedded transmission electron microscopy (TEM) and fluorescence microscopy have been used to investigate the structure and dynamic biogenesis of carboxysomes, but cannot reveal fine details such as shell interactions with RuBisCO. To this end, we used an inducible carboxysome system in *Synechococcus elongatus* PCC 7002 (hereafter S7002) from the Cameron Lab to visualize *de novo* carboxysome biogenesis. In these constructs, the *ccm* operon is expressed from an inducible promoter by the addition of IPTG. We also used a strain lacking *ccmK1*, which is arrested at the procarboxysome stage.

We used the standard CET pipeline to prepare three *ccm* mutants of S7002: a Δ*ccm* strain in which the entire *ccm* operon is deleted and replaced with an antibiotic resistance cassette, a Δ*ccm* +*ccm* strain in which the entire *ccm* operon is reintroduced under control of an IPTG-inducible promoter, and a Δ*ccm* +*ccm*Δ*K1* strain in which a version of *ccm* lacking the major shell protein *ccmK1* is reintroduced under control of an IPTG-inducible promoter. These strains were visualized according to the same methods outlined in this chapter. Downstream analysis for template matching of ribosomes and RuBisCO are as above.

Figure 2.6 shows tomograms of cells captured at different stages of carboxysome maturation. Through template matching using a RuBisCO template and segmentation, we were able to pick out individual RuBisCO complexes within carboxysome shells. A surprising discovery was that we were able to capture a dividing carboxysome, in which a facet grows inwards to part

the RuBisCO by "slicing" rather than "pinching" as was expected from TEM observations of resin-embedded samples [71].

2.5.1 Plasma membrane budding

In many of the tomograms of cells with induced *ccm* expression we found double-membraned vesicles located between the plasma membrane and outermost thylakoid membrane (Figure 2.8 B,C,D). These are often found at the convergence of thylakoid membranes at the cell pole. In some cases, we also found D-shaped membrane loops extending out from the plasma membrane (Figure 2.8 A). These loops are intriguing because they may be biogenic precursors to thylakoid membranes.

The origin of thylakoid membranes remains elusive and past proteomics and TEM data have shown that there is no direct contact between the thylakoids and the plasma membrane[56, 47]. Our ability to observe this putative intermediate stage may be due to the the newly induced carboxysomes present in the cell. Without CO_2 fixation, cyanobacteria are unable to grow biomass, including lipids for new membrane synthesis. Within a few hours of induction, the new carboxysomes are able to provide fixed carbon to the cell, thereby jump-starting cellular metabolism. When the cells were frozen after 5 hours of *ccm* induction, they were captured in a highly biosynthetic state.

2.6 Outlook

In recent years, high resolution CET has become more accessible to biologists through the development of optimized hardware, software, and analytical approaches. These techniques allow us to probe complex cellular architecture. Among prokaryotes, cyanobacteria provide an endlessly fascinating playground for understanding genetic regulation, environmental adaptation, and intracellular organization.

As part of my thesis research, I have acquired hundreds of high-resolution tomograms of *Synechococcus elongatus* PCC 7942, a model cyanobacterium, grown under an array of light

conditions and at different circadian times. I believe that there is a wealth of knowledge within these tomograms, and even a cursory survey outlined here has revealed unknown structures (the "syringes") and unusual macromolecular configurations (phycobilisome stacks and 100S ribosome dimers). In order to make the most of these data, my intent is to release the most interesting tomograms to the cyanobacterial community through EM data repositories. These will be accompanied by a publication focusing on ribosome distribution and dimerization throughout the circadian cycle, while highlighting other features of interest.

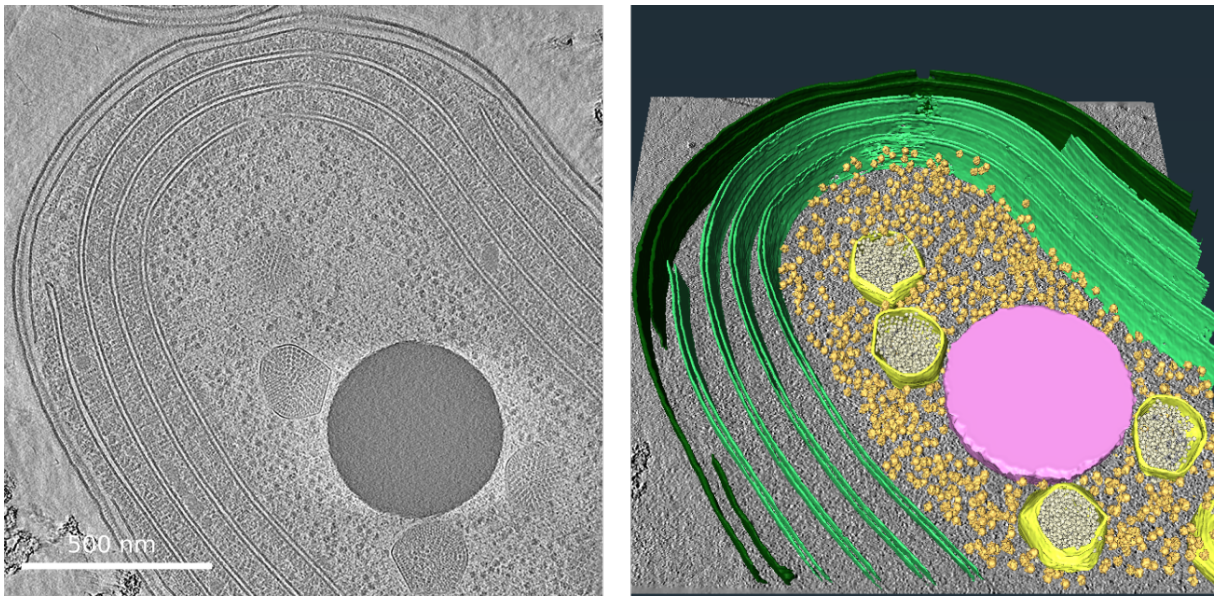

Figure 2.1. Tomogram and segmentation of *S. elongatus* PCC 7942.
Left: Tomogram of S7942, showing organized compartmentalization typical of cyanobacteria. Outer and plasma membrane are clearly visible, as are thylakoid membranes, carboxysomes, and a polyphosphate body. Right: Segmentation of same tomogram highlighting features of interest. Dark green: outer and plasma membrane. Light green: thylakoid membranes. Yellow shells: carboxysomes, with RuBisCO. Pink: polyphosphate body. Goldenrod: ribosomes. *Scale bar: 500 nm.*

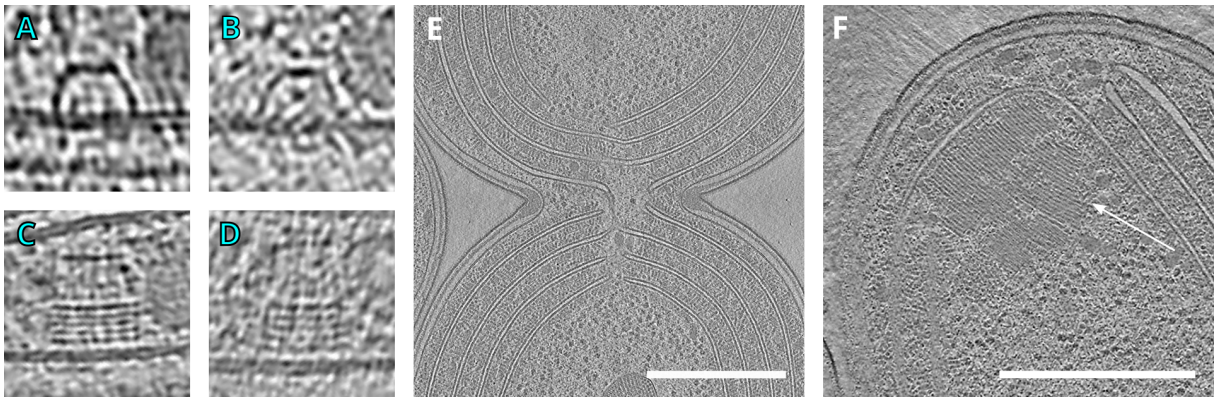

Figure 2.2. Other structures and features of interest in *S. elongatus* PCC 7942.
(A,B) Examples of unknown "table"-shaped structures in S7942 attached to the cytoplasmic face of the plasma membrane. The "tables" measure about 30 nm across at the base. (C,D) Examples of unknown "syringe"-shaped structures in S7942 attached to the cytoplasmic face of the plasma membrane. The "syringes" measure about 40 nm across at the base. (E) Tomogram of dividing S7942 mid-septation. Thylakoid membranes bridging both daughter cells are visible. (F) Large stacks of unknown phycobilisome-related proteins (arrow) in S7942 grown under very low-light conditions. *Scale bars: A-D 60 nm box size; E,F 500 nm.*

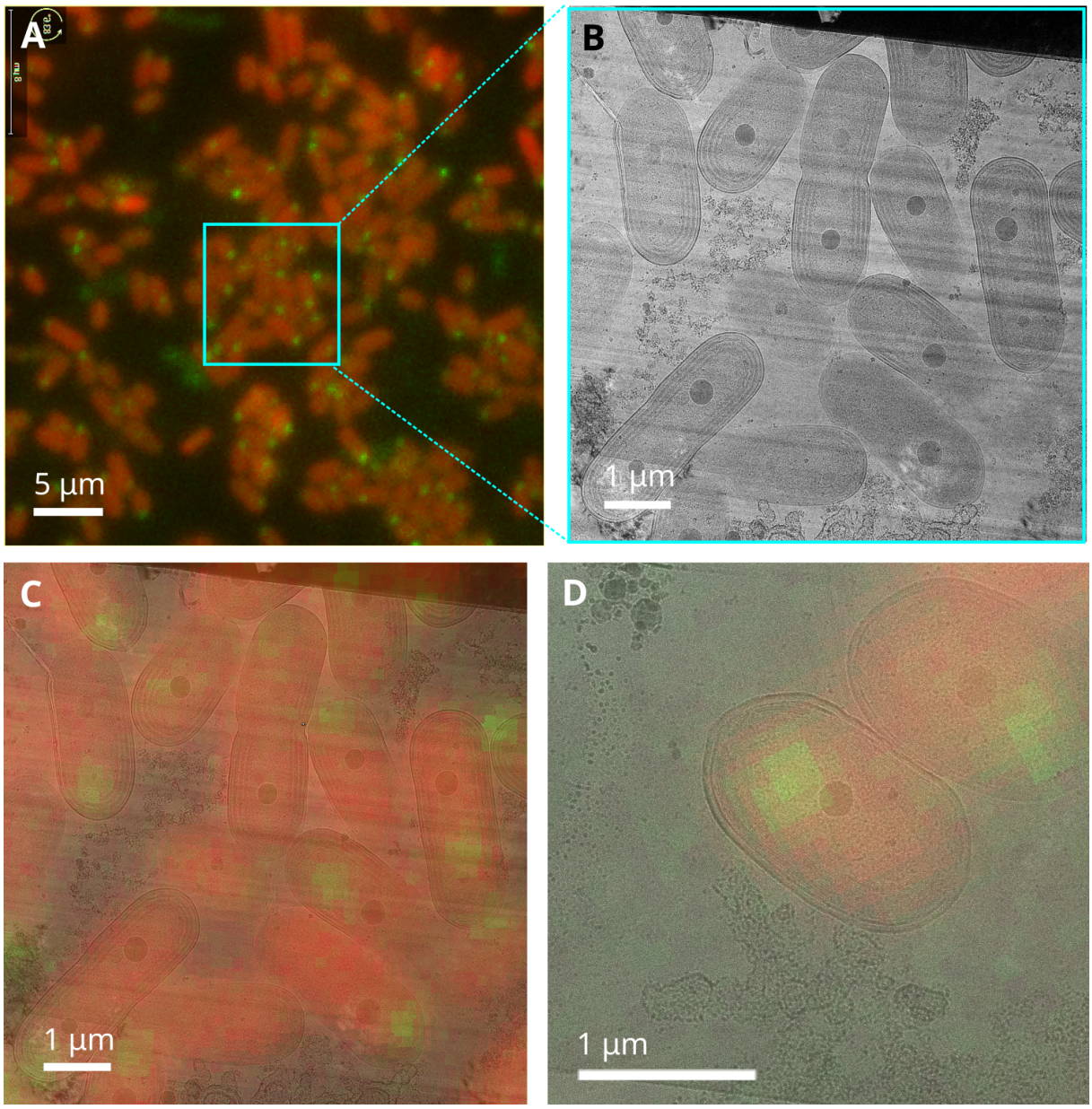

Figure 2.3. Cryo-correlated light and electron microscopy (cryo-CLEM) of YFP-KaiC in *S. elongatus* PCC 7942.
(A) Cryo-fluorescence micrograph of a field of vitrified cyanobacteria expressing YFP-KaiC. (Red: thylakoid auto-fluorescence. Green: YFP-KaiC) and the corresponding lamella (B) after cryo-FIB milling. (C) Overlay of fluorescent and EM images of region of interest. (D) Single bacterium targeted for tomography. *Scale bars: A 5 µm; B-D 1 µm.*

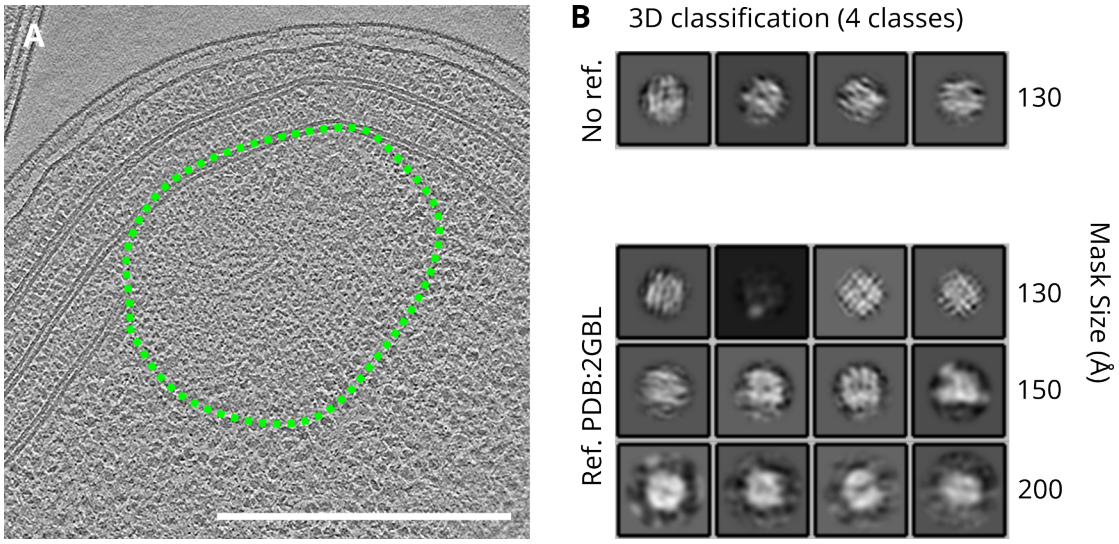

Figure 2.4. Template matching and averaging of *in situ* KaiC.
(A) Tomogram of YFP-KaiC focus in S7942 with induced expression of YFP-KaiC. Location of focus matches correlative-FM data. Extent of KaiC region is indicated by the green dashed-line. Individual hexamers of KaiC are visible within the region. (B) 3D classification and alignment strategy of template-matched KaiC particles in preparation for IBC (see Chapter 3). Classification without a reference is indistinct and appears to be strongly driven by noise. Classification and alignment with a PDB-derived template (PDB:2GBL) yields similar results to no reference at small (130 Å) mask sizes. Larger masks (200 Å) yield classes that superficially resemble the template. *Scale bar: A 500 nm*

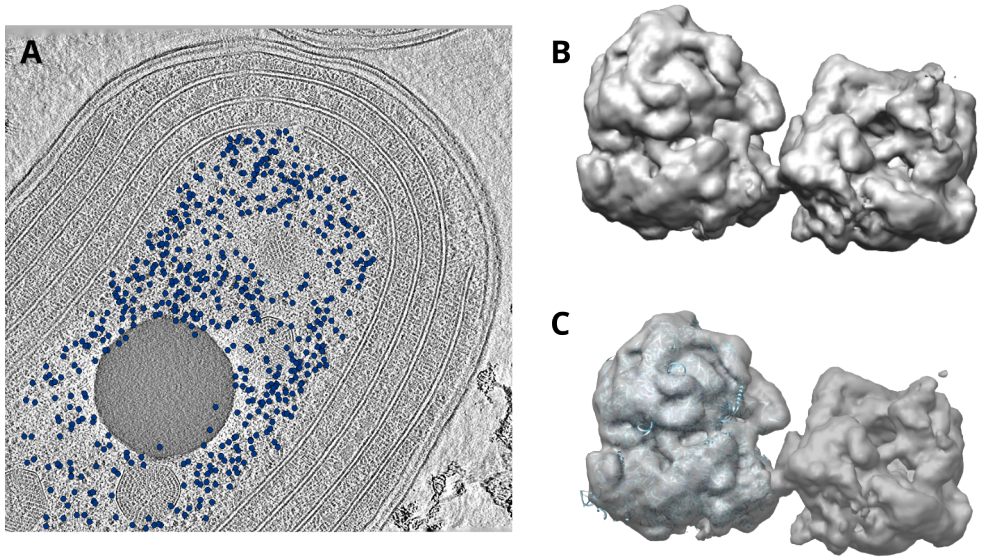

Figure 2.5. Ribosome template matching and ribosome dimers in *S. elongatus* PCC 7942. Ribosome template matching results in S7942 in same tomogram as Figure 2.1. Initial matches have been curated to keep only points inside the cytoplasmic area. (B,C) Averages of ribosome dimers in S7942 identified *in situ*. Each ribosome appears joined at the 30S subunit. (C) Same as (B), but with the model of *E. coli* ribsome PDB:5MDZ fit into one of the ribsosome maps.

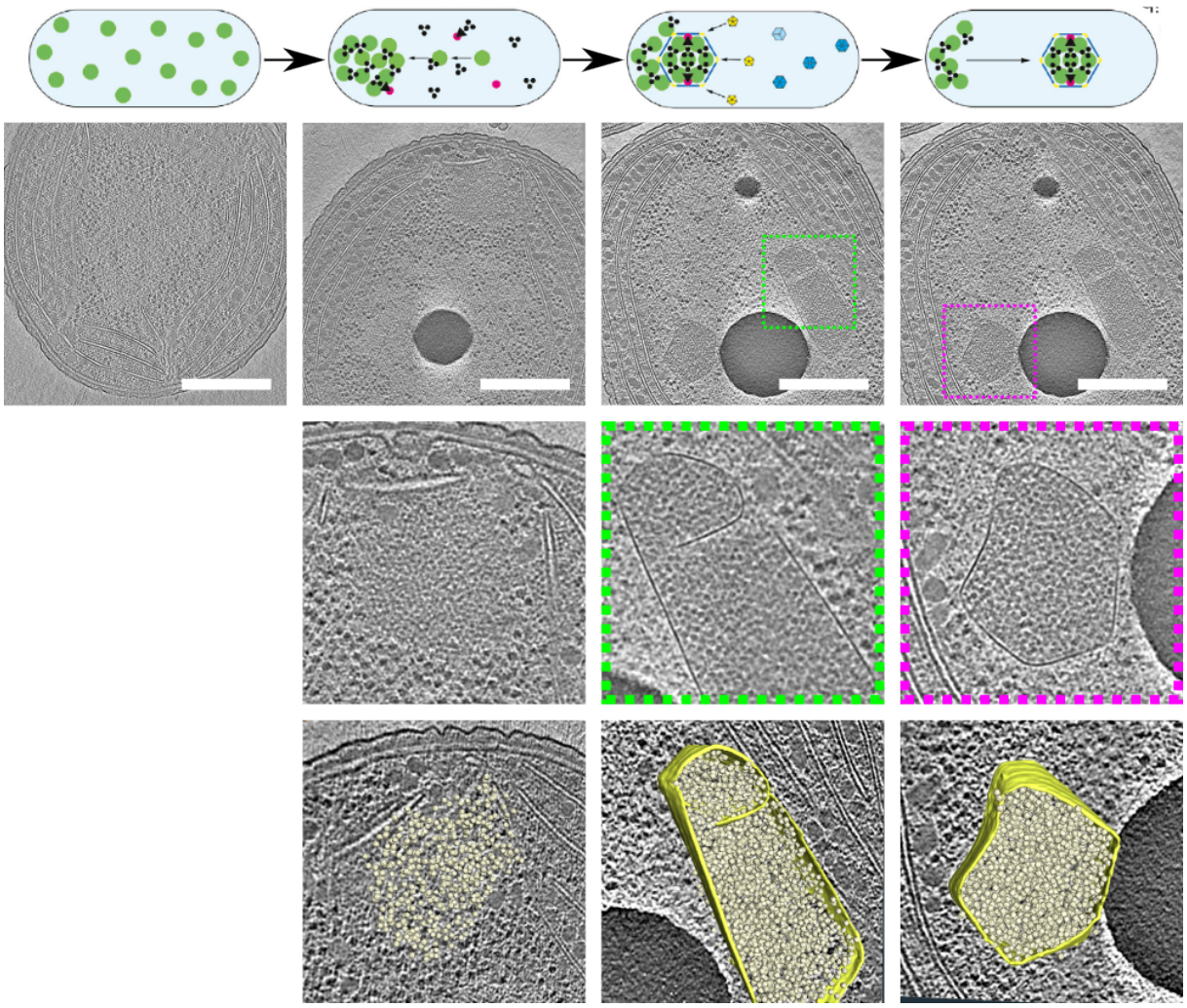

Figure 2.6. Carboxysome biogenesis progression in *S. elongatus* PCC 7002.
Top row: schematic of carboxysome maturation progression from carboxysome-free, to pro-carboxysome, to initial encapsulation, to final mature carboxysome. Below, second row, are tomograms of cells corresponding to each stage of carboxysome biogenesis, and a magnified image (third row) of RuBisCO aggregates in either procarboxysomes, or maturing carboxysomes. Bottom row shows 3D segmentations of the views in row three. RuBisCO molecules are picked out in pale yellow and carboxysome shells are shown in bright yellow. *Scale bars: 500nm.*

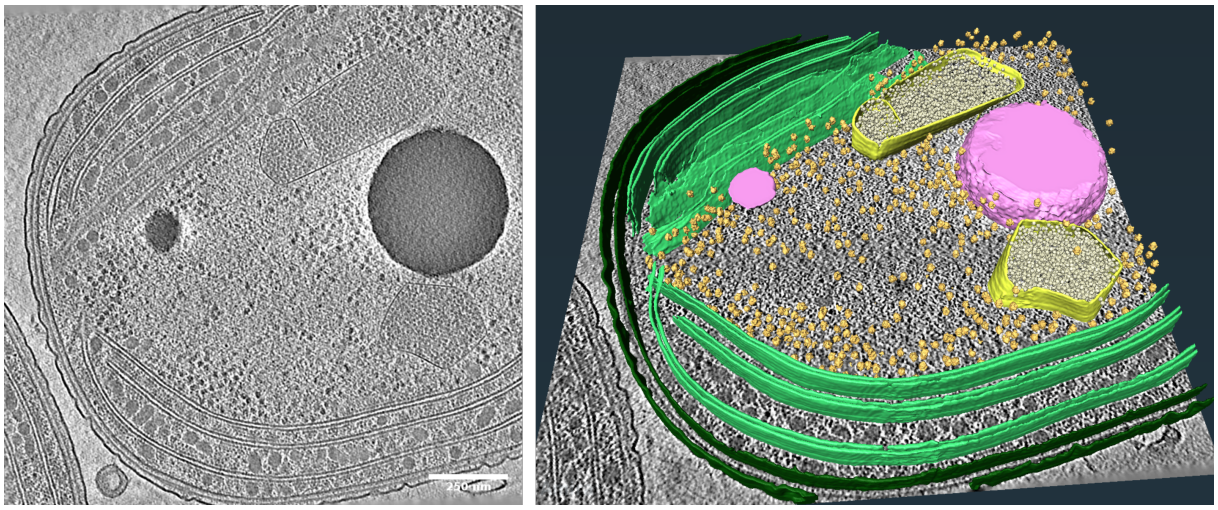

Figure 2.7. Tomogram and segmentation of newly induced carboxysomes in *S. elongatus* PCC 7002.
Left: Tomogram of carboxysome formation was induced in Δ*ccm* +*ccm* for 5 hrs prior to freezing samples. Right: Segmentation of tomogram to emphasize features of interest. Dark green-inner/outer membrane; Light green-thylakoid membranes; Pink-polyphosphate body; Yellow and white-carboxysomes and RuBisCO; Goldenrod-ribosomes. *Scale bar 250 nm.*

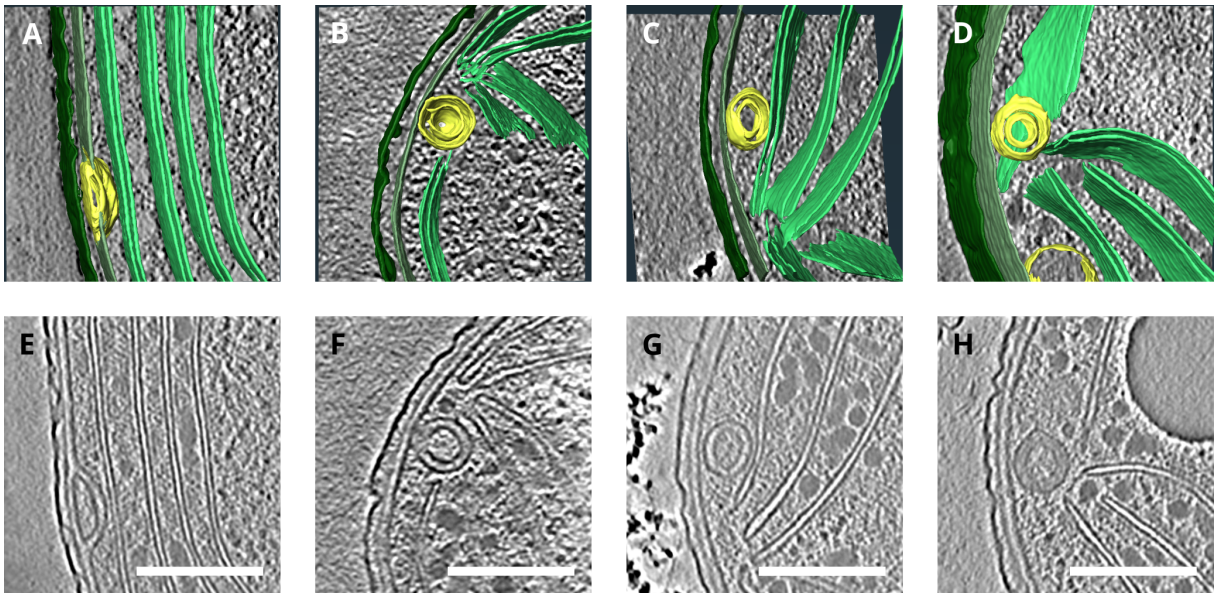

Figure 2.8. Plasma membrane vesicles in *S. elongatus* PCC 7002.
(A-B) Segmentation of a "D-loop" vesicle budding from the plasma membrane. (C-D) Segmentations of tomograms containing double-membrane enclosed vesicles. Dark green: outer and plasma membrane. Light green: thylakoid membranes. Yellow: vesicles of interest. (E-H) Tomograms corresponding (A-D). *Scale bars: E-H 250 nm.*

Chapter 3

Iterative Binary Classification

3.1 Introduction

One major goal of *in situ* cryo-electron tomography (CET) is to be able to identify macromolecules within their native cellular context [75]. This approach differs from single-particle analysis cryoEM (SPA), which aims to visualize purified macromolecules at the highest resolution possible. In SPA, hundreds of thousands of molecules, each of which is called a "particle" are picked from a large series of two-dimensional images, and are averaged together over many refinement iterations to derive the highest possible resolution structures [43]. Over the course of this iterative process, low quality particles are discarded and the final high-resolution structure often contains only 25% of the original dataset.

For those particles that cannot be purified, one common alternative is to use *in situ* CET to collect tilt series of the structure of interest, then use sub-tomogram averaging (STA) techniques to crop and analyze individual sub-volumes [75]. Sub-volumes are first identified by using a 3D cross correlation score by matching a reference template over the entire tomogram. These sub-volumes are treated as independent particles and can be used as in SPA, where low-quality particles are discarded in favor of a high-resolution final structure.

When seeking to understand a molecule's role in its native cellular context and for molecular sociology, it is desirable to unequivocally identify particles within a tomogram that corresponds to a molecule of interest—an *identity-first* approach. In contrast, most studies to date

aim to build a high-resolution structure of the molecule of interest—a *resolution-first* approach. A resolution-first considers only the "best" instances of the molecule, and discards those that may be the molecule of interest but do not contribute to structural resolution due to factors such as sample quality or orientation. When *in situ* tomography is used to study the structure of macromolecules in a cellular context, we are limited in both the total number of particles analyzed and the total number of tomograms available to analyze at once. Additionally, for questions of molecular distribution, particles of interest must be analyzed on a per-tomogram basis. Because of minor differences in tomogram quality, only the highest quality particles from each tomogram would be kept in the final pool if we follow a resolution-first approach as in SPA or STA. For an identity-first particle analysis, we need a method to reliably identify whether a selected particle belongs to one particular group of particles. While particle quality and resolution are useful in making this assignment, strictly using a resolution-first approach leads to many false negatives and loss of information.

One simplistic method would be to use 3D correlation scores from template matching to select only particles that have a sufficiently high score. In an ideal scenario, there would be clear two-peaked distribution of correlation scores (Figure 3.1A) where particles are either obviously false or obviously true. In such a case, it is simple to pick a threshold value that excludes false particles. However, because CET data often have a low signal-to-noise ratio, the the distribution of scores for "false" and "true" particles have significant overlap (Figure 3.1B). Setting a threshold to exclude as many false particles as possible would exclude many true particles as well, and choosing a lower threshold would admit too many false particles. Additionally, in real-world data the distributions of false and true particles would be added together (i.e. indistinguishable without *a priori* knowledge), and the resulting sum would appear as a single-peaked distribution. In such a case, choosing an appropriate threshold becomes impossible.

In order to improve the particle identification rate, we created Iterative Binary Classification (IBC) as an alternative strategy to reduce the false positive matching rate. This strategy relies

on multiple rounds of classification and elimination to vote on the identity of a given particle and determine its likelihood of being a "true" particle. Here, we demonstrate the use of IBC to identify likely ribosomes in the synthetic mycoplasma JCV1 Syn3A in a collaborative project with the Schulten (UIUC) and Glass (JCVI) groups [63]. The goal of identifying ribosomes *in situ* was to serve as a model for creating hypothetical space-filling chromosome geometries in an effort to model the molecular dynamics of an entire synthetic cell system. Developing these methods also furthered the goal of using ribosomes in S7942 to track chromosome compaction.

3.2 Methodology

JCVI Syn3A cells were cultured off-site using established protocols [76] and passed to us for vitrification and CET. Tilt-series pre-processing and ribosome template matching were done using Warp [37]. For each tomogram of interest a correlation threshold was chosen to include as many true positives as possible. Cell boundaries lying just outside of the membrane were manually defined using Dynamo [42] and used to exclude points located outside of the cell. Example tomograms of JCVI Syn3A are shown in Figure 3.2A,B.

The remaining set of particles was exported as a .star file for alignment and classification in Relion [43]. Particles were first aligned to a reference without classification using a tight mask. After initial alignment, the particles were classified without reference and without alignment into two classes. For this classification-only step, as larger mask was used to allow the area surrounding a particle to help drive classification. Class averages were manually inspected and the poorer class was removed from the pool of particles. The poorer class generally contained around 10 to 20% of the total number of particles. Binary reference-free classification with a large mask was repeated until the proportion of particles in the two classes was split near 50/50%, which indicated that Relion was no longer able to distinguish the two classes. At this step, class averages were manually inspected to verify that both classes looked similar. All particles were kept, then checked for duplication or any outliers.

For binary classification with bootstrapping, each round of classification was run with 20 iterations. Particle identities were tracked over each iteration and the classification score was calculated based on the percentage of time that a given particle was sorted into the "good" class.

3.3 Results

We first performed conventional template matching using a template generated from about 200 manually picked particles (Figure 3.2C,D. About 1600 candidate particles were identified after removing points located outside of the cell boundaries and filtering through a matching score threshold (Figure 3.2D). This set of particles includes many false-positive matches such as membrane segments.

Iterative binary classification appears to eliminate approximately half of the particles originally picked from template matching with a low correlation cutoff (Figure 3.3F). The first few rounds showed a clear difference in quality between the "good" and "bad" classes, with about 15% of particles in the bad class. At the end of the iterative binary classification process, both classes resembled each other with a near 50% split. Points that originally were located on the membrane and contained membrane segments were effectively removed from the particle pool (Figure 3.3G). Additionally, the final ribosome count per cell volume matched estimates from biochemical purification.

In order to test the reliability of per-particle classification, each round of classification was repeated for twenty iterations (Figure 3.4A) and particle classifications were tracked over each iteration. Because initial classes are randomized, we are able to calculate the probability that a given particle would be classified as "good". After each round, we kept only the particles that classified as "good" 50% of the time or greater. We find that over 75% of the initial particle pool reliably classifies into the good class. Over the course of 3 rounds of 20 iterations each, the score distribution of remaining particles becomes narrower and shifts towards higher scores (Figure 3.4B). We concluded that over multiple rounds of classification IBC preferentially and

reliably keeps particles that resemble each other.

3.4 Outlook

The field of high-resolution cryoEM has progressed rapidly over the past decade and high-quality EM maps for single particles are routinely achievable. SPA has become a powerful part of the biologists toolbox accessible through the expansion of university and national facilities. However, CET for *in situ* structural biology is still limited by physical considerations such as cell thickness and the complexity of the intracellular environment [77]. Additionally, many of the questions that CET is poised to answer rely on identifying macromolecules within a complex environment and there exists a need to develop techniques to assign identity.

To this end, we have developed the IBC workflow to iteratively sort particles based on group similarity. The workflow is built on top of existing cryoEM software, and can be implemented with any software package that can do 3D classification. Compared to standard SPA approaches, IBC expands the mask used to classify particles in order to account for surrounding material. This is particularly advantageous for eliminating false particles located on membranes. The classification strategy in IBC is also different. By limiting the number of classes to two and only running reference-free classification without alignment, we are essentially asking the software to make a yes-no (binary) judgment for each particle on whether it matches the expected particle or not. After multiple rounds, this classification strategy stabilizes when the software is no longer able to reliably distinguish two separate classes (Figure 3.3F). By running IBC on the same particle pool, we also find that particle classification is largely stable. Particles that are assigned as ribosomes reliably re-classify as ribosomes across multiple rounds and iterations (Figure 3.4B).

Our implementation of IBC has some disadvantages that limit its applicability. As with SPA approaches, particle number is still a limiting factor. Because particle classes are assigned based on similarity to the existing pool, a small starting pool would allow more spurious matches

due to a higher signal-to-noise level. In our data, ribosome identification was only robust with at least 500 particles. Below that level, we could no longer reliably distinguish between the "good" and "bad" classes. This limitation presents difficulties when trying to identify proteins that exist in low copy-numbers inside the cell. In such cases, it would be necessary to aggregate data from multiple tomograms, which may be difficult if the tomograms vary in quality.

Additionally, we have used IBC only for classifying ribosomes *in situ*. These particles are large and numerous cytosolic macromolecules that are "easy" to work with. Many particles of interest may not have such advantageous features. Less ideal particles may be too small or may be membrane anchored. Small particles present greater difficulty for template matching techniques due to a lower signal-to-noise ratio and may lead to a poor initial particle pool for IBC with many false particles. In tomograms of cyanobacteria overexpressing YFP-KaiC, the close proximity of particles within the KaiC region lead to poor template matching results with many overlapping points. Our attempts to apply IBC to identifying KaiC *in situ* in cyanobacteria proved to be unsuccessful (see Chapter 1.5). Membrane-bound proteins would necessarily include the membrane, which may dominate the classification process, leading to poor discrimination between "false" and "true" particles. In the same line of inquiry, it is unclear how to select the best stopping criteria for IBC. We selected a simplistic stopping criterion when particle classes are split 50/50 because it represents the point where a particle is just as likely to be classified as either good or bad. However, one could also design more complex criteria to consider the resolution of the final particle pool.

Lastly, our implementation of IBC does not have a method to validate the accuracy of particle assignments. In our example of ribosome distribution in JCVI Syn3A, we have corresponding biochemical data demonstrating good agreement with the estimated number of ribosomes per unit of cellular volume. It is likely that IBC would be used in conjunction with orthogonal methods when used to assign particle identity. One potential method would be to tag the protein of interest and find the additional density in EM maps.

Despite these obstacles to the broad application of IBC for *in situ* tomography, we believe

that our initial investigation marks an important shift in approaching tomographic data analysis from an *identity-first* rather than *resolution-first* approach. IBC itself will likely be little used due to rudimentary development, but the principle of relying on particle group-similarity scoring to sort into "good" and "bad" classes is important. Software development and image analysis techniques are constantly evolving, and future developments will certainly improve our ability to identify macromolecules within tomograms of complex cellular environments.

3.5 Acknowledgements

Chapter 3, in part, is published as Benjamin R. Gilbert, Zane R. Thornburg, Vinson Lam, Fatema-Zahra M. Rashid, John I. Glass, Elizabeth Villa, Remus T. Dame, and Zaida Luthey-Schulten. "Generating Chromosome Geometries in a Minimal Cell From Cryo-Electron Tomograms and Chromosome Conformation Capture Maps", Frontiers in Molecular Biosciences, vol.8, 2021. The dissertation author was a secondary investigator and author of this paper. Figures 3.2 and 3.3 and corresponding captions are adapted from material prepared for the above publication.

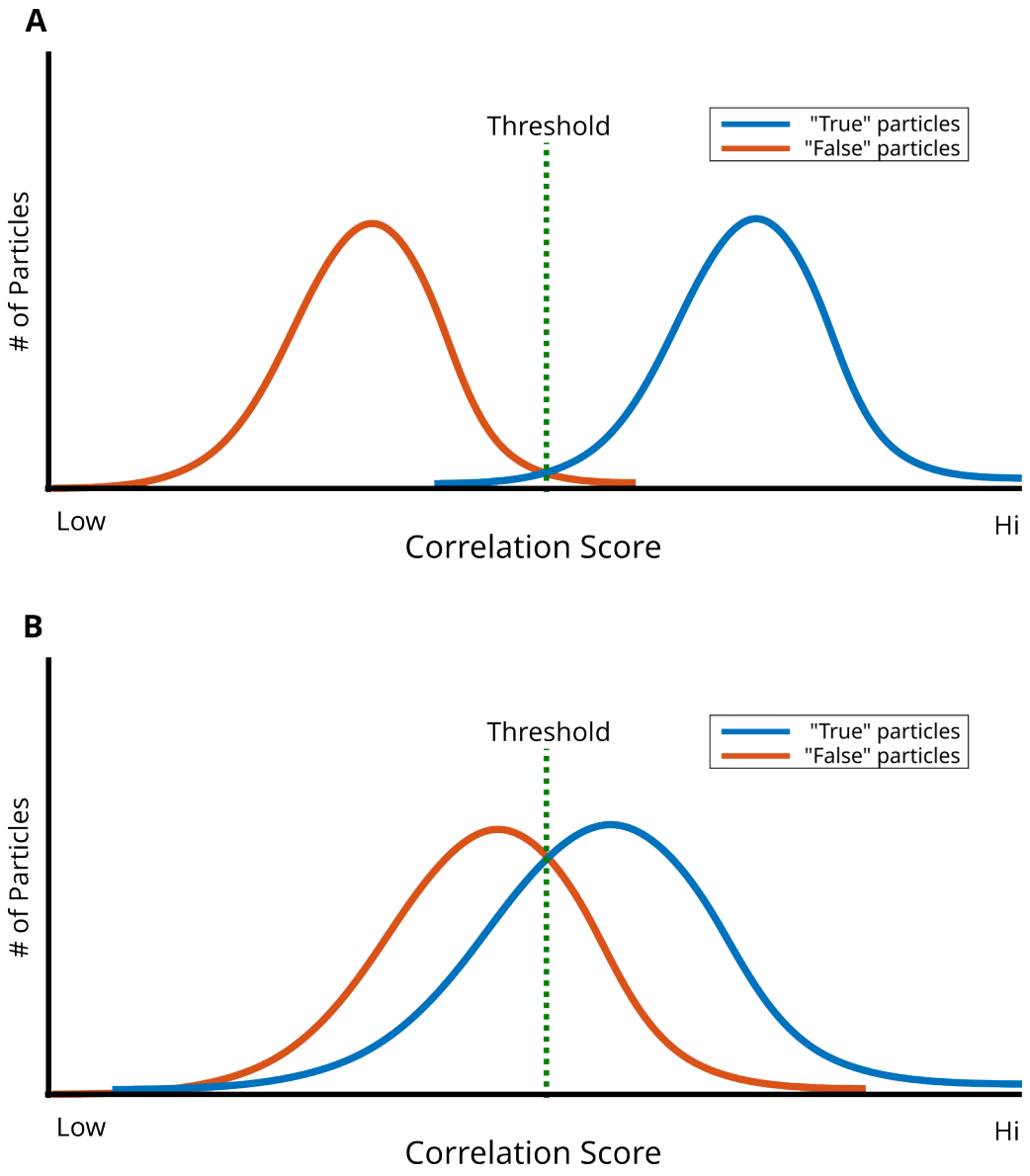

Figure 3.1. Thresholding strategies for particle identification.
(A) Schematic of an idealized template matching case where the correlation score distribution for false and true particles are well-separated such that a threshold can found that reliably excludes the majority of false particles while retaining true particles. (B) A less ideal template matching case where correlation scores for false and true particles have a large overlap. In such a case, no possible threshold can be identified that provides sufficient discriminatory power to select for only true particles.

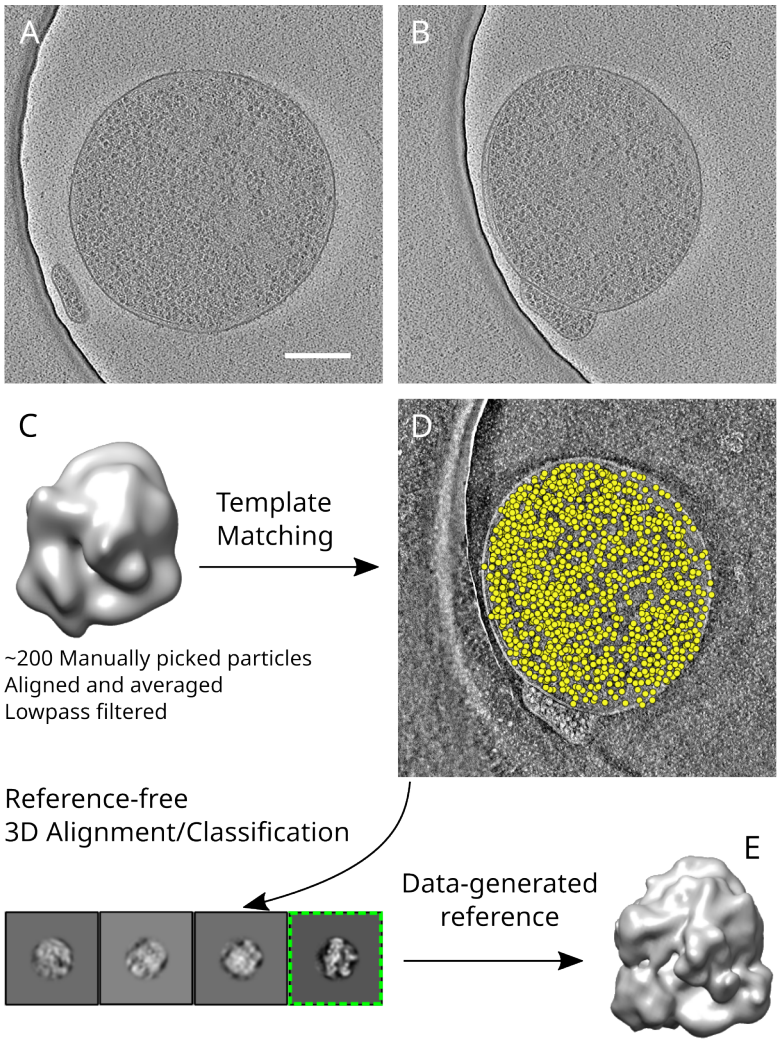

Figure 3.2. Iterative Binary Classification, Part 1.
(A,B) Slices through tomographic reconstructions of two JCVI-Syn3A cells. Scale bar 200nm. (C) An initial average generated from 200 manually picked ribosomes was used as a reference for template matching in JCVI-Syn3A tomograms. (D) Initial template matching results of (B) showing matched positions as yellow dots. Template matching results were filtered with a low threshold to remove some false positives. Additionally, all particles outside of the cell were manually excluded. Note that the initial template matching pool still contains false positives e.g., membrane segments. (E) Template matching results from multiple tomograms were used to create a data-generated ribosome map in Relion using reference-free 3D alignment and classification.

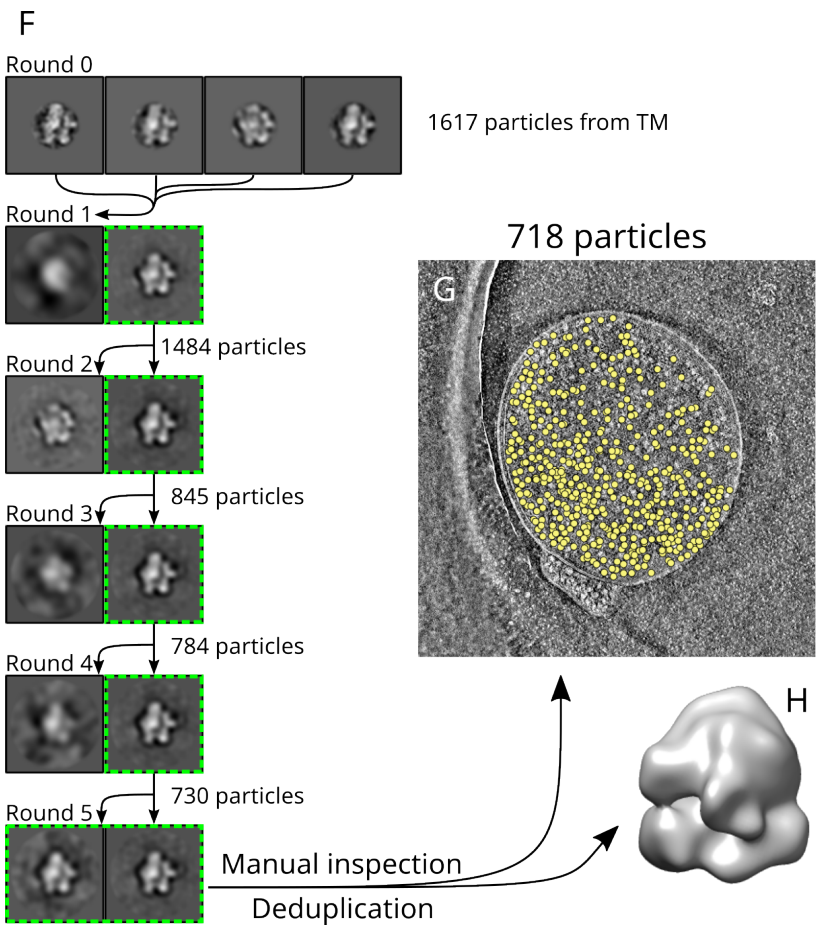

Figure 3.3. Iterative Binary Classification, Part 2.
Continuation of Figure 3.2. (F) Round 0: At the beginning of the iterative binary classification scheme, particles from each tomogram are aligned and classified separately, using the data-generated ribosome as a reference and a tight mask (250 A). Rounds 1-5: Reference-free 3D classification without alignment is used to separate the particles into two classes. This is done using a large mask (500 A). Only the class that most resembles the reference (green outline) passes to the next round of reference-free 3D classification. This continues until the two classes resemble each other, and both are kept. (G) After binary classification, the results are de-duplicated and manually inspected to remove any remaining false positives e.g., membrane segments. (H) Subtomogram average of the ribosomes from one single tomogram, kept at the end of the iterative binary classification workflow.

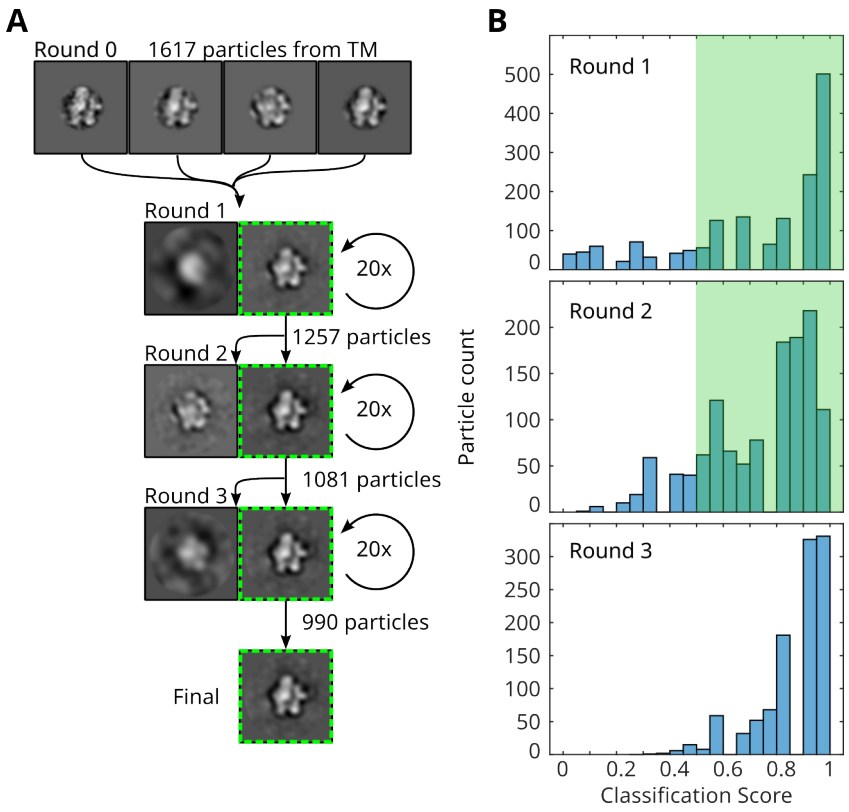

Figure 3.4. Evaluation of IBC via bootstrapping.
(A) Representative schematic of bootstrapping process, adapted from Figure 3.3. Each round of classification is run with 20 iterations to determine the classification score for each particle. Particles with a score better than 0.5 are kept and passed to the next round of classification. (B) Distribution of classification scores in each round of bootstrapping. The classification score is the proportion of time that each particle was placed into the "good" class. For Rounds 1 and 2, the shaded green areas represent those particles with a classification score greater than 0.5 that were passed onto the next round of bootstrapped IBC. After Round 3, no particles were removed.

Chapter 4

Practical approaches for cryo-FIB milling and applications for cellular cryo-electron tomography

4.1 Introduction

A major goal in biological imaging is to visualize macromolecular complexes and the intricate networks they form at high-resolution *in situ* with minimal artifacts. However, most commonly accessible techniques lack sufficient resolution (such as fluorescence light microscopy) or sufficient cellular context (such as single particle cryo-EM). Cryo-electron tomography is a high-resolution imaging modality that can visualize macromolecular structures *in situ* in a near-native state in their cellular context [78]. However, specimen thickness is a major limitation with cryo-ET and other electron microscopy techniques. Due to multiple electron scattering, specimen thickness is limited to less than 400 nm at 300 kV [79], which is well below the size of eukaryotic cells and most bacteria.

One approach to overcome this limitation involves sectioning cells under cryogenic conditions using a microtome [80]. However this approach is technically demanding and introduces visual and structural artifacts that arise from the the sectioning process [81]. Recent work has adapted the versatile focused ion beam (FIB) instrument for cryo-electron microscopy applications as a method to generate thin sections through cellular material, yielding unprecedented

insight into eukaryotic and prokaryotic cell biology [82, 83, 84, 47, 46, 85, 86, 87, 88, 89, 90, 91, 77, 92, 93, 94, 95, 96, 97, 98]. This technique offers significant advantages including relative ease of use, minimal artifacts, and the ability to target specific cells for high-resolution cryo-ET.

Focused ion beam (FIB) microscopy and milling has been used in materials science as a method to thin samples for analysis and to create micro/nanoscale patterns [99]. The operation uses a tightly focused (5–10 nm) beam of ions, typically gallium, that rasters over the sample [100], similar to the beam of electrons in conventional scanning electron microscopy (SEM). Secondary electrons are generated by the ion beam's interaction with the sample, which can be detected to form images. Furthermore, the relatively large mass of gallium ions can be used as a tool for micro/nano machining by selectively ablating material from a specimen. In this manner, the FIB can be used to precisely remove material above and below a region of interest to leave a thin section—a lamella—that remains supported by the unmilled material around it. FIB milling sample preparation is usually performed in a "Dual-Beam" instrument with both FIB and SEM columns for simultaneous milling and multi-perspective imaging. These instruments are also typically equipped with gas-injection systems that allow targeted metal deposition or modification of milling characteristics [101]. For cryo-FIB applications, these instruments are equipped with a stage cooled to liquid nitrogen temperatures to maintain samples at cryogenic temperatures and an airlock quick-loading system to introduce cryogenic specimens into the chamber under vacuum. This allows cold samples to be transferred into and out of the instrument while avoiding atmospheric ice contamination and to be milled at liquid nitrogen temperatures for several hours.

This chapter will briefly describe practical principles and procedures for cryo-FIB milling including considerations for upstream sample preparation, downstream TEM tomography, and evaluation of sample quality as part of a typical cryo-ET workflow (Fig. 4.1). A closely related technique using cryo-FIB liftout can be used for much thicker samples such as tissue blocks [102, 103, 104], but will not be discussed in this chapter. At this time of writing, commercial dual-beam instruments can be outfitted with third party cryostages/quickloader systems such

as the Quorum PP3006 cryo-stage, the Leica EM VCT500, and the Hummingbird Scientific cryotransfer system. In this chapter, we will describe a typical FIB milling protocol using the Thermo Fisher Scientific (TFS) Aquilos, a dual-beam FIB/SEM platform that includes a cryo-stage/quickloader system. However, many of the general principles should be applicable across instruments.

4.1.1 Principles of Operation

Cryo-FIB milling is most easily performed using a dual-beam focused-ion-beam/scanning-electron-microscope (FIB/SEM) that allows simultaneous monitoring and processing of the sample. The SEM column is mounted vertically onto the chamber and the FIB column is mounted at a 52° angle relative to the SEM such that the beams intersect. This intersection point, the beam coincidence point, is defined as the working distance of the microscope. In a well aligned system, the beam-coincidence point should be located at the stage eucentric height (Fig. 4.2).

Samples for cryo-FIB milling are typically prepared on TEM grids by plunge-freezing (see Section 4.3.1). The grid is positioned at the beam-coincidence point and oriented such that its surface forms a low incident angle (typically 5–10 degrees) relative to the FIB column (Fig. 4.2C). Milling thus results in lamellae that are nearly parallel to the substrate and long enough to contain enough material of interest as detailed in Section 4.1.2. The FIB is used to mill away material by continually rastering over the sample in a user-specified pattern to gradually ablate material. When starting a lamella, the milling patterns are set $\sim$2 um apart, and are gradually brought closer together to reach the target thickness, $<$200 nm. Additionally, the ion-beam current is reduced as the lamella becomes thinner in order to afford more control over the milling process and to minimize beam damage. The final target lamella thickness should be informed by the biological question and any downstream analysis (e.g. subtomogram averaging or membrane segmentation) (see Section 4.3.3). Typical lamellae thicknesses may range from 85 to 250 nm, and typical TEM pixel sizes may range from 0.2 nm to 2 nm (see Section 4.3.3).

Platinum Sputtering and GIS deposition

Vitrified biological samples are not conductive, and thus often result in beam-induced charging. This charging effect can be detrimental during milling and also during TEM imaging that leads to low quality images. A platinum sputtering system can be used to reduce charging by depositing a thin conductive layer on the sample. The sputtering system may be built into the chamber or immediately outside the chamber as part of a cryo-stage/quickloader installation, both enabling sputtering to be performed on cryogenic samples without excess contamination.

For cryo-FIB milling, an organo-platinum gas injection system (GIS) is used to coat the surface of the cold grid before lamella milling. The gas is released into the chamber close to the sample and immediately condenses on the cold grid. When exposed to the ion beam, the organic component is partially sublimated, leaving a metallic/organic film behind [105]. This residual platinum is essential for protecting the leading edge of the lamella during the milling process to prevent uncontrolled milling that will form "curtain" artifacts [100]. Additionally, the platinum layer acts as structural support that prevents lamella cracking during subsequent handling.

Stage and Shuttle

Up to two grids previously clipped into an autogrid support (Note 3) can be loaded into the specimen shuttle (Fig. 4.2A,B and Fig. 4.3E) for insertion into the microscope. The grids are held in place by a metal spring flap that contacts the edge of the autogrid and maintains thermal contact. In order to minimize atmospheric ice contamination, the shuttle is transferred from the loading station to the microscope under vacuum using a sealed transfer arm (Fig. 4.3A), via a pumped airlock system (the quickloader Fig. 3J). Additionally, the shuttle has a spring-loaded "door" that covers the grids whenever the shuttle is removed from the loading station or the microscope stage to minimize atmospheric ice contamination.

The shuttle holds the grids at a 45° angle relative to the vertically mounted SEM column (Fig 4.2B and Fig. 4.3E). During operation, the stage may be tilted anywhere from 0° to 45° relative to the horizontal stage position. The FIB column and platinum GIS needle are mounted

52° relative to the SEM (Fig 4.2C). The stage is capable of XYZ positioning as well as rotation about the Z-axis (the optical axis of the SEM), and tilt about the X-axis (the direction of sample insertion). Consequently, there is one XYZ position that brings the milling target to the beam-coincidence point. The rotation angle is determined by the mounting position of the FIB column, and tilt is determined by the specific sample and lamella requirements.

Stage Temperature Control

The stage is actively cooled by nitrogen gas flowing through a heat exchanger (Fig. 4.4A). Nitrogen gas from the source is split into two lines, each passed through a flow regulator, then into a hollow copper coil (Fig. 4.4B) immersed in a liquid nitrogen dewar (Fig. 4.4C) to reach liquid nitrogen temperature. The cooled nitrogen gas is then passed to the microscope chamber through a vacuum-isolated tube to minimize thermal loss. Nitrogen gas exits the chamber through return lines through the vacuum tubing, and is vented into the liquid nitrogen dewar to prevent frost formation that may potentially block gas flow and to prevent depositing liquid nitrogen in the lab environment.

Within the chamber, one of the lines of cooled nitrogen gas is passed through the lower part of the stage. The specimen is located on the upper part of the stage and is cooled by thermal conduction with the lower stage. The second line is passed through the cryo-shield, a separate anti-contamination fixture that has a large surface area to adsorb residual water molecules in the chamber. The stage and shield nitrogen flow rates are regulated separately from the input nitrogen line by the dedicated flow controller. Temperatures are monitored and recorded by computer software through thermocouples embedded in the stage and shield.

4.1.2 Considerations for Sample Milling Angle and Orientation

The target milling angle depends on the specimen. Typically, a large milling angle relative to the grid surface will result in shorter lamellae (ie measured from the front edge to the back edge) due to reduced cross sectional area (Fig. 4.2D). High milling angles may be useful

to create lamellae in thicker specimens or in specimens where it is difficult to identify a cell at low angles. Conversely, low milling angles result in longer lamellae, but may be more prone to obstruction from surrounding material or may make it difficult to identify a cell due to the nearly parallel viewing angle. Practically, it is best to mill lamellae at as low an angle (i.e., as parallel to the substrate as possible) for two reasons:

1. The lamella angle limits the tilt range of tomography in the TEM, contributing to resolution anisotropy [106].

2. Milling at low angles results in long lamellae, maximizing the usable area for tilt-series acquisition.

The lower limit to milling angle is set by sample geometry–at low angles, the edge of the autogrid or the grid bars will block the beam from reaching the grid square surface. This lower limit is about 11° stage tilt, corresponding to a beam incident angle of about 4° with respect to the grid surface. The upper limit to milling angle is set by the TEM stage. Due to the pre-tilt of the lamella, in one tilt direction on the TEM stage, the apparent sample thickness will be greater than compared to the other direction, corresponding to a greater relative tilt between the lamella and the beam. The apparent thickness of the sample increases proportionally to 1/cosine of the stage angle and at high TEM stage tilt angles, the sample will become too thick to image. If the initial lamella angle is too high, it will unnecessarily limit the range of TEM stage angles for tilt series acquisition. This upper limit for lamella milling is typically around 22° on the SEM stage, corresponding to an incident angle of about 15° (see Note 1). In general, ”tall” cells such as yeast and many eukaryotic cells may be milled at a higher angle than unicellular bacteria, which require low milling angles to generate enough usable area.

In order to mill at low angles, special autogrids are available with a cutaway notch that increases accessibility at low stage tilts. The milling notch on the autogrid should be oriented to face towards the FIB source–the clipped grid should be rotated so that the notch is at the top

position in the shuttle. To help with orientation, we routinely mark the autogrids with colored permanent marker to create a highly visible reference point (Fig. 4.2A).

4.2 Materials

4.2.1 Equipment

1. Dual Beam (FIB/SEM) instrument equipped with a temperature controlled stage capable of reaching -175 °C or lower and a vacuum transfer system. This chapter is focused on preparing specimens using the Thermo Fisher Scientific (TFS) Aquilos system with a built-in cryo-stage and quickloader, but general principles should be applicable across instruments.

2. Sample loading station/equipment and preparation tools compatible with the intended dual-beam instrument (Fig. 4.3).

3. Grid boxes.

4. Grid box opening tools.

5. Fine manipulation tweezers (e.g., Dumont #5).

6. Hot plate or hair dryer for warming/drying tools.

7. Liquid nitrogen transport dewar to hold gridboxes.

8. 4-liter liquid nitrogen storage containers.

9. Personal protective equipment (PPE) including cryo-gloves and goggles.

4.2.2 Consumables

1. Clean liquid nitrogen for sample preparation (NF grade; less than 5ppm moisture).

2. Pressurized liquid/gas nitrogen (to be regulated to 80 psi with a capacity of 30 L/min, sufficient for 12 hours use). This can be from either an in-house line or from a separate tank, e.g., a 230 L capacity, 230 PSI tank.

3. EM grids, quantifoil type or with other film substrate (see Note 2).

4. TFS regular autogrids, or cryo-FIB-autogrids.

5. TFS c-clips, also called clip-rings or clamprings.

4.3 Methods

On-grid cryo-FIB milling is suitable for many types of biological specimens including bacteria, yeasts, and mammalian cells. This section describes generalized methods suitable for these three common specimen types with considerations for different approaches required for each specimen. *These instructions assume that the reader is familiar with manipulating cryogenic samples to minimize atmospheric ice contamination and risk of sample devitrification.* **Always use appropriate PPE when working with cryogenic liquids**, and always pre-cool tools in liquid nitrogen before handling the specimens.

4.3.1 Sample Type Considerations

Cryo-FIB milling is adaptable to a wide variety of cell types (Fig 4.5). Here we offer some considerations on sample preparation and FIB milling for three broad categories of cells. This protocol is not applicable for bulk tissue samples due to major differences in vitrification procedures and FIB milling workflow [102, 103, 104, 94]. The categories are not strictly limited to only those cell types described, and we list some exceptions within the categories. In all cases, grid preparation is critical and users should optimize the following for their particular cell type:

1. Specimens should be thick enough to provide sufficient material to create a lamella. If the sample is too thin, the final generated lamella will be very short and contain almost

no cellular features of interest. For these cases, milling wedges can provide a longer electron-transparent window, albeit of varying thickness, on which tomograms can be acquired [95, 107].

2. Specimens should be thin enough to ensure proper vitrification and minimize crystalline ice domains.

3. An individual milling target (whether a single cell or clump of cells) should be large enough to support a 5-10 μm wide lamella suitable for cryo-ET.

4. Appropriate cellular density for the cell type. Note that cell density also affects sample thickness and vitrification.

Mammalian and Flat Eukaryotic Cells

These cells are generally flat and extend several tens of microns in diameter (Fig. 4.5D,G). Typically, the nucleus appears as a small hill in the center part of the cell. Each lamella made in these samples will be a partial section of a single cell. Examples include fibroblasts and other cells that are cultured on substrates, and some amoebae.

Grid Preparation

Cells may be grown directly on the quantifoil grid by seeding cells and allowing time for them to adhere. The grids should be made of non-cytotoxic material such as gold. Additionally, these grids may be treated with extracellular matrix such as fibronectin or poly-l-lysine to facilitate cell adhesion. If sterility is important, grids may be sterilized under a germicidal UV lamp prior to coating and seeding with cells. The appropriate seeding concentration and recovery periods should be determined empirically.

Some mammalian cells may be deposited on grids immediately before plunging, similarly to protein solutions for single-particle cryo-EM. In this case, adherent cells may be dissociated from the culture surface (using trypsin/EDTA) with the aim to create single cells with minimal

clumping. Cell clumps will lead to poor vitrification. Cells should be concentrated or diluted to a pre-determined concentration prior to plunge-freezing.

Evaluating grid quality and milling

In both seeded and deposited cells, the ideal specimen would have on average 1-2 cells per grid square (on a 200 mesh grid, $\sim$6000 μm^2 area) with minimal clumps (Fig. 4.5A). At the SEM, cells should appear well hydrated, and covered in a thin layer of ice (Fig. 4.5D,G). In some cases, the outline of the nucleus may be visible. Cells that are overblotted (i.e., too dry) may appear to be shrunken, starting to lift off from the substrate (for adherent cells), or have craters appearing on the surface.

Flat eukaryotic cells are typically milled at moderate to high stage tilt angles, from 15° up to 22°. FIB scanning patterns should be positioned to mill through the bulk of the cell in order to have sufficient support material to hold the lamella. Lamellae from cells may extend as far as 15 um in length and may be thicker at the rear due to FIB beam spreading. The lamella thickness can be made uniform through a final milling step with additional stage tilt as described in Section 4.3.2.

Yeast and Tall Eukaryotic Cells

These cells are smaller than flat cells, typically encompassing less than 10 um in diameter and have a roughly round shape (Fig 4.5E,H). This is likely due to the presence of a rigid cell wall that holds the cell shape. Each lamella made in these samples will have sections of multiple cells appearing side-by-side. Examples include *Saccharomyces cerevisiae*, *Chlamydomonas*. In some cases, large bacteria clusters such as filamentous *Anabaena* [46] lend themselves to milling in this manner.

Grid Preparation

These cells are typically deposited on the grid before plunging, rather than cultured directly on the grid. Cells should be diluted or concentrated to an empirically determined

concentration prior to plunge-freezing. In some cases (such as yeast) the cells are more tolerant of drying due to secreted extracellular polymers or the presence of a cell wall.

Evaluating grid quality and milling

Contrary to the case with flat cells, the ideal yeast specimen *should* have clumps of 5-10 cells, with 1-2 clumps per grid square (on a 200 mesh grid, Fig. 4.5B). Due to the relatively small size of yeast, these clumps are necessary to provide enough material to make reasonably sized lamellae. At the SEM, cells should appear relatively dry, but with enough ice to cover the cells and to bridge the gap between neighboring cells (Fig. 4.5E,H). As a rule of thumb, the clumps should look like steep hills. If there is negative curvature of the clumps where they touch the grid surface, the cells are likely overblotted. If needed, it is possible to mill individual yeast cells, but with a narrow lamella about 3 μm wide instead of 10 μm [108].

Yeast may be milled at moderate to high stage tilt angles, from 15° up to 22°. Milling patterns should be positioned to cut through the center of the clump of cells. As in the case with flat cells, a final milling step with additional stage tilt is recommended to make uniform lamellae.

Bacteria

These cells are generally too small (less than 5 μm in diameter) to mill individually. During blotting, rod-shaped bacteria (e.g *E. coli*, *B. subtilis*) will tend to lie down on the grid such that the long axis of the cell is parallel to the grid surface. Examples include most unicellular planktonic bacteria.

Grid Preparation

Bacteria are almost always deposited on the grid immediately prior to plunging. Cells should be diluted or concentrated to an empirically determined concentration prior to plunge-freezing with the aim to make a monolayer of cells embedded in media. The optimal concentration is highly dependent on the specific cell shape and the specific grid hole pattern used because the cells may slip through or become trapped by the holes. Bacteria are generally tolerant of

drying because of the large number of closely packed cells and secreted extracellular polymers [109]. However, the relatively large total cell mass can lead to poor vitrification. This issue can be alleviated through the addition of cryoprotectants such as trehalose immediately prior to plunge-freezing.

Evaluating grid quality and milling

The ideal bacterial specimen should have a uniformly flat monolayer of cells over each grid square (Fig. 4.5C), with the cells packed side-by-side. This arrangement will allow sufficiently long lamella with cells throughout. At the SEM, the ice should be just enough to cover the layer of bacteria, but without excessive hills or valleys (Fig. 4.5F,I). Generally, if each bacterium is well-defined, the sample is overblotted.

Bacterial grids should be milled at low to moderate stage tilt angles, from 11° to 15°, in order to maximize the number of cells captured in each lamella. This will also result in a long GIS platinum leading edge. If needed, the GIS deposition time can be decreased slightly. A final milling step with additional stage tilt may be useful for some bacterial samples, but is not always necessary for samples milled at moderate stage tilts.

For FIB milling, the lamella should be targeted near the center of the grid square for maximum tilt range at the TEM. Unlike the case with mammalian cells and yeast, it is difficult to target one individual bacterium for milling. Instead, the milling strategy relies on having a near complete grid square coverage to capture as many cells as possible in one single lamella.

Cryo-CLEM

Correlated light and electron microscopy (CLEM) of the same specimen is a powerful technique that allows targeting labeled cellular structures of interest for high-resolution EM [102, 110]. Cryo-CLEM combines the advantage of fluorescence microscopy to specifically locate organelles or proteins of interest and the advantage of TEM to visualize *the same object* at high-resolution in its native cellular context. A full description of CLEM is outside the scope of this chapter. For FIB milling, correlation can provide great advantages in determining areas to

mill, but also provides additional challenges for sample preparation including reduced throughput and increased atmospheric ice contamination due to additional imaging and transfer steps.

For typical mammalian and yeast samples, the cell density described above (about 1-2 cells or clumps per grid square) is typically compatible with cryo-fluorescent microscopy. For bacterial specimens, the cell density should be reduced to somewhat less than full coverage of the grid square in order to be able to resolve individual cells.

During FIB milling, the fluorescent data can be used to guide targeted milling of mammalian and yeast samples. For bacteria, milling is still done in non-targeted manner—while the fluorescent information is useful to screen individual grid squares for suitable cell coverage, ice thickness, and overall quality, the fluorescent data is more critical at the TEM to determine which specific cells should be targeted for tilt series acquisition.

There are commercially available cryo-fluorescence microscopes such as the Corrsight and the Leica Cryo-CLEM system. Additionally, aftermarket cryo-stage additions such as CMS-196 Linkam stage are available in addition to a number of custom made cryo-light microscopes [111, 112]. Recent work has also demonstrated cryo super-resolution microscopy to be compatible with a typical cryo-CLEM workflow [102, 111, 113, 114, 115, 116]. Key points to consider when acquiring cryo-fluorescence microscopes include stage temperature stability, anti-contamination features, and compatibility with existing EM instruments and workflows.

4.3.2 General FIB milling protocol

Before Starting

These steps should be done before the FIB session.

1. Culture and plunge-freeze specimens at the appropriate density (see Section 4.3.1) using your selected grid type (see Note 2). *Cells should be frozen on the carbon side of quantifoil grids.*

2. We recommend marking the autogrids with permanent marker before clipping to make

sample more visible when under liquid nitrogen (Fig. 4.2A). Avoid marking the milling notch of the cryo-FIB-autogrid due to potential beam interactions with the marker residue.

3. While working at liquid nitrogen temperatures, clip specimen grids into a cryo-FIB autogrid support. The grid should be clipped so that the cell side (the carbon side) is facing towards the flat surface of the autogrid so that cells are visible during milling (see Note 3). Clipped grids may be kept for several weeks in a liquid nitrogen storage dewar before subsequent processing.

4. If fluorescent correlation is required for targeted FIB milling, it should be collected beforehand.

When idle, our microscope is routinely kept in the following manner:

- At room temperature, the microscope chamber is pumped down to about 2×10^{-6} mbar.
- Heat exchanger flow controller set to 1 L/min for both stage and shield. This keeps the gas lines free of moisture.
- Preferably, the sample transfer arm (Fig. 4.3C) is attached to the microscope quickloader and pumped. This minimizes dust and moisture contamination inside the transfer arm and the quickloader.
- Typically, we keep the FIB source heating is turned off if the system is idle for more than a day, to conserve gallium. Otherwise the source may be left on for the next user. However, practices may vary among facilities depending on instrument usage frequency.

Day of Milling

Microscope Startup and Cooldown

1. Turn on the FIB and SEM beams, typically done by "waking" the microscope. Start the user interface, and inspect the system status as described in the following steps 2 - 4.

2. Check that the chamber base pressure is about 2×10^{-6} mbar. (see Note 4)

3. Check that the stage is empty.

4. Home the stage to reset stage coordinates and verify range of motion.

5. Check gas nitrogen source pressure and adjust to 80 psi. If the system is attached to a tank, check that the tank contains sufficient nitrogen for the session. Replace if needed.

6. Begin purging the heat exchanger gas lines by opening the flow controller to the maximum. Purge for at least 10 minutes.

7. Begin venting the transfer lid assembly (Fig. 4.3D). This step is necessary to remove residual moisture inside the lines.

8. Prepare for loading: turn on the hot plate on the preparation controller (Fig. 4.3H) and place required tools on it.

9. Fill a 4-liter dewar with clean liquid nitrogen for sample preparation. Make sure the nitrogen hose attached to the source is dry before filling to minimize ice contamination. Be sure to use appropriate PPE when handling cryogenic liquids.

10. Fill the heat exchanger tank with liquid nitrogen.

11. Start the temperature logging software to monitor and record stage and shield temperature.

12. Slowly insert the heat exchanger into the heat exchanger tank and ensure that it is seated appropriately. Monitor the stage and shield temperature until it stabilizes around -180 °C. Reduce the flow rate to 8.5 L/min to further reduce temperatures by about 3 °C. Allow the system to cool for an additional 30 minutes. (see Note 5) When the stage is at cryogenic temperatures, the chamber vacuum should improve considerably compared to the room temperature base pressure. On our system, the chamber pressure is around 7×10^{-7} mbar when the stage is at cryogenic temperatures.

Sample Preparation and Loading

1. Retrieve grid boxes containing the frozen, clipped specimens and have them ready in liquid nitrogen.

2. Insert the shuttle into the loading position in the loading station (Fig. 4.3A). Fill the loading station with liquid nitrogen, and allow to cool until the liquid is no longer boiling. Refill as needed. Keep the loading station covered with the standard lid to minimize atmospheric contamination while cooling.

3. Transfer the grid box containing the grids to the loading station and unscrew the lid to access the grids.

4. Place one grid into each slot of the shuttle, and rotate the grid in position so that the milling slot is at the top (Fig. 4.2A and Fig. 4.3E).

5. Secure the grids in the slots by turning the locking screw (Fig. 4.3E) at the top of the shuttle. Verify that the grids are secured by turning the shuttle to the vertical position and check that the grids remain in place.

6. Flip the shuttle into the vertical transfer position (Fig. 4.3B), and replace the standard lid with the transfer lid (Fig. 4.3D).

7. Press 'V' to vent the quickloader airlock (Fig. 4.3J) and retrieve the sample transfer arm. Ensure that the transfer arm valve is closed.

8. Attach the transfer arm to the transfer lid on the loading station. If present, secure the transfer arm with the locking clamps (Fig. 4.3C). Otherwise, securely hold the base of the transfer arm. Check that the shuttle grabber is in the 'open' position (Fig. 4.3G).

9. Pump the transfer lid airlock for 35–40 seconds, then open the transfer arm valve.

10. Vent the transfer lid airlock for 3 seconds, then close the venting line.

11. Open the sliding valve on the transfer lid to allow access to the shuttle.

12. While observing the shuttle, insert the transfer arm and close the grabber to hold the shuttle. Verify the hold by pulling the shuttle back slightly by a few millimeters. **The next two steps should be done quickly in succession to minimize contamination.**

13. Quickly and smoothly withdraw the shuttle completely to the back position, lock the transfer arm, and close the sliding valve on the transfer lid.

14. Pump the transfer lid airlock for 35-40 seconds to evacuate both the transfer lid airlock and the transfer arm, then close the transfer arm valve. Check that the transfer arm is in the 'locked' position.

15. Vent the transfer lid airlock, then release and lift the transfer arm from the transfer lid.

16. Attach the transfer arm to the microscope airlock and pump the airlock by pressing the 'P' button. This will pump the airlock and move the stage to the loading position.

17. Wait for the airlock vacuum to reach an acceptable level–the 'OK' button will turn on and the quickloader valve will unlock (see Note 6). Listen for a click.

18. Open the microscope airlock gate valve, then open the transfer arm valve.

19. Unlock the transfer arm and insert it all the way to dock the shuttle into the stage. Release the shuttle grabber and retract the arm. Check that the shuttle is no longer attached to the arm. Lock the transfer arm.

20. Close the microscope gate valve to isolate the microscope chamber. Leave the transfer arm attached to the quickloader. The transfer arm valve may be left open.

21. Verify that the stage temperature is around -180 °C and that the chamber pressure is similar to the value before the transfer (within 2-3 $\times 10^{-7}$ mbar).

Sample Inspection and Milling Preparation

While milling, the user should periodically check the stage temperature and chamber pressure for appropriate values. If there is any large deviation, the user may need to respond rapidly to salvage the sample. The heat exchanger dewar will last about 8 hours after initial cooldown, depending on gas flow rate. If the instrument needs to be operated for longer, the dewar can be refilled by slightly propping the heat exchanger aside and using a funnel to pour liquid nitrogen into the tank.

See Tables 4.1 and 4.2 for FIB/SEM imaging and scanning conditions. The preset positions for mapping, sputtering, and GIS deposition should be determined beforehand (e.g. during initial system installation) and kept for all users.

1. Switch on the SEM and FIB beams. If the FIB was previously turned off, it may require 10-15 minutes to start up.

2. Set scan rotation to 180° for both SEM and FIB. (see Note 7).

3. On the SEM view, change to the lowest magnification and find the grids to ensure that they are present. Check that the grids are seated appropriately in the shuttle.

4. Set the working distance: Start live SEM imaging and roughly focus the sample. Increase magnification to 5000x and refine focus and astigmatism. While actively imaging at focus, click 'Link Stage to Z' to set the working distance in the microscope coordinate frame.

5. Move the stage to the 'Mapping Position' for one of the grids—at 45° tilt at about 7.5 mm working distance. This will place the sample perpendicular with respect to the SEM column.

6. Acquire and save an SEM 'Photo' preset image at a low enough magnification (80x) to see the majority of the grid. Evaluate the grid quality and pick out appropriate target cells or squares for lamella milling (see Section 4.3.1, Fig. 4.5, and Note 8).

7. If the samples are good, discard the nitrogen from the loading station and let the station dry. Otherwise, you may unload the shuttle and load new specimens.

8. Move the stage to the sputtering position and activate the platinum sputtering feature. (see Note 9). When finished, click 'Recover from Sputtering' to return to the mapping position.

9. Move the stage to the platinum deposition position (GIS position), insert the GIS needle, and deposit the organo-platinum compound for a pre-determined amount of time (typically 5-10 seconds, see Note 10). When finished, ensure the GIS needle is retracted and return to the mapping position.

Lamella Milling

Lamella milling can broadly be divided into three phases: initial rough milling, thinning to about 400 nm thickness, and final milling to target thickness (Fig. 4.6).

In the rough milling phase, the goal is to develop a lamella that has been completely cleared of material throughout its length by the bottom and top milling patterns, respectively. We commonly refer to this as the lamella "breaking through" and is characterized by the appearance of empty space bordering the front and back of the lamella. This step is crucial because the lamellae may otherwise be obscured at high tilts in the TEM. Additionally, if the lamella has not broken through, the sample is likely too thick. A recent report has demonstrated that milling "expansion joints" adjacent to the lamella improves milling stability and quality [117]. In our hands, the use of expansion joints has increased overall lamella quality and is now a routine part of our cryo-FIB-ET workflow.

In the thinning phase, the goal is to gradually mill the lamella without introducing curtaining artifacts (see Section 4.3.4). Before reducing the milling pattern gap, each step should be allowed to continue until no biological material appears in the FIB milling pattern with increased software contrast. Additionally, the lamella surface should be monitored at regular intervals using the SEM to check for even texture.

In the final milling phase, the FIB current should be reduced to 30 pA or 10 pA. The milling patterns should be gradually moved closer to reach the target thickness. The lamella should be monitored more frequently by SEM to check that milling is proceeding evenly and that the GIS platinum layer is still sufficient to protect the leading edge of the lamella. The SEM can also be used to estimate lamella thickness by comparing the relative transparency of the lamella at 5 kV and 3 kV [88]. During this phase, the user should monitor the FIB milling pattern for any image drift and compensate accordingly with the X/Y shift knobs. Continue milling until the lamella is judged to be thin enough (see Note 11). Sometimes, the lamella will not be able to survive continued milling at which point milling should be stopped (e.g. lamella bending/bulging, loss of GIS platinum layer, or holes in the lamella from uneven milling).

1. Bring a selected milling target to the beam-coincidence point (see Note 12). Make sure sample is at desired tilt (see Section 4.1.2 and Section 4.3.1) to determine appropriate milling angle).

2. Import the saved milling pattern into the FIB view (see Table 4.3 for typical parameters). Adjust the milling position to create a lamella through the desired target. If needed, change the dimensions and gap between the milling patterns.

3. Change the FIB current to the desired beam current (Table 4.4).

4. After changing to a new FIB current, you may need to run the auto contrast routine for the FIB view. Additionally, take several brief FIB images to allow any image/beam drift to settle and to focus at the lamella position (See Note 13).

5. Start rastering the patterns. Monitor the milling progress regularly with the FIB and SEM. If desired, you may save SEM snapshots of intermediate milling steps to judge progress.

6. When milling at this current is finished, switch to a lower current, reduce the milling pattern separation, and adjust the pattern dimensions. (see Table 4.4 and Fig. 4.6)

7. Continue milling while reducing pattern separation and FIB current until you reach a pattern separation of $\sim$200nm. (see Note 14 and Table 4.4)

8. On some specimens, it may be necessary to perform a final milling step with a stage tilt of $\pm 0.5°$ from the desired angle to compensate for the slightly diverging FIB beam (Fig. 4.6 'Final Mill'). In this case, only enable milling on the side corresponding to the tilt direction (i.e. only enable the top pattern if milling with a $+0.5°$ tilt. See Note 15) [88].

9. Continue on to other lamella locations as desired.

Sample Retrieval

About 1 hour before retrieval, begin purging the loading station with dry nitrogen gas. If the loading station is at liquid nitrogen temperatures, increase the purge time to 2 hours. The sequence of events for sample retrieval is essentially the reverse of sample loading, but it is reproduced here for the sake of completeness.

1. After completing all lamellae, perform a final cleaning step to remove amorphous ice buildup (see Note 16). When finished, close the SEM and FIB column valves.

2. Make sure the shuttle holder in the loading station is in the vertical position.

3. Stop purging the loading station and fill with liquid nitrogen. Allow to cool until the liquid is no longer boiling. Refill as needed. Place the transfer lid on the loading station.

4. Open the transfer arm valve, then press the 'P' button to pump the airlock and move the stage to the loading position.

5. Wait for the airlock gate valve to unlock. Open the airlock gate valve.

6. Insert the transfer arm fully and close the grabber. Test the hold by pulling back slightly.

7. Fully retract the transfer arm and lock the arm in place. **Close the transfer arm valve and the airlock gate valve.**

8. Press ‘V’ to vent the quickloader airlock. Retrieve the transfer arm and place it onto the transfer lid.

9. Pump the transfer lid airlock for 35-40 seconds (make sure transfer lid sliding valve is closed), then open the transfer arm valve. **The next three steps should be done quickly in succession to minimize contamination.**

10. Open the transfer arm valve, then vent the transfer lid airlock for 3 seconds. Stop venting.

11. Unlock the transfer arm.

12. Open the transfer lid slider and quickly and gently insert the transfer arm to dock the shuttle into the loading station.

13. Release the shuttle grabber and retract the arm. If desired, pump down the transfer arm as described above.

14. Remove the transfer lid from the loading station and replace with the standard lid.

15. Using pre-cooled tools, flip the shuttle into the horizontal loading position, turn the locking screw to release the grids, then transfer the grids to a pre-cooled, labeled grid box.

16. Store the grid boxes with your specimens in liquid nitrogen.

End of Session Tasks

1. Remove heat exchanger from dewar and allow the stage and shield to warm to room temperature. (30-60 minutes)

2. Home the stage for the next user.

3. If the microscope will not be used in the next day, sleep the system to conserve gallium. Otherwise, keep it on but ensure the SEM and FIB column valves are closed.

4. Turn off hot plates and store tools.

5. When the stage and shield are near room temperature, turn the flow rates to 1 L/min to prevent moisture accumulation inside the heat exchanger gas lines.

4.3.3 Considerations for TEM

The specimen should be loaded such that the FIB milling axis is perpendicular to the TEM tilt axis (Fig. 4.7). This will allow maximum tilt range for tomography without the unmilled material blocking the field of view at high tilts. Due to FIB milling geometry, the lamella will have a measurable pre-tilt at the TEM ranging from 5° to 15° difference compared to reported stage goniometer angle. This pre-tilt will influence the tilt series acquisition scheme because in one tilt direction the specimen will appear to be much thicker at high tilt angles compared to the other direction. (See Section 4.1.2) Additionally, sample orientation is important for accurate focus and tracking when acquiring data with low-dose techniques. TEM data acquisition is mostly handled through automated routines from software packages such as SeriaEM [35, 34].

When beginning a new project, it will be necessary to iteratively optimize samples between the TEM and FIB. For example, the final lamella thickness should be guided by the intended TEM data acquisition pixel size. This is important in order to limit the total dose applied to a specimen during tilt series acquisition. Doubling the TEM magnification while maintaining a similar beam intensity on the camera will result in four times the applied dose (in electrons per square angstrom) to the sample. A higher desired TEM magnification will therefore require thinner lamellae in order reduce the dose applied to the specimen while maintaining an appropriate beam intensity on the camera. Conversely, thick specimens will require additional radiation, resulting in lower signal-to-noise ratio and lower resolution, but allow imaging of a larger volume for increased cellular context.

For reasons described above, it is important to track and orient grids during FIB milling and through to TEM data acquisition. This is most easily accomplished by using marked autogrid supports that allow the user to orient the sample at the aquilos loading station and at the TEM loading station. Examples of marked autogrids include the commercially available cryo-FIB-

autogrids that have laser etched dots in the surface of the ring to indicate sample orientation. These marks may be difficult to see under liquid nitrogen, so we routinely mark the autogrids with a colored permanent marker.

While cryo-FIB milling exhibits fewer artifacts compared to sections from microtomy, the ion beam will damage the surface of the lamella as it ablates material [118]. Additionally, repeated use of the SEM for monitoring milling progress also contributes electron damage. In particular, sensitive structures such as bacterial polyphosphate bodies, accumulated damage from the FIB/SEM can be seen as localized bubbling confined to the surface of the specimen to several nanometers deep. However, previous work has demonstrated that FIB milled samples do not exhibit heat-induced devitrification beyond the immediate interacting surface [118].

4.3.4 Common Troubleshooting Items

System Maintenance

In addition to manufacturer suggested regular instrument upkeep, we recommend following a regular maintenance schedule for cryo-FIB/SEM systems focused on checking stage temperature, cleaning the stage of platinum buildup, and cleaning seals/o-rings of dust. These tasks should be done every 3-4 months. Additionally, the stage components should be inspected for wear and defects regularly due to the large temperature cycles that these parts experience.

System consumables include the gallium liquid-metal ion-source and the FIB aperture strip, both of which may need replacing every six months if the instrument is used routinely.

Equipment Troubleshooting

Poor chamber vacuum.

The system should reach better than 2×10^{-6} mbar at room temperature and better than 7×10^{-7} mbar at cryogenic temperatures. If these are not satisfied, the chamber seals especially those on the front door and the quickloader should be inspected and cleaned. Poor vacuum may lead to an increased rate of water vapor accumulation on the sample resulting in an increase in the lamella thickness that reduces imaging quality.

Frost on heat exchanger tubing.

Frost buildup on the heat exchanger tubing is due to loss of vacuum insulation. The typical causes are pump failure, a leak in the outer tubing, or a leak in the internal nitrogen lines. Continued use of the system with frost buildup may lead to poor stage cooling

Amorphous ice contamination.

From our experience, poor stage cooling will lead to accumulation of amorphous ice or even "leopard skin" ice when observed at the TEM. The temperature of the top of the stage (where the shuttle is inserted) should be measured using a thermocouple. Starting from room temperature, the stage top should be able to reach below -170 °C within 30 minutes. If this is not the case, the stage should be disassembled and thoroughly cleaned. We have found that buildup from the sputter coater and GIS can be responsible for stage temperature issues.

Crystalline/Atmospheric ice contamination.

Check that the o-rings on the transfer arm and transfer lid are clean and in good condition. Ensure that all tools and loading equipment are dry before handling samples. Ensure that the venting line on the transfer lid has been purged for at least 10 minutes, and keep purging continuously for the duration of the session. Ensure that any liquid nitrogen having direct contact with samples is free of frost.

Inaccurate ion beam currents.

When the beam is blanked, the FIB is deflected into a faraday cup to measure the beam current. If the reported value is much higher (10-15%) than the nominal value, the ion beam aperture strip is likely worn out (Fig. 4.8). Typical FIB milling may use one particular aperture (eg 10 or 30 pA) much more than the others, which may cause them to wear out earlier and become much larger than the initial size. This leads to drastically increased ion beam currents and poor control over milling. On certain microscopes, it may be necessary to switch to an unused "parking position" FIB aperture when the microscope is idle but the ion source is left on, due to the continual exposure of the aperture strip to the ion beam.

Sample Troubleshooting

FIB image instability.

The image may appear to drift or distort in the FIB view, especially at high beam currents or magnifications. Check that there are no ice or autogrid obstructions near the field of view that may be deflecting the ion beam. Check that the FIB accelerating voltage is at 30 kV. Increasing platinum sputtering time may help with drift.

Lamella appears skewed relative to milling axis.

The grid surface in the FIB view is not perfectly flat. Use additional scan rotation to make the FIB image appear horizontal. (see Note 7 and Fig. 4.9)

Curtaining artifacts.

These artifacts manifest as ridges and grooves on the surface of the lamella parallel to the milling axis. The FIB current is too high for the lamella thickness or milling has not completed before narrowing the patterns. Reduce the current and extend the milling time to ensure a flat lamella surface. Monitor the quality of the lamella at regular intervals with the SEM. If the GIS platinum layer is wearing away too quickly, the initial deposition time may be increased.

For tall cells, the profile is presented such that the cell surface is nearly perpendicular to the beam. This is not the case for flat cells or bacteria, where the surface is much more oblique (compare Fig 4.5H and 4.5I). The tall profile can lead to issues with insufficient GIS platinum deposition that would otherwise be acceptable. These cells may require a longer GIS platinum deposition time and rotating the stage to optimize deposition thickness.

Broken lamellae at the TEM.

The finished lamellae are relatively fragile and are susceptible to damage from rough handling. Slightly increasing the GIS platinum deposition time may proved extra support and make handling easier. It is important to only handle lamellae grids by the very edge of the autogrid support. Another option is to reduce the width of the lamellae to make them less susceptible to breakage.

Lamella appears to bend during milling.

Recent reports have suggested that lamella bending can be attributed to tension in the bulk material arising from the vitrification process. The proposed solution is to mill additional "micro-expansion joints" near the lamella to reduce the impact of surrounding material motion [117]. In our hands, the micro-expansion joints also reduce bending and subsequent breaking at the TEM. Silicon dioxide grids may also offer a stiffer support that may reduce lamella bending or breaking [119].

4.4 Notes

1. Because the grid is held at 45° and the FIB column angle relative to the SEM column is 52°, there is a 7° difference between the reported stage angle and the incident milling angle. To estimate the incident milling angle, subtract 7° from the reported stage angle.

2. The EM grid should be chosen such that each grid square is large enough to contain the widest desired lamella, but small enough to have sufficient sample rigidity so that the lamella will not bend and break during subsequent handling. We routinely use 200 mesh quantifoil grids for FIB milling. The specific pattern of holes will determine blotting speed and sample dryness. We are routinely using R1/4 grids for mammalian cells and R2/1 grids for bacteria. Grid material should be: gold for cells cultured directly on the grid, copper for cells deposited immediately before plunge freezing. See section 4.3.1 for sample type considerations.

3. The autogrid is a rigid ring support in which TEM grids are placed and secured with a spring clip. This arrangement allows improved handling and stability of samples. Grids may be clipped either using the provided loading station, or in any other suitable device that will minimize atmospheric contamination. Grids should be clipped so that the cell side is facing towards the flat side of the autogrid. We have found clipping grids under a very low level of nitrogen to be most efficient, with minimal grid square breakage. Once

clipped, the grid is permanently mounted in the autogrid and is essentially impossible to remove at cryogenic temperatures without damaging the grid.

4. On our system, the chamber base pressure at room temperature is typically 2×10^{-6} mbar or better. If the base pressure is too high, the chamber seals, airlock seals, and nitrogen lines should be cleaned and inspected (See Section 4.3.4).

5. The reported stage temperature is measured from the lower stage, which is quickly cooled by cold nitrogen gas. However, the upper stage (where the sample sits) usually lags behind due to its thermal mass and reduced contact area with the lower stage. Waiting at least 30 minutes after full cooldown is important to ensure that the upper stage is well below devitrification temperature.

6. The microscope quickloader gate valve is kept locked to prevent accidental opening and venting of the chamber. The valve will only unlock if the user has issued the 'pump' command through the button interface **AND** if the pressure in the quickloader airlock is low enough. Additionally, the gate valve is only unlocked for about 90 seconds before the action times out and relocks. The valve must be opened within this timeframe. When closing the valve, wait for it to lock before reopening or re-issuing the pump command. Otherwise, we have found that this may lead to the gate valve being stuck in the open state.

7. Setting the scan rotation to 180° is optional, but it orients the SEM and FIB views to appear more natural such that the FIB view shows cells "sitting" on the grid, rather than "hanging" from the grid. In some cases, the scan rotation of the FIB column is not perfectly parallel to the grid surface. In this case, the resulting lamellae will be tilted relative to the milling axis (Fig. 4.9A-D). Such tilted lamellae become more difficult for tomography due to limited focus and tracking area (see 4.3.3). This issue can be corrected by rotating the scan direction of the FIB column until the grid surface appears horizontal (Fig. 4.9E-H).

8. In addition to sample specific considerations for milling, users should consider the accessible area of the grid at the TEM for tilt series acquisition. This depends on the specific TEM instrument, but is typically limited to the grid squares that are in the center 1 mm of the grid. For a 200 mesh grid, this is about 10-by-10 grid squares centered over the grid. Lamellae should be milled within this region. To minimize occlusion from the grid bars at high tilt at the TEM, it is generally best to make lamellae that are centered in the grid square.

9. Sputter coating is used to improve the image quality of non-conductive samples by depositing a layer of metal to allow charge to quickly dissipate. The Aquilos has a built-in sputter coater. Set the number of purge cycles to 0 (which would otherwise lead to sample contamination) and click 'Prepare for Sputtering'. The microscope will enter a low vacuum state (about 0.1 mbar) by partially venting with dry argon, and the stage temperature will increase slightly to about -170 °C. The stage will move to the sputtering position. When the preparation actions have finished, select the sputtering parameters or the preset values and run the process. Typical sputter conditions for initial rough sputtering are 1 kV, 30 mA, for 15 seconds at 0.10 mbar chamber pressure. You can see the plasma glow using the chamber camera. When sputtering is complete, click 'Recover from Sputtering' to return the stage to the mapping position and return to high vacuum

10. The GIS deposition time depends on the sample type, the intended deposition thickness, and the preset deposition stage coordinate. If the stage is closer to the tip of the GIS needle, a shorter deposition time will yield the same thickness of GIS platinum as a longer deposition time at a further distance. The deposition stage position/coordinates can be adjusted to allow long/short deposition times, or can be adjusted to be centered between the two grids such that both the left and right grids are coated at the same time.

11. We have found that judging appropriate lamella thickness and when to stop milling requires some experience and iterative comparison between the SEM and TEM to 'calibrate' the

user. One helpful exercise is to make a lamella, estimate its thickness at the SEM, then measure the actual thickness from a tomogram.

12. To manually find the beam coincidence point, tilt to the desired milling angle and go to a low mag view for both SEM and FIB. Find your target in both SEM and FIB, and center the target in the FIB view using XY moves. Switch to SEM view and move the stage in Z so that the target is about halfway closer to the center of the SEM field of view. (e.g. if the target was 100 um away from the center of the SEM, move the stage in Z so that the target is now about 50 um away.) Switch to the FIB view and recenter the target using XY moves. Switch to SEM and check positioning. Reiterate between XY moves in FIB view and Z moves in SEM view until the target is centered in both SEM and FIB. Alternatively, the proprietary MAPS software package from TFS allows correlation between fluorescent, SEM, and TEM images. Additionally, MAPS may be used as a microscope control program. This software package has the ability to calculate eucentric height for a given point on a sample, which should be very close to the beam-coincidence point. To do so, add a lamella object, then go to its mapping position. Select 'Calculate Eucentric Height' which will ask you to keep the object centered at several tilts. The specific internal calibration for accurate eucentricity should be determined during software installation and kept for all users.

13. This apparent drift is not due to physical specimen movement, but due to slight movement in the beam due to sample interaction. Especially at high FIB currents, the sample may acquire charging that influences the FIB [120].

14. Step milling improves lamella stability by forming a gradual transition from the unmilled material to the lamella. Without step milling, the lamellae are more prone to developing cracks at the edge where they connect to the bulk material.

15. The FIB view has a shallow depth of field, which can be observed when the the front of

the lamella is in sharp focus, but the back of the lamella is out of focus. This leads to heterogeneity in milling efficiency over the surface of the lamella. At the TEM, this can be observed where the back of the lamella is thicker than the front. To thin only the back portion of the lamella, the stage should be tilted approximately +0.5° which will expose the back for milling without disturbing the front edge of the lamella [88].

16. Given the large chamber volume, poor vacuum compared to the TEM, and cryogenic temperatures, amorphous ice buildup is inevitable inside the cryo-FIB/SEM. This can be minimized with proper instrument maintenance, but in our experience, long operating times of more than 6 to 8 hours lead to ice buildup from the chamber and from milling redeposition. Before sample retrieval, it is recommended to perform a short five minute lamella cleaning step with a low FIB current for all lamellae immediately prior to sample retrieval (Fig. 4.6). This step is essentially identical to the fine milling step, but with the pattern set to skim over the surface of the lamella without removing too much material.

4.5 Acknowledgements

We would like to acknowledge the following people: Reika Watanabe and Miles Paszek for providing images of NIH3T3 and yeast grids, respectively. Reika Watanabe, Kanika Khanna, and Sergey Suslov for fruitful discussion of FIB/SEM. Mario Aguilera for photography of microscope equipment.

This work was supported by an NIH Director's New Innovator Award 1DP2GM123494-01 (to E.V.) and NIH 5T32GM7240-40 (to V.L.). Images of cyanobacteria are from projects supported by NIH R35GM118290 awarded to Susan S. Golden. This work was performed in part at the San Diego Nanotechnology Infrastructure (SDNI) of UCSD, a member of the National Nanotechnology Coordinated Infrastructure, which is supported by the National Science Foundation (Grant ECCS-1542148).

Chapter 4 is a reprint of material published as Vinson Lam and Elizabeth Villa "Practical Approaches for Cryo-FIB Milling and Applications for Cellular Cryo-Electron Tomography", Methods in Molecular Biology, vol.2215, 2021. The dissertation author was the primary investigator and author of this paper.

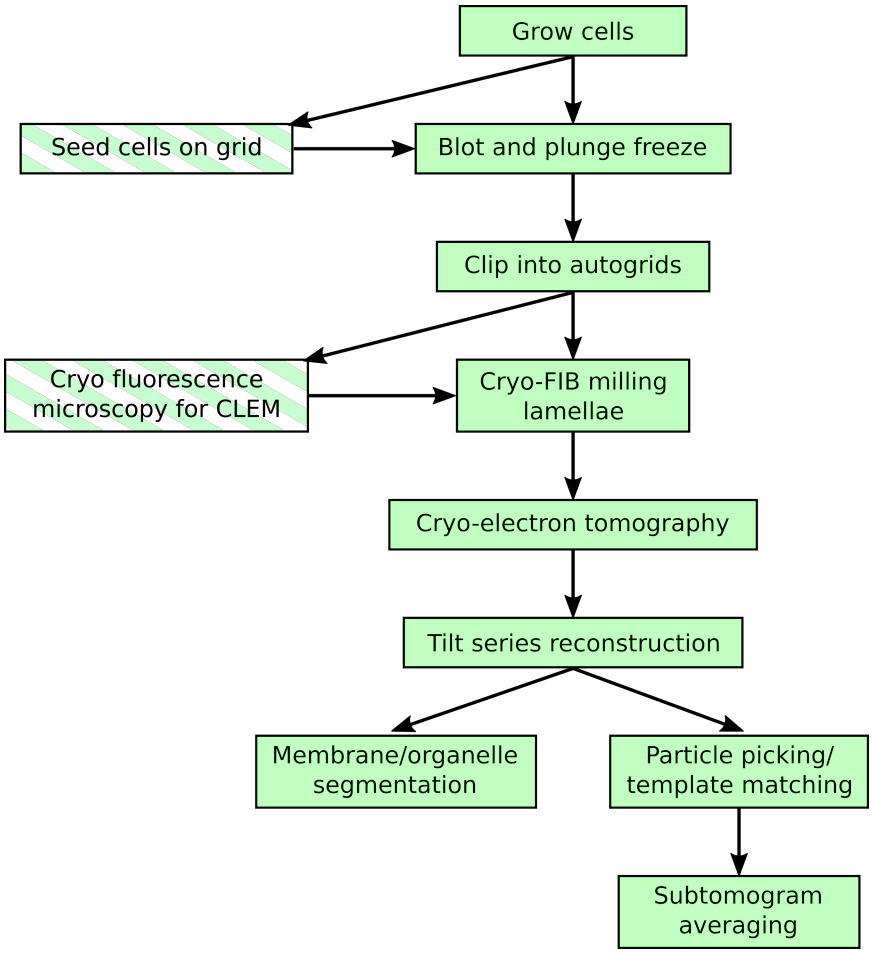

Figure 4.1. Typical cryo-FIB-ET workflow.

Cryo-FIB-ET is a vertically oriented workflow in which the same sample is processed throughout. This technique is sensitive to the success rate of each step and is limited by low throughput during lamella milling. This chapter seeks to provide practical guidance on increasing success at cryo-FIB milling, thereby increasing throughput for cryo-ET. Typical workflow steps are highlighted with a solid background. Optional steps are highlighted with a striped background.

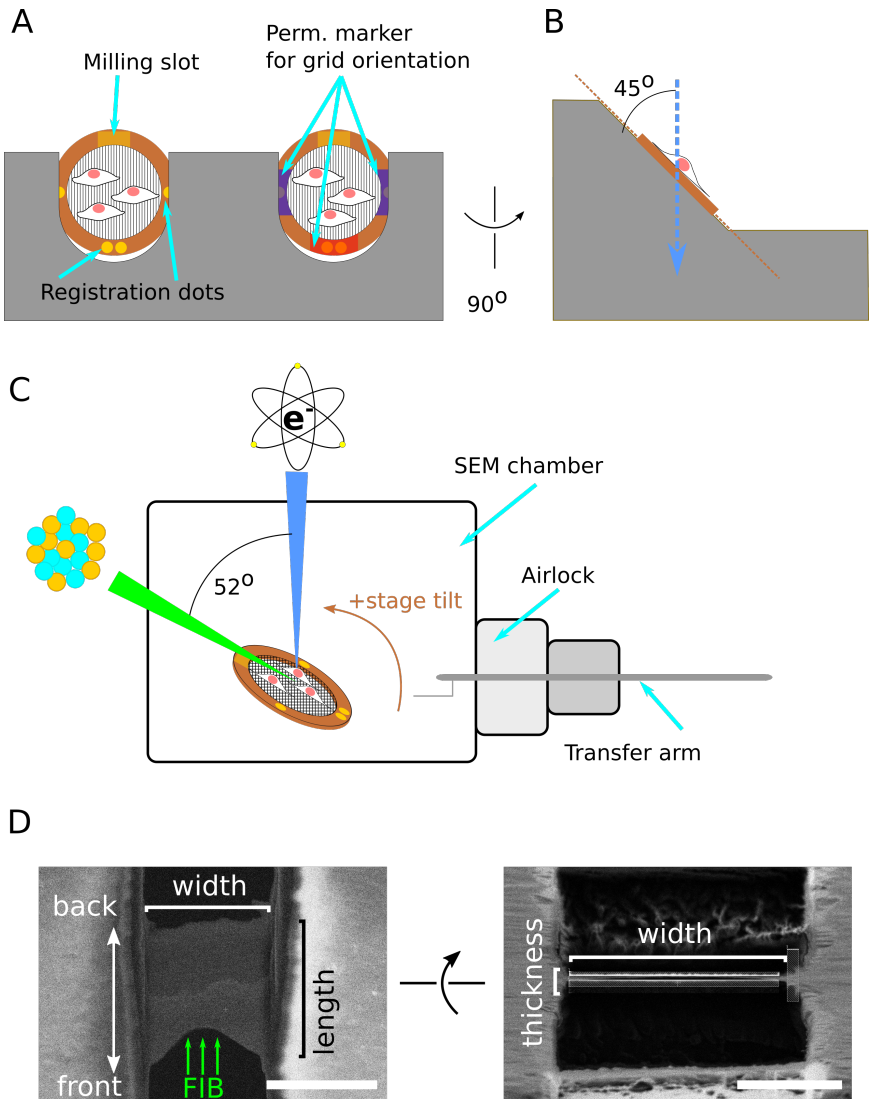

Figure 4.2. Schematic of grid and FIB/SEM geometry.

(A) Schematic of two grids clipped into an cryo-FIB-autogrid support and loaded into the shuttle, with cells on the top surface. The cryo-FIB-autogrid has a milling slot that enables lower angle milling and registration dots for aligning the grid when loading at the SEM or TEM. Additional markings with permanent marker can be made to enhance visibility under liquid nitrogen. Compare to Fig. 4.3E. (B) Side view of grid loaded into shuttle, illustrating the grids are held at a 45° angle relative to vertical. (C) Schematic of relative orientation of the SEM column, FIB column, sample stage, and transfer arm. The grid is positioned at the beam-coincident point, and the milling slot is oriented toward the FIB column. The stage is arranged to have positive tilt towards the FIB column. This results in FIB-sample incident angle 7° smaller than the reported stage angle. SEM beam is indicated in blue, FIB in green, and the specimen in copper. (D) Schematic of terminology used in this chapter to refer to lamella dimensions and orientation. *Scale bars: 5 μm*

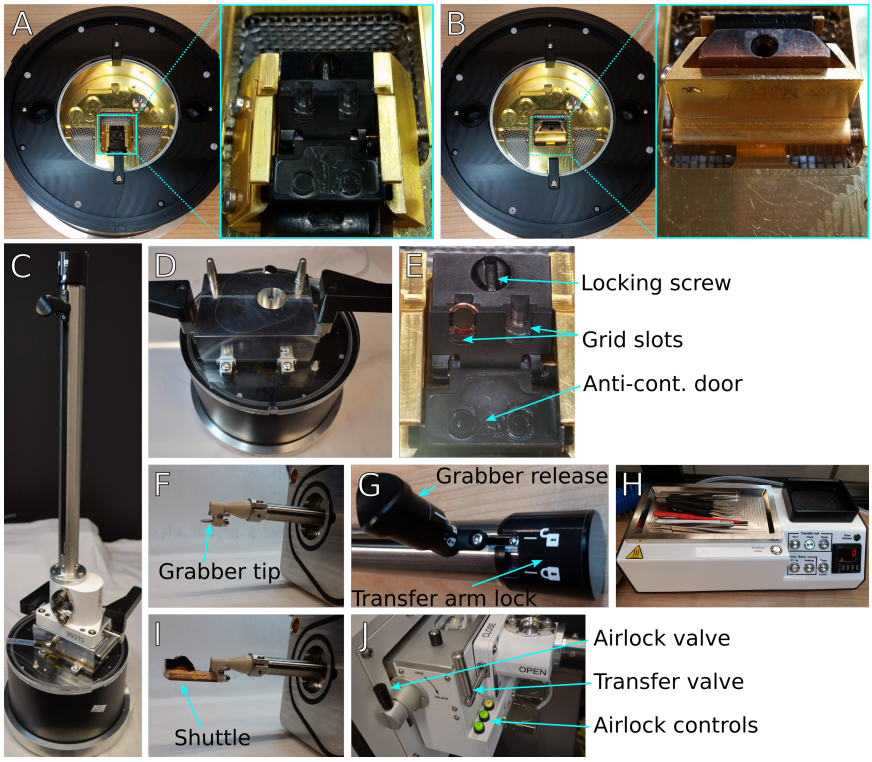

Figure 4.3. Equipment for FIB/SEM sample preparation and loading.

(A) Loading station with shuttle inserted and in the loading position. Inset shows detailed view of shuttle position. (B) Same as (A) but with the shuttle rotated vertically into the transfer position. Inset shows detailed view of shuttle in vertical transfer position. (C) Transfer arm attached to the transfer lid and positioned over the loading station. (D) Loading station with transfer lid, showing the transfer lid airlock chamber and the registration pins to place the transfer arm. (E) Detail of shuttle showing a loaded grid in the appropriate location and orientation, the locking screw to secure grids, and the anti-contamination door that covers the grids during transfer steps. Users should take care to keep the milling slot unmarked due to potential interactions with FIB imaging. (F) Detail of the transfer arm grabber tip, showing the registration pin and the grabber locking mechanism. (I) Detail of shuttle and grabber together. (G) Detail of transfer arm locking mechanism. The transfer arm lock on the right releases the rod to insert or retract. The smaller grabber release knob on the left opens and closes the grabber. (H) Preparation controller with tools: fine handling tweezers, grid box opening tool, screwdriver. The preparation controller is used to pump or vent the transfer lid and transfer arm assembly when moving specimens to and from the microscope. (J) transfer arm attached to airlock of FIB/SEM quickloader system. The transfer and airlock valves control access to the transfer arm chamber and the microscope chamber, respectively. Airlock pumping and venting actions are controlled by the green ‘P’ and ‘V’ buttons, respectively.

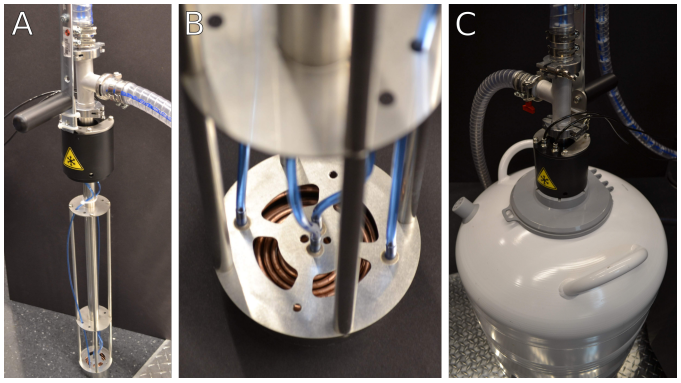

Figure 4.4. Heat exchanger assembly.

(A) Heat exchanger in a stand when not in use. During cryogenic operation, the heat exchanger assembly is immersed into a liquid nitrogen dewar. The heat exchanger assembly is kept under partial vacuum through the clear tubing attached near the top to maintain thermal isolation of cold gas nitrogen. (B) Detail of heat exchanger coils and nitrogen gas lines. Warm nitrogen gas is passed from the blue gas lines into the copper coils and cooled to liquid nitrogen temperatures. Cold gas is routed through the body of the heat exchanger into the microscope stage. (C) Image of heat exchanger assembly inserted into a liquid nitrogen container during cryogenic operation. The thick clear tubing near the top of the heat exchanger unit is part of the vacuum isolation system.

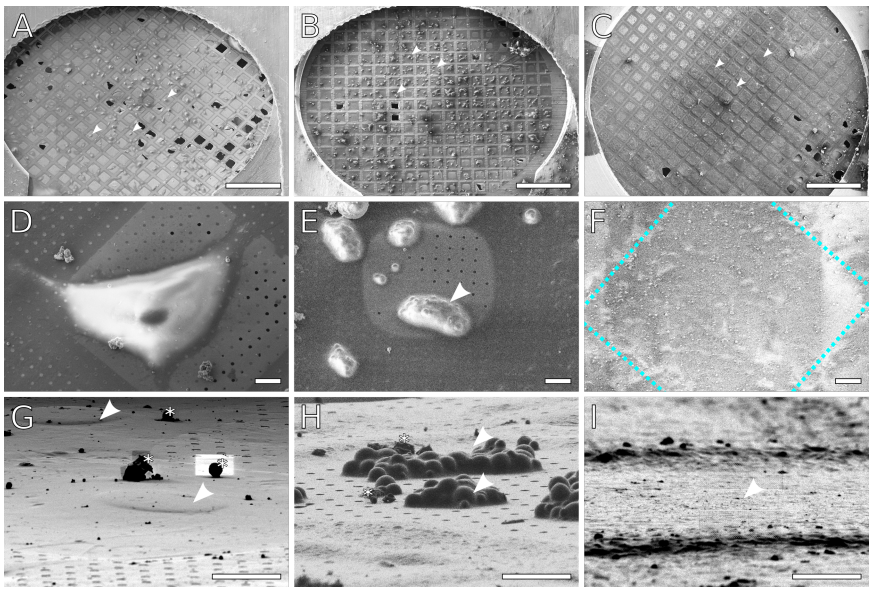

Figure 4.5. Examples of ideal specimen concentrations.

SEM images of (A) Adherent mammalian cells (NIH 3T3) grown on a grid. The cells density is low enough that there are only 1-2 cells per grid square. The surface is sufficiently blotted to reveal the carbon film, while enough liquid remains to cover the cells (some holes remain hydrated). (B) Yeast cells deposited on a grid. The cells form clumps consisting of several cells, with no more than 1-2 large clumps per grid square. As with (A), the surface is blotted to reveal the carbon film, while enough liquid remains to cover each clump. (C) Planktonic bacterial cells deposited on a grid. A monolayer of cells covers each grid square. Enough liquid has been removed to expose the grid bars, but the carbon film is not visible due to coverage by cells and media. Arrow heads indicate examples of cells/grid squares suitable for lamellae milling. (D,E,F) Close up views of individual cells/grid squares for (A,B,C) respectively. In (F), the cells are obscured by the GIS platinum layer. The approximate location of the grid bars is outlined in blue.(G,H,I) Representative FIB views of individual targets for lamella milling, all imaged at 13° stage tilt. Asterisks mark out atmospheric ice contamination. (G) NIH 3T3 cells. Nuclei are indicated by arrowheads. (H) Clumps of yeast, indicated by arrowheads. Notice that yeast clumps have a much taller profile compared to the 3T3 cells or the bacteria. (I) Monolayer of bacteria in a grid square. The darker horizontal ridges are the grid bars. Individual bacteria are not visible as they are embedded in an ice layer and overlaid with platinum from the GIS coating. *Scale bars: A-C 500 µm; D-I 10 µm.*

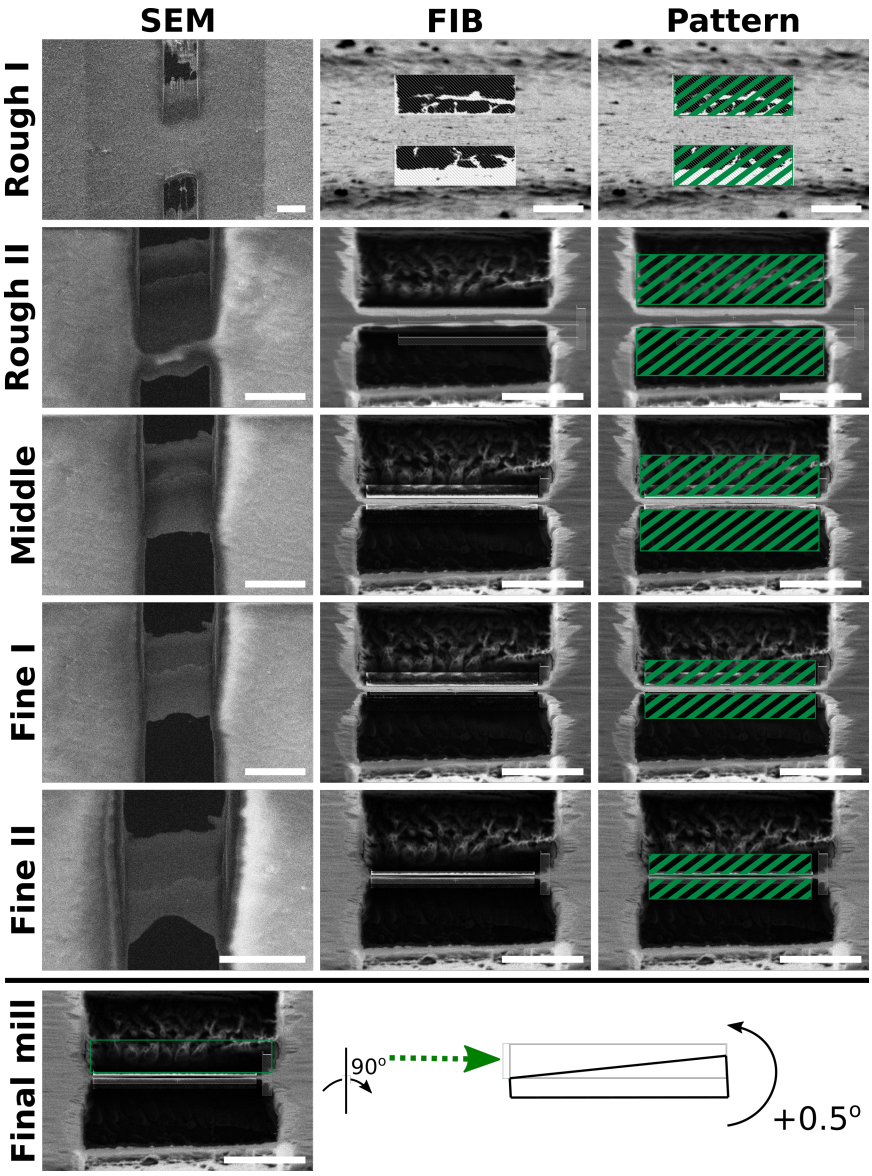

Figure 4.6. Overview of typical FIB milling progression.

SEM (left column) and FIB (middle column) views of one lamella milled from beginning to end. As material is removed, the lamella becomes more uniform and electron transparent seen from the SEM view. Additionally, the leading edge of the lamella becomes thinner seen from the FIB view. Third column: Schematic of milling patterns overlaid onto lamella FIB views (Table 4.4). Bottom row: schematic of final milling step with a +0.5° stage tilt to make lamellae of uniform thickness using only the top milling pattern and an additional +0.5° stage tilt. Green arrow represents the direction of the ion-beam milling. For the final step, only the top pattern is activated to selectively mill the thicker portion in the back. The milled area is indicated in grey. *Scale bars: SEM images 10 µm; FIB images 5 µm.*

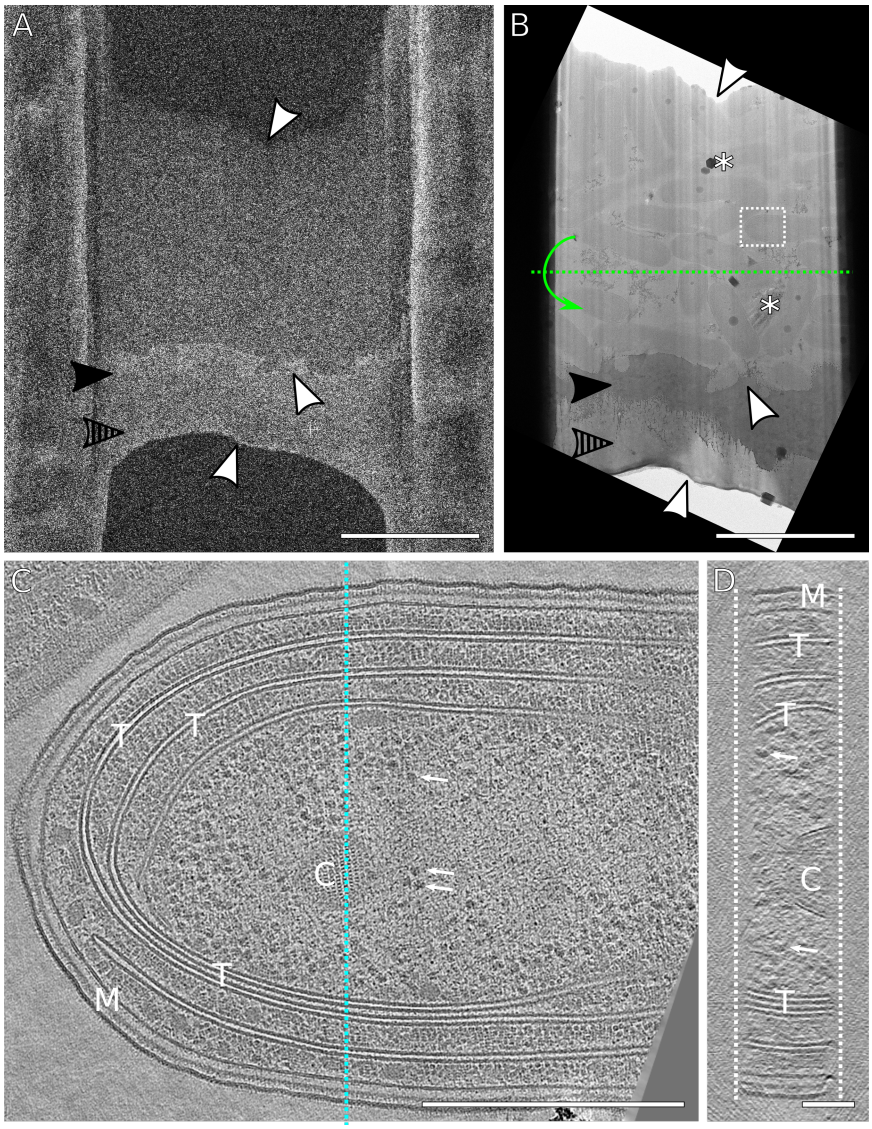

Figure 4.7. Representative lamella and reconstructed tomogram.

(A) SEM image of a finished lamella through a lawn of cyanobacteria. The milling direction was from bottom to top. The lamella was milled with expansion joints to reduce buckling (not visible here) [117]. (B) Corresponding TEM image of (A) showing a field of bacteria. White arrowheads mark areas of correlation between the SEM and TEM image. The solid and striped arrowheads point out the platinum sputtering and GIS platinum layers, respectively. Asterisks mark areas of atmospheric ice contamination and poor vitrification. The white box indicates the field of view for tilt-series acquisition. Green dotted line represents the TEM tilt axis. (C) XY view of a reconstructed tomogram of a single cyanobacterium from the lamella. M: inner/outer membrane. T: thylakoid membranes. C: carboxysomes. Arrows: ribosomes. (D) YZ view of reconstructed tomogram corresponding to the slice indicated by the blue line in (C) with structures labeled identically. The lamella thickness is approximately 150 nm. The surfaces of lamella are indicated by the dashed white lines. *Scale bars: A,B 5 µm; C, 500 nm; D, 100 nm*

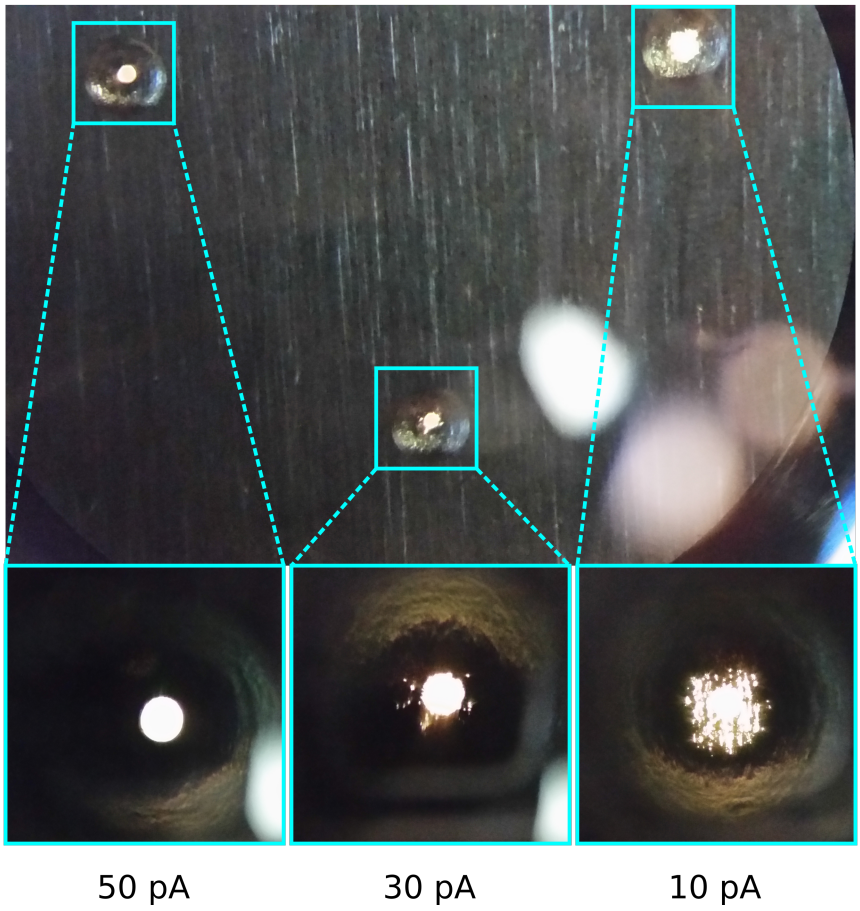

Figure 4.8. FIB aperture wear.

Basic light microscope image of a FIB aperture strip retrieved after about 6 months of 4 sessions/week use. The smallest apertures used for milling (10 and 30 pA) have suffered extensive damage to the edge of the aperture hole leading to high beam currents, compared to an infrequently used aperture (50 pA).

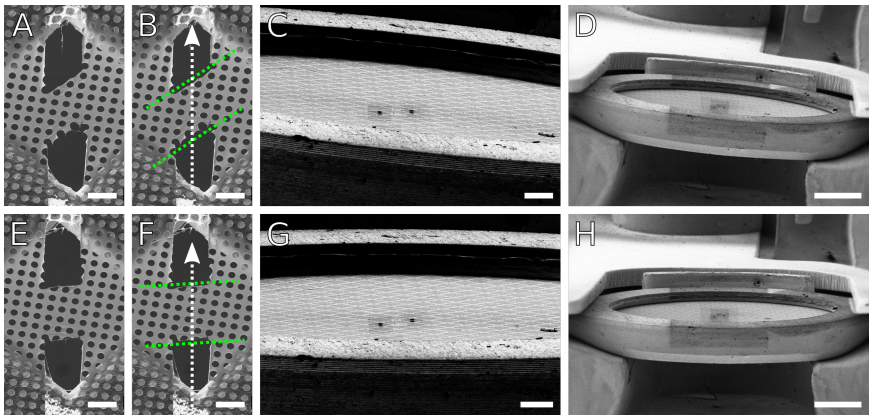

Figure 4.9. Correcting skewed FIB milling with scan rotation.

(A,B) SEM images of a skewed lamella made in carbon foil. Dotted green lines mark the approximate geometry of the lamella relative to the milling axis as indicated by the white arrow. (C,D) FIB views of the clipped grid at low magnifications, showing an apparent tilt of the grid relative to the horizontal. (G,H) By adjusting the apparent tilt using additional scan rotation applied to the FIB view, the lamella skew angle can be corrected (E,F) to become nearly perpendicular to the milling axis. These demonstrative lamellae were milled on a room temperature carbon film grid. Results are directly applicable for cryogenic samples. *Scale bars: A,B,E,F 10 µm; C,G 100 µm; D,H 500 µm.*

Table 4.1. Typical imaging conditions for SEM and FIB for frozen hydrated biological specimens.

	Voltage (kV)	**Current (pA)**	**Detector**	**Mode**
SEM	2-**5**	25	**ETD**	Secondary Electrons
FIB	30	1.5*; 10-500*	**ETD**	Secondary Electrons

*1.5 pA for live imaging. 10-500 pA for active milling.

Table 4.2. Typical scan settings for SEM and FIB views for frozen hydrated specimens.

	Live (FIB/SEM)	**Snapshot (SEM)**	**Photo (SEM)**
Dwell Time	200 ns	200 ns	2 μs
Line Integration	1	1	1
Resolution	1536 x 1024	3072 x 2048	6144 x 4096
Bit Depth	8	8	8-16

'Live scan' and 'snapshot' are used to monitor lamella milling. The 'photo' preset is typically used to generate a low magnification grid overview due to the high electron dose. Snapshots and photos are not used in FIB view due to the potential for beam damage.

Table 4.3. Milling pattern parameters.

Milling Pattern Basic Properties	
Application	Si
X Size	12-10 μm
Y Size	*
Z Size	$\sim$10 μm
Scan Direction	**Outside to inside
Dwell Time	1 μs
Beam	Ion

*The Y size for both patterns should be adjusted throughout milling to become smaller, just enough to encompass the remaining unmilled material. **The scan direction for each pattern (ie. top-to-bottom or bottom-to-top) should be set so that the milling direction is towards the lamella. For very sensitive samples, the dwell time may be reduced.

Table 4.4. A typical scheme for performing step-wise milling starting from rough to final polish.

	Rough I	**Rough II**	**Middle**	**Fine I**	**Fine II**	**Final Polish**
FIB current	0.5 nA	0.3 nA	0.1 nA	30 pA	10 pA	10 pA
Pattern Separation	3 μm	1.5 μm	750 nm	400 nm	200 nm	*n/a
Pattern X size	12 μm	11.5 μm	11 μm	10.5 μm	10 μm	10 μm
Typical time	10 min	10 min	15 min	20 min	20 min	10 min

FIB current and pattern X size are gradually reduced as the lamella becomes thinner. Note that the pattern separation does not correspond exactly to lamella thickness due to FIB beam spread. At low currents, milling time increases but there is greater control over lamella quality. *For final polishing, the stage is tilted by an additional 0.5 degrees and only one pattern is used to mill.

Appendix A

Closing Statement

In 2017, a few months after I started my doctoral research to visualize cyanobacterial clock complexes in high resolution using CET, the Nobel Prizes in Physiology or Medicine and in Chemistry were respectively awarded to pioneering scientists in circadian biology and cryo-electron microscopy. At the time, my advisor Elizabeth quipped that Nobel Prizes are awarded when there are no major discoveries left in a field. This assessment leaves out that fact that scientific developments mature beyond the scope of the original research, often becoming widely used and cited in distant fields.

I started as a complete novice to CET and my experience learning to use this fickle technology was facilitated by more senior lab members. In turn, as I became more proficient, I found great joy and satisfaction in teaching new Villa Lab members to use our instruments and in improving our technological capabilities to automate data acquisition. I have likewise developed useful prototype instruments in the Golden Lab to address questions about cyanobacterial motility. These experiences in teaching and prototyping have informed my future career decisions to pursue a role as an imaging specialist at an EM facility. This role would enable biologists to use CET in their research and to focus on biological questions without needing to learn the minutiae of microscope operation. In an ideal future, CET would be routinely used in the biologist's toolkit much like PCR, another Nobel-winning technique.

As I allude to in the epigraph of this dissertation, microscopy in general and *cryo*-electron

microscopy especially, are only snapshots of a single moment in a cell's life. In the midst of the crowded cellular environment it is impossible to assign particle identities without error, nor is it possible to count them precisely. The most that we can do is to estimate using the best computational resources available. The real number of ribosomes in a cell is unknowable, but we can get close.

At first glance, it appears unusual that we would choose to study such a dynamic and *time-dependent* process as circadian biology using a static method such as CET. But the advantage is in being able to capture the cell in the course of its daily life, and preserving the information in perpetuity. Every tomogram of a cyanobacterium represents an immortal cell destined to live on *in silico* far longer than it would have ever lived *in vivo*. With our atlas, we have prepared a comprehensive foundation for the study of circadian cell biology in cyanobacteria for years to come.

Circadian biology has likewise grown beyond its original scope in fruit flies to encompass human health with implications for long-term health outcomes and drug treatment. Life on earth has evolved around daily fluctuations in light, temperature, and humidity because of Earth's rotation. The Sun is our oldest companion. I would like to close with a quote from another 2017 Nobel Laureate, Kazuo Ishiguro: "The Sun, noticing there were so many children in the one place, was pouring in his nourishment through the wide windows..." (Ishiguro, *Klara and the Sun*). All organisms on Earth are the Sun's children!

Bibliography

[1] Cohen SE and Golden SS (2015) Circadian rhythms in cyanobacteria. Microbiol Mol Rev 79(4):373–383

[2] Diamond S, Jun D, Rubin BE, and Golden SS (2015) The circadian oscillator in *Synechococcus elongatus* controls metabolite partitioning during diurnal growth. Proceedings of the National Academy of Sciences 112(15):E1916–E1925

[3] Taton A, Erikson C, Yang Y, Rubin BE, Rifkin SA, Golden JW, and Golden SS (2020) The circadian clock and darkness control natural competence in cyanobacteria. Nature Communications 11(1):1688

[4] Yang Q, Pando BF, Dong G, Golden SS, and van Oudenaarden A (2010) Circadian gating of the cell cycle revealed in single cyanobacterial cells. Science 327(5972):1522–1526

[5] Dong G, Yang Q, Wang Q, Kim YI, Wood TL, Osteryoung KW, van Oudenaarden A, and Golden SS (2010) Elevated atpase activity of kaic applies a circadian checkpoint on cell division in synechococcus elongatus. Cell 140(4):529–539

[6] Vijayan V, Zuzow R, and O'Shea EK (2009) Oscillations in supercoiling drive circadian gene expression in cyanobacteria. Proceedings of the National Academy of Sciences 106(52):22564–22568

[7] Liu Y, Tsinoremas NF, Johnson CH, Lebedeva NV, Golden SS, Ishiura M, and Kondo T (1995) Circadian orchestration of gene expression in cyanobacteria. Genes & Development 9(12):1469–1478

[8] Swan JA, Golden SS, LiWang A, and Partch CL (2018) Structure, function, and mechanism of the core circadian clock in cyanobacteria. Journal of Biological Chemistry 293(14):5026–5034

[9] Markson JS, Piechura JR, Puszynska AM, and O'Shea EK (2013) Circadian control of global gene expression by the cyanobacterial master regulator rpaa. Cell 155(6):1396–1408

[10] Katayama M, Tsinoremas NF, Kondo T, and Golden SS (1999) *cpmA*, a gene involved in an output pathway of the cyanobacterial circadian system. Journal of Bacteriology 181(11):3516–3524

[11] Woelfle MA and Johnson CH (2006) No promoter left behind: Global circadian gene expression in cyanobacteria. Journal of Biological Rhythms 21(6):419–431. PMID: 17107933

[12] Smith RM and Williams SB (2006) Circadian rhythms in gene transcription imparted by chromosome compaction in the cyanobacterium synechococcus elongatus. Proceedings of the National Academy of Sciences 103(22):8564–8569

[13] Woelfle MA, Xu Y, Qin X, and Johnson CH (2007) Circadian rhythms of superhelical status of dna in cyanobacteria. Proceedings of the National Academy of Sciences 104(47):18819–18824

[14] Andersson CR, Tsinoremas NF, Shelton J, Lebedeva NV, Yarrow J, Min H, and Golden SS (2000) Application of bioluminescence to the study of circadian rhythms in cyanobacteria. In Bioluminescence and Chemiluminescence Part C, volume 305 of *Methods in Enzymology*, pp. 527–542. Academic Press

[15] Min H, Liu Y, Johnson CH, and Golden SS (2004) Phase determination of circadian gene expression in synechococcus elongatus pcc 7942. Journal of Biological Rhythms 19(2):103–112. PMID: 15038850

[16] Kumar R, Grosbart M, Nurse P, Bahng S, Wyman CL, and Marians KJ (2017) The bacterial condensin mukb compacts dna by sequestering supercoils and stabilizing topologically isolated loops. Journal of Biological Chemistry 292(41):16904–16920

[17] Nolivos S and Sherratt D (2014) The bacterial chromosome: architecture and action of bacterial SMC and SMC-like complexes. FEMS Microbiology Reviews 38(3):380–392

[18] Mackey SR, Choi JS, Kitayama Y, Iwasaki H, Dong G, and Golden SS (2008) Proteins found in a cika interaction assay link the circadian clock, metabolism, and cell division in *Synechococcus elongatus*. Journal of Bacteriology 190(10):3738–3746

[19] Wang X, Llopis PM, and Rudner DZ (2013) Organization and segregation of bacterial chromosomes. Nature Reviews Genetics 14(3):191–203

[20] Lesterlin C, Gigant E, Boccard F, and Espéli O (2012) Sister chromatid interactions in bacteria revealed by a site-specific recombination assay. The EMBO Journal 31(16):3468–3479

[21] Paddock ML, Boyd JS, Adin DM, and Golden SS (2013) Active output state of the *Synechococcus* kai circadian oscillator. Proceedings of the National Academy of Sciences 110(40):E3849–E3857

[22] Yang S, Kim S, Kim DK, Jeon An H, Bae Son J, Hedén Gynnå A, and Ki Lee N (2019) Transcription and translation contribute to gene locus relocation to the nucleoid periphery in e. coli. Nature Communications 10(1):5131

[23] Vijayan V and O'Shea EK (2013) Sequence determinants of circadian gene expression phase in cyanobacteria. Journal of Bacteriology 195(4):665–671

[24] Taton A, Unglaub F, Wright NE, Zeng WY, Paz-Yepes J, Brahamsha B, Palenik B, Peterson TC, Haerizadeh F, Golden SS, and Golden JW (2014) Broad-host-range vector system for synthetic biology and biotechnology in cyanobacteria. Nucleic Acids Research 42(17):e136–e136

[25] Clerico EM, Ditty JL, and Golden SS (2007) Specialized Techniques for Site-Directed Mutagenesis in Cyanobacteria, pp. 155–171. Humana Press, Totowa, NJ

[26] Mutsuda M, Michel KP, Zhang X, Montgomery BL, and Golden SS (2003) Biochemical properties of cika, an unusual phytochrome-like histidine protein kinase that resets the circadian clock in *Synechococcus elongatus* pcc 7942. Journal of Biological Chemistry 278(21):19102–19110

[27] Schindelin J, Arganda-Carreras I, Frise E, Kaynig V, Longair M, Pietzsch T, Preibisch S, Rueden C, Saalfeld S, Schmid B, Tinevez JY, White DJ, Hartenstein V, Eliceiri K, Tomancak P, and Cardona A (2012) Fiji: an open-source platform for biological-image analysis. Nature Methods 9(7):676–682

[28] Dorfman R (1979) A formula for the gini coefficient. The Review of Economics and Statistics 61(1):146–149

[29] Mackey SR, Ditty JL, Clerico EM, and Golden SS (2007) Detection of Rhythmic Bioluminescence From Luciferase Reporters in Cyanobacteria, pp. 115–129. Humana Press, Totowa, NJ

[30] Zielinski T, Moore AM, Troup E, Halliday KJ, and Millar AJ (2014) Strengths and Limitations of Period Estimation Methods for Circadian Data. PLoS ONE 9(5):e96462

[31] Faulkner M, Rodriguez-Ramos J, Dykes GF, Owen SV, Casella S, Simpson DM, Beynon RJ, and Liu LN (2017) Direct characterization of the native structure and mechanics of cyanobacterial carboxysomes. Nanoscale 9:10662–10673

[32] Lam V and Villa E (2021) Practical Approaches for Cryo-FIB Milling and Applications for Cellular Cryo-Electron Tomography, pp. 49–82. Springer US, New York, NY

[33] Wagner FR, Watanabe R, Schampers R, Singh D, Persoon H, Schaffer M, Fruhstorfer P, Plitzko J, and Villa E (2020) Preparing samples from whole cells using focused-ion-beam milling for cryo-electron tomography. Nature Protocols 15(6):2041–2070

[34] Schorb M, Haberbosch I, Hagen WJH, Schwab Y, and Mastronarde DN (2019) Software tools for automated transmission electron microscopy. Nature Methods 16(6):471–477

[35] Mastronarde DN (2005) Automated electron microscope tomography using robust prediction of specimen movements. Journal of Structural Biology 152(1):36–51

[36] Hagen WJ, Wan W, and Briggs JA (2017) Implementation of a cryo-electron tomography tilt-scheme optimized for high resolution subtomogram averaging. Journal of Structural Biology 197(2):191–198. Electron Tomography

[37] Tegunov D and Cramer P (2019) Real-time cryo-electron microscopy data preprocessing with warp. Nature Methods 16(11):1146–1152

[38] Zheng SQ, Palovcak E, Armache JP, Verba KA, Cheng Y, and Agard DA (2017) Motioncor2: anisotropic correction of beam-induced motion for improved cryo-electron microscopy. Nature Methods 14(4):331–332

[39] Mastronarde DN and Held SR (2017) Automated tilt series alignment and tomographic reconstruction in imod. Journal of Structural Biology 197(2):102–113. Electron Tomography

[40] Mastronarde DN (1997) Dual-axis tomography: An approach with alignment methods that preserve resolution. Journal of Structural Biology 120(3):343–352

[41] Kremer JR, Mastronarde DN, and McIntosh J (1996) Computer visualization of three-dimensional image data using imod. Journal of Structural Biology 116(1):71–76

[42] Castaño-Díez D, Kudryashev M, Arheit M, and Stahlberg H (2012) Dynamo: A flexible, user-friendly development tool for subtomogram averaging of cryo-em data in high-performance computing environments. Journal of Structural Biology 178(2):139–151. Special Issue: Electron Tomography

[43] Scheres SH (2012) Relion: Implementation of a bayesian approach to cryo-em structure determination. Journal of Structural Biology 180(3):519–530

[44] Tegunov D, Xue L, Dienemann C, Cramer P, and Mahamid J (2021) Multi-particle cryo-em refinement with m visualizes ribosome-antibiotic complex at 3.5 å in cells. Nature Methods 18(2):186–193

[45] Martinez-Sanchez A, Garcia I, Asano S, Lucic V, and Fernandez JJ (2014) Robust membrane detection based on tensor voting for electron tomography. Journal of Structural Biology 186(1):49–61

[46] Weiss GL, Kieninger AK, Maldener I, Forchhammer K, and Pilhofer M (2019) Structure and function of a bacterial gap junction analog. Cell 178(2):374–384.e15

[47] Rast A, Schaffer M, Albert S, Wan W, Pfeffer S, Beck F, Plitzko JM, Nickelsen J, and Engel BD (2019) Biogenic regions of cyanobacterial thylakoids form contact sites with the plasma membrane. Nature Plants 5(4):436–446

[48] Nagar E, Zilberman S, Sendersky E, Simkovsky R, Shimoni E, Gershtein D, Herzberg M, Golden SS, and Schwarz R (2017) Type 4 pili are dispensable for biofilm development in the cyanobacterium synechococcus elongatus. Environmental Microbiology 19(7):2862–2872

[49] Yang Y, Lam V, Adomako M, Simkovsky R, Jakob A, Rockwell NC, Cohen SE, Taton A, Wang J, Lagarias JC, Wilde A, Nobles DR, Brand JJ, and Golden SS (2018) Phototaxis in a wild isolate of the cyanobacterium *Synechococcus elongatus*. Proceedings of the National Academy of Sciences 115(52):E12378–E12387

[50] Kaplan M, Oikonomou CM, Wood CR, Chreifi G, Ghosal D, Dobro MJ, Yao Q, Pal RR, Baidya AK, Liu Y, Maggi S, McDowall AW, Ben-Yehuda S, Rosenshine I, Briegel A, Beeby M, Chang YW, Shaffer CL, Jensen GJ, and Galperin MY (2022) Discovery of a novel inner membrane-associated bacterial structure related to the flagellar type iii secretion system. Journal of Bacteriology 0(0):e00144–22

[51] Wilde A and Mullineaux CW (2015) Motility in cyanobacteria: polysaccharide tracks and type iv pilus motors. Molecular Microbiology 98(6):998–1001

[52] Chang YW, Rettberg LA, Treuner-Lange A, Iwasa J, Søgaard-Andersen L, and Jensen GJ (2016) Architecture of the type iva pilus machine. Science 351(6278):aad2001

[53] Stingaciu LR, O'Neill H, Liberton M, Urban VS, Pakrasi HB, and Ohl M (2016) Revealing the dynamics of thylakoid membranes in living cyanobacterial cells. Scientific Reports 6:19627 EP –. Article

[54] Gan F, Shen G, and Bryant DA (2015) Occurrence of far-red light photoacclimation (farlip) in diverse cyanobacteria. Life 5(1):4–24

[55] Tamary E, Kiss V, Nevo R, Adam Z, Bernát G, Rexroth S, Rögner M, and Reich Z (2012) Structural and functional alterations of cyanobacterial phycobilisomes induced by high-light stress. Biochimica et Biophysica Acta (BBA) - Bioenergetics 1817(2):319–327

[56] Huokko T, Ni T, Dykes GF, Simpson DM, Brownridge P, Conradi FD, Beynon RJ, Nixon PJ, Mullineaux CW, Zhang P, and Liu LN (2021) Probing the biogenesis pathway and dynamics of thylakoid membranes. Nature Communications 12(1):3475

[57] Cohen SE, Erb ML, Selimkhanov J, Dong G, Hasty J, Pogliano J, and Golden SS (2014) Dynamic localization of the cyanobacterial circadian clock proteins. Curr Biol 24:1836–1844

[58] Tseng R, Goularte NF, Chavan A, Luu J, Cohen SE, Chang YG, Heisler J, Li S, Michael AK, Tripathi S, Golden SS, LiWang A, and Partch CL (2017) Structural basis of the day-night transition in a bacterial circadian clock. Science 355(6330):1174–1180

[59] Snijder J, Schuller JM, Wiegard A, Lössl P, Schmelling N, Axmann IM, Plitzko JM, Förster F, and Heck AJR (2017) Structures of the cyanobacterial circadian oscillator frozen in a fully assembled state. Science 355(6330):1181–1184

[60] Pattanayek R, Williams DR, Pattanayek S, Xu Y, Mori T, Johnson CH, Stewart PL, and Egli M (2006) Analysis of kaia–kaic protein interactions in the cyano-bacterial circadian clock using hybrid structural methods. The EMBO Journal 25(9):2017–2028

[61] Lucas BA, Himes BA, Xue L, Grant T, Mahamid J, and Grigorieff N (2021) Locating macromolecular assemblies in cells by 2d template matching with cistem. eLife 10:e68946

[62] Rickgauer JP, Grigorieff N, and Denk W (2017) Single-protein detection in crowded molecular environments in cryo-em images. eLife 6:e25648

[63] Gilbert BR, Thornburg ZR, Lam V, Rashid FZM, Glass JI, Villa E, Dame RT, and Luthey-Schulten Z (2021) Generating chromosome geometries in a minimal cell from cryo-electron tomograms and chromosome conformation capture maps. Frontiers in Molecular Biosciences 8

[64] Xiang Y, Surovtsev IV, Chang Y, Govers SK, Parry BR, Liu J, and Jacobs-Wagner C (2021) Interconnecting solvent quality, transcription, and chromosome folding in escherichia coli. Cell 184(14):3626–3642.e14

[65] Hood RD, Higgins SA, Flamholz A, Nichols RJ, and Savage DF (2016) The stringent response regulates adaptation to darkness in the cyanobacterium synechococcus elongatus. Proceedings of the National Academy of Sciences 113(33):E4867–E4876

[66] Tagami K, Nanamiya H, Kazo Y, Maehashi M, Suzuki S, Namba E, Hoshiya M, Hanai R, Tozawa Y, Morimoto T, Ogasawara N, Kageyama Y, Ara K, Ozaki K, Yoshida M, Kuroiwa H, Kuroiwa T, Ohashi Y, and Kawamura F (2012) Expression of a small (p)ppgpp synthetase, ywac, in the (p)ppgpp0 mutant of bacillus subtilis triggers yvyd-dependent dimerization of ribosome. MicrobiologyOpen 1(2):115–134

[67] Mori M, Zhang Z, Banaei-Esfahani A, Lalanne JB, Okano H, Collins BC, Schmidt A, Schubert OT, Lee DS, Li GW, Aebersold R, Hwa T, and Ludwig C (2021) From coarse to fine: the absolute escherichia coli proteome under diverse growth conditions. Molecular Systems Biology 17(5):e9536

[68] Chubukov V, Gerosa L, Kochanowski K, and Sauer U (2014) Coordination of microbial metabolism. Nature Reviews Microbiology 12(5):327–340

[69] Kato T, Yoshida H, Miyata T, Maki Y, Wada A, and Namba K (2010) Structure of the 100s ribosome in the hibernation stage revealed by electron cryomicroscopy. Structure 18(6):719–724

[70] Beckert B, Abdelshahid M, Schäfer H, Steinchen W, Arenz S, Berninghausen O, Beckmann R, Bange G, Turgay K, and Wilson DN (2017) Structure of the bacillus subtilis hibernating 100s ribosome reveals the basis for 70s dimerization. The EMBO Journal 36(14):2061–2072

[71] Cameron JC, Wilson SC, Bernstein SL, and Kerfeld CA (2013) Biogenesis of a bacterial organelle: The carboxysome assembly pathway. Cell 155(5):1131–1140

[72] Kerfeld CA and Melnicki MR (2016) Assembly, function and evolution of cyanobacterial carboxysomes. Current Opinion in Plant Biology 31:66 – 75

[73] Bekker A, Holland HD, Wang PL, Rumble D, Stein HJ, Hannah JL, Coetzee LL, and Beukes NJ (2004) Dating the rise of atmospheric oxygen. Nature 427(6970):117–120

[74] Price GD, Badger MR, Woodger FJ, and Long BM (2007) Advances in understanding the cyanobacterial CO2-concentrating-mechanism (CCM): functional components, Ci transporters, diversity, genetic regulation and prospects for engineering into plants. Journal of Experimental Botany 59(7):1441–1461

[75] Wan W and Briggs J (2016) Chapter thirteen - cryo-electron tomography and subtomogram averaging. In The Resolution Revolution: Recent Advances In cryoEM, (ed.) Crowther R, volume 579 of *Methods in Enzymology*, pp. 329–367. Academic Press

[76] Breuer M, Earnest TM, Merryman C, Wise KS, Sun L, Lynott MR, Hutchison CA, Smith HO, Lapek JD, Gonzalez DJ, de Crécy-Lagard V, Haas D, Hanson AD, Labhsetwar P, Glass JI, and Luthey-Schulten Z (2019) Essential metabolism for a minimal cell. eLife 8:e36842

[77] Mahamid J, Pfeffer S, Schaffer M, Villa E, Danev R, Kuhn Cuellar L, Förster F, Hyman AA, Plitzko JM, and Baumeister W (2016) Visualizing the molecular sociology at the hela cell nuclear periphery. Science 351(6276):969–972

[78] Koning RI, Koster AJ, and Sharp TH (2018) Advances in cryo-electron tomography for biology and medicine. Annals of Anatomy - Anatomischer Anzeiger 217:82–96

[79] Russo CJ and Passmore LA (2016) Progress towards an optimal specimen support for electron cryomicroscopy. Current Opinion in Structural Biology 37:81–89

[80] Al-Amoudi A, Chang JJ, Leforestier A, McDowall AW, Michel Salamin L, Norlén L, Richter K, Sartori Blanc N, Studer D, and Dubochet J (2004) Cryo-electron microscopy of vitreous sections. The EMBO Journal 23:3583–3588

[81] Al-Amoudi A, Studer D, and Dubochet J (2005) Cutting artefacts and cutting process in vitreous sections for cryo-electron microscopy. Journal of Structural Biology 150(1):109–121

[82] Mahamid J, Tegunov D, Maiser A, Arnold J, Leonhardt H, Plitzko JM, and Baumeister W (2019) Liquid-crystalline phase transitions in lipid droplets are related to cellular states and specific organelle association. Proceedings of the National Academy of Sciences 116(34):16866–16871

[83] Chaikeeratisak V, Khanna K, Nguyen KT, Sugie J, Egan ME, Erb ML, Vavilina A, Nonejuie P, Nieweglowska E, Pogliano K, Agard DA, Villa E, and Pogliano J (2019) Viral capsid trafficking along treadmilling tubulin filaments in bacteria. Cell 177(7):1771–1780.e12

[84] Khanna K, Lopez-Garrido J, Zhao Z, Watanabe R, Yuan Y, Sugie J, Pogliano K, and Villa E (2019) The molecular architecture of engulfment during *Bacillus subtilis* sporulation. eLife 8:e45257

[85] Lopez-Garrido J, Ojkic N, Khanna K, Wagner FR, Villa E, Endres RG, and Pogliano K (2018) Chromosome translocation inflates bacillus forespores and impacts cellular morphology. Cell 172(4):758–770.e14

[86] Noble JM, Lubieniecki J, Savitzky BH, Plitzko J, Engelhardt H, Baumeister W, and Kourkoutis LF (2018) Connectivity of centermost chromatophores in rhodobacter sphaeroides bacteria. Molecular Microbiology 109(6):812–825

[87] Mosalaganti S, Kosinski J, Albert S, Schaffer M, Strenkert D, Salomé PA, Merchant SS, Plitzko JM, Baumeister W, Engel BD, and Beck M (2018) In situ architecture of the algal nuclear pore complex. Nature Communications 9(1):2361

[88] Schaffer M, Mahamid J, Engel BD, Laugks T, Baumeister W, and Plitzko JM (2017) Optimized cryo-focused ion beam sample preparation aimed at in situ structural studies of membrane proteins. Journal of Structural Biology 197(2):73–82

[89] Chaikeeratisak V, Nguyen K, Khanna K, Brilot AF, Erb ML, Coker JKC, Vavilina A, Newton GL, Buschauer R, Pogliano K, Villa E, Agard DA, and Pogliano J (2017) Assembly of a nucleus-like structure during viral replication in bacteria. Science 355(6321):194–197

[90] Rosenzweig ESF, Xu B, Cuellar LK, Martinez-Sanchez A, Schaffer M, Strauss M, Cartwright HN, Ronceray P, Plitzko JM, Förster F, Wingreen NS, Engel BD, Mackinder LC, and Jonikas MC (2017) The eukaryotic co2-concentrating organelle is liquid-like and exhibits dynamic reorganization. Cell 171(1):148–162.e19

[91] Bäuerlein FJ, Saha I, Mishra A, Kalemanov M, Martínez-Sánchez A, Klein R, Dudanova I, Hipp MS, Hartl FU, Baumeister W, and Fernández-Busnadiego R (2017) In situ architecture and cellular interactions of polyq inclusions. Cell 171(1):179–187.e10

[92] Zhang J, Ji G, Huang X, Xu W, and Sun F (2016) An improved cryo-fib method for fabrication of frozen hydrated lamella. Journal of Structural Biology 194(2):218–223

[93] Engel BD, Schaffer M, Kuhn Cuellar L, Villa E, Plitzko JM, and Baumeister W (2015) Native architecture of the *Chlamydomonas* chloroplast revealed by in situ cryo-electron tomography. eLife 4:e04889

[94] Harapin J, Börmel M, Sapra KT, Brunner D, Kaech A, and Medalia O (2015) Structural analysis of multicellular organisms with cryo-electron tomography. Nature Methods 12:634–636

[95] Villa E, Schaffer M, Plitzko JM, and Baumeister W (2013) Opening windows into the cell: focused-ion-beam milling for cryo-electron tomography. Current Opinion in Structural Biology 23(5):771–777. Protein-carbohydrate interactions / Biophysical methods

[96] Wang K, Strunk K, Zhao G, Gray JL, and Zhang P (2012) 3d structure determination of native mammalian cells using cryo-fib and cryo-electron tomography. Journal of Structural Biology 180(2):318–326

[97] Rigort A, Bäuerlein FJB, Villa E, Eibauer M, Laugks T, Baumeister W, and Plitzko JM (2012) Focused ion beam micromachining of eukaryotic cells for cryoelectron tomography. Proceedings of the National Academy of Sciences 109(12):4449–4454

[98] Marko M, Hsieh C, Schalek R, Frank J, and Mannella C (2007) Focused-ion-beam thinning of frozen-hydrated biological specimens for cryo-electron microscopy. Nature Methods 4:215

[99] Rajput NS and Luo X (2015) Chapter 3 - FIB Micro-/Nano-fabrication. In Micromanufacturing Engineering and Technology, (ed.) Qin Y, Micro and Nano Technologies, pp. 61–80. William Andrew Publishing, Boston, second edition

[100] Volkert CA and Minor AM (2007) Focused ion beam microscopy and micromachining. MRS Bulletin 32(5):389–399

[101] Chyr I and Steckl AJ (2001) Gan focused ion beam micromachining with gas-assisted etching. Journal of Vacuum Science & Technology B: Microelectronics and Nanometer Structures Processing, Measurement, and Phenomena 19(6):2547–2550

[102] Schaffer M, Pfeffer S, Mahamid J, Kleindiek S, Laugks T, Albert S, Engel BD, Rummel A, Smith AJ, Baumeister W, and Plitzko JM (2019) A cryo-fib lift-out technique enables molecular-resolution cryo-et within native caenorhabditis elegans tissue. Nature Methods 16(8):757–762

[103] Zhang J, Zhang D, Sun L, Ji G, Huang X, Niu T, and Sun F (2019) VHUT-cryo-FIB, a method to fabricate frozen-hydrated lamella of tissue specimen for in situ cryo-electron tomography. bioRxiv

[104] Mahamid J, Schampers R, Persoon H, Hyman AA, Baumeister W, and Plitzko JM (2015) A focused ion beam milling and lift-out approach for site-specific preparation of frozen-hydrated lamellas from multicellular organisms. Journal of Structural Biology 192(2):262–269

[105] Stevie FA, Griffis DP, and Russell PE (2005) Focused Ion Beam Gases for Deposition and Enhanced Etch, pp. 53–72. Springer US, Boston, MA

[106] Diebolder C, Faas F, Koster A, and Koning R (2015) Conical fourier shell correlation applied to electron tomograms. Journal of Structural Biology 190(2):215–223

[107] Strunk K, Wang K, Ke D, Gray J, and Zhang P (2012) Thinning of large mammalian cells for cryo-TEM characterization by cryo-FIB milling. Journal of Microscopy 247(3):220–227

[108] Medeiros JM, Böck D, Weiss GL, Kooger R, Wepf RA, and Pilhofer M (2018) Robust workflow and instrumentation for cryo-focused ion beam milling of samples for electron cryotomography. Ultramicroscopy 190:1–11

[109] Guo YS, Furrer JM, Kadilak AL, Hinestroza HF, Gage DJ, Cho YK, and Shor LM (2018) Bacterial extracellular polymeric substances amplify water content variability at the pore scale. Frontiers in Environmental Science 6:93

[110] Arnold J, Mahamid J, Lucic V, de Marco A, Fernandez JJ, Laugks T, Mayer T, Hyman AA, Baumeister W, and Plitzko JM (2016) Site-specific cryo-focused ion beam sample preparation guided by 3D correlative microscopy. Biophysical Journal 110(4):860–869

[111] Nahmani M, Lanahan C, DeRosier D, and Turrigiano GG (2017) High-numerical-aperture cryogenic light microscopy for increased precision of superresolution reconstructions. Proceedings of the National Academy of Sciences 114(15):3832–3836

[112] Carlson DB and Evans JE (2011) Low-cost cryo-light microscopy stage fabrication for correlated light/electron microscopy. JoVE (52):e2909

[113] Tuijtel MW, Koster AJ, Jakobs S, Faas FGA, and Sharp TH (2019) Correlative cryo super-resolution light and electron microscopy on mammalian cells using fluorescent proteins. Scientific Reports 9(1):1369

[114] Schellenberger P, Kaufmann R, Siebert CA, Hagen C, Wodrich H, and Grünewald K (2014) High-precision correlative fluorescence and electron cryo microscopy using two independent alignment markers. Ultramicroscopy 143:41–51. SI: Correlative Microscopy

[115] Chang YW, Chen S, Tocheva EI, Treuner-Lange A, Löbach S, Søgaard-Andersen L, and Jensen GJ (2014) Correlated cryogenic photoactivated localization microscopy and cryo-electron tomography. Nature Methods 11(7):737–739

[116] Kaufmann R, Schellenberger P, Seiradake E, Dobbie IM, Jones EY, Davis I, Hagen C, and Grünewald K (2014) Super-resolution microscopy using standard fluorescent proteins in intact cells under cryo-conditions. Nano Letters 14(7):4171–4175

[117] Wolff G, Limpens RWAL, Zheng S, Snijder EJ, Agard DA, Koster AJ, and Bárcena M (2019) Mind the gap: micro-expansion joints drastically decrease the bending of FIB-milled cryo-lamellae. bioRxiv

[118] Marko M, Hsieh C, Moberlychan W, Mannella CA, and Frank J (2006) Focused ion beam milling of vitreous water: prospects for an alternative to cryo-ultramicrotomy of frozen-hydrated biological samples. Journal of Microscopy 222(1):42–47

[119] Toro-Nahuelpan M, Zagoriy I, Senger F, Blanchoin L, Théry M, and Mahamid J (2019) Tailoring cryo-electron microscopy grids by photo-micropatterning for in-cell structural studies. bioRxiv

[120] Stokes DJ, Vystavel T, and Morrissey F (2007) Focused ion beam (FIB) milling of electrically insulating specimens using simultaneous primary electron and ion beam irradiation. Journal of Physics D: Applied Physics 40(3):874–877